DOCTOR OF PHILOSOPHY

Fabrication and characterisation of silver-glass nanocomposites

Wackerow, Stefan

Award date:
2014

DOCTOR OF PHILOSOPHY

Fabrication and Characterisation of Silver-Glass Nanocomposites

Stefan Wackerow

2014

University of Dundee

Fabrication and Characterisation of Silver-Glass Nanocomposites

Stefan Wackerow, Dipl-Phys.

Supervisor: Prof Amin Abdolvand

A thesis submitted to the School of Engineering, Physics and Mathematics, University of Dundee for the degree of Doctor of Philosophy (PhD)

May 2014

Table of Contents

List of figures

List of tables

List of abbreviations

AD	Anno Domini, in the year of the Lord
CCD	Charge-coupled device
DNA	Deoxyribonucleic acid
EBS	Electron Backscattering mode in Scanning Electron Microscopy
EDX	Energy-dispersive X-ray spectroscopy
eq.	Equation
GSC	Glass-silver composite, which is the material analysed in chapter 4
MGT	Maxwell-Garnett theory
NBO	Non-bridging oxygen
NIR	Near infrared
ns	Nanosecond, referring to laser pulse length
ppm	Parts per million
ps	Picosecond, referring to laser pulse length
SEM	Scanning Electron Microscopy, Scanning Electron Microscope
SERS	Surface Enhanced Raman Scattering
SPR	Surface Plasmon Resonance
UV	Ultraviolet
VIS	Visible light
wt-%	Percentage by weight

Declaration

I certify that I, the undersigned, am the author of this thesis, that I have consulted all the cited references, that the work in this thesis was done by me, and that this work has not previously been accepted for a higher degree.

Stefan Wackerow

Certification

I, Professor A. Abdolvand of the School of Engineering, Physics and Mathematics, hereby certify that Stefan Wackerow has spent the required number of terms at research under my supervision and that he has fulfilled the conditions of the Ordinance of the University of Dundee so that he is qualified to submit the following thesis for the degree of Doctor of Philosophy.

Amin Abdolvand

List of publications

The following publications of the author are related to this thesis:

1. Wackerow, S. and A. Abdolvand, *Generation of silver nanoparticles with controlled size and spatial distribution by pulsed laser irradiation of silver ion-doped glass.* Optics Express, 2014. **22**(5): p. 5076-5085.

2. Wackerow, S. and A. Abdolvand, *Optical analyses of the formation of a silver nanoparticle-containing layer in glass.* Optics Express, 2012. **20**(21): p. 23227-23234.

3. Wackerow, S. and A. Abdolvand, *Laser-assisted one-step fabrication of homogeneous glass–silver composite.* Appl. Phys. A, 2012. **109**(1): p. 45-49.

4. Wackerow, S., G. Seifert, and A. Abdolvand, Homogeneous *silver-doped nanocomposite glass.* Opt. Mater. Express, 2011. **1**(7): p. 1224-1231.

Related conference presentations of the author:

5. Wackerow, S., Abdolvand, A., *Creating metallic films by laser irradiation of silver ion exchanged glasses*, CLEO Munich 2013

6. Wackerow, S., Abdolvand, A., *DC electric field assisted fabrication and optical analysis of silver-doped nanocomposite glass*, CLEO Munich 2013

7. Wackerow, S., Abdolvand, A., Homogeneous *silver-glass nanocomposites*, Photon 12, Durham 2012

Other publications of the author:

8. Fleming, A. H., S. Wackerow, A. C. Hourd, W. A. Gillespie, G. Seifert and A. Abdolvand, *Diffractive optical element embedded in silver-doped nanocomposite glass.* Optics Express, 2012. **20**(20): p. 22579-22584.

9. Wackerow, S. and G. Seifert, *Co-Doping of glasses with rare earth ions and metallic nanoparticles for frequency up-conversion.* Proc.SPIE, 2010. **7725**.

10. Hallermann, F., Rockstuhl, C., Fahr, S., Seifert, G., Wackerow, S., Graener, H., Plessen, G. v., Lederer, F., *On the use of localized plasmon polaritons in solar cells.* physica status solidi (a), 2008. **205**(12): p. 2844-2861.

11. Graener, H., Abdolvand, A., Wackerow, S., Kiriyenko, O., Hergert, W., *Optical properties of photonic/plasmonic structures in nanocomposite glass.* physica status solidi (a), 2007. **204**(11): p. 3838-3847.

Other conference presentations:

12. Wackerow, S., Seifert, G. *Co-doping of glasses with rare earth ions and metallic nanoparticles for frequency up-conversion*, SPIE Photonics Europe, Brussels 2010

13. Wackerow, S., Dyrba, M., Schweizer, S., Seifert, G., Graener, H., *Improving up-conversion efficiency of rare earth ions by metallic nanoparticles*, DPG Spring Meeting, Dresden 2009

14. Kiriyenko, O., W. Hergert, S. Wackerow, M. Beleites, and H. Graener. *Photonic/Plasmonic Structures from Metallic Nanoparticles in a Glass Matrix*. in *Proceedings of the COMSOL Conference in Hannover.* 2008.

15. Kiriyenko, O., W. Hergert, S. Wackerow, and H. Graener, *Effective Permittivity and Optical Properties of Photonic/Plasmonic Structures in Nanocomposite Glass.* COMSOL Users Conference Grenoble 2007

16. Wackerow, S., Abdolvand, A., Seifert, G., Graener, H., *Mikrostrukturierung silbernanopartikelhaltiger Gläser durch elektrische Felder*, DPG spring meeting, Regensburg 2007

Acknowledgements

I am most grateful to my supervisor, Professor Amin Abdolvand, for giving me the opportunity to carry out this research, for his enthusiasm and constant support. I also want to thank Professor Allan Gillespie for his continuous support and encouragement, and the Engineering and Physical Sciences Research Council (EPSRC) for funding.

Further I want to thank Dr Andrew Hourd for fruitful discussions on topics of Chemistry, Dr Yongchang Fan for his help with electron microscopy, Dr Stephen Reynolds for discussions on Comsol simulations, Dr David Goldie for his conductivity measurements on ion-exchanged glasses and the Optics group in Halle for giving access to their microscope spectrometer.

I want to thank the technicians, in particular Gary Callon, Callum Moore and Stuart Anthony for fruitful discussions on technical questions and for technical support. I also want to thank Grant Kydd for helping with carbon coating.

Also I want to thank my colleagues, especially Guang Tang for fruitful discussions on laser irradiation and thermal modelling, Fu Yu and Dalong Zang for computer-related help, and Svetlana Zolotkovskaya, Lauren Fleming Mateusz Tyrk and Stephen Grant for nice collaborations.

Abstract

Metallic nanoparticles and nanostructures have spawned significant interest in a wide area of science. Nanoparticles in glass show unique linear and nonlinear optical properties due to surface plasmon resonances. These induce absorption and scattering of light around the resonance wavelength, which can be tuned by changing size, shape or spatial distribution of the nanoparticles. Metallic nanostructures show local field enhancement effects, which are used for example in surface enhanced Raman scattering. Their large surface area compared to bulk materials makes them interesting for applications in chemistry and life science.

In this thesis the synthesis of two different types of silver-glass nanocomposites is investigated. Both materials are prepared from silver ion-exchanged glass, which is also prepared and characterised in house.

The first type of nanocomposite is glass doped with silver nanoparticles. It is formed by annealing silver ion-exchanged glass at a temperature close to the transition point. This induces the reduction of silver to atoms and the agglomeration in nanoparticles with a diameter of less than 10nm, which are located in a layer beneath the glass surface, which has a thickness of tens of micrometres. These nanoparticles are responsible for a characteristic absorption band centred around 410nm due to plasmon resonances.

The second nanocomposite, which was first produced in the course of this work, is called glass-silver composite. It is created by pulsed laser irradiation of silver ion-exchanged glass. It contains nanoparticles with a diameter of 100nm or more, which are distributed homogeneously in a dense single monolayer at the glass surface. This material shows a strong metal-like reflection of light. The location of nanoparticles at

the surface makes it interesting for applications utilising the field enhancement effect of the nanoparticles, such as surface enhanced Raman scattering and enhancement of light conversion.

Both nanocomposites and the ion-exchanged glass are characterised by optical microscopy, scanning electron microscopy and optical spectroscopy.

The work is divided in four chapters, starting with an introduction in chapter 1. In chapter 2 the method of production of the silver ion-exchanged glass and the properties of the material are presented. Generation of nanoparticles inside the glass by annealing is covered in chapter 3 and an analysis of laser processing of ion-exchanged glasses is shown in chapter 4. The concluding chapter consists of a summary of the work and an outlook.

1. Introduction to metal-glass nanocomposites

A nanocomposite is a material consisting of two or more different phases where one of the phases has at least one dimension of less than 100 nanometres. In this work two different nanocomposites are presented, including their synthesis and analysis of properties. Both are consisting of a glass with silver nanoparticles. The first contains nanoparticles inside the glass in a layer at the surface with a thickness of 10 to 200 µm. It is synthesised by annealing of silver ion exchanged glass. The second has a dense monolayer of silver nanoparticles directly at the surface. This is manufactured by irradiating the same silver ion exchanged glass with pulsed lasers.

In this chapter the fundamentals of these materials are presented, starting with an overview of properties and applications of metal nanoparticles in section 1.1, followed by an introduction to the type of material presented here in 1.2.

1.1. Properties of metal nanoparticles and their applications

Generally nanoparticles are entities of a material with a size from a few atoms up to about 100nm. Particles and structures of this size show several very interesting properties not seen in bulk objects of similar materials. These gave rise to very large interest not only in the field of physics [1, 2], but also in life science and chemistry [3], resulting in thousands of related publications per year nowadays.

1.1.1. Surface plasmon resonances

An important difference between nanoparticles and bulk objects of the same material lies in their optical properties. For metal nanoparticles these are mostly determined by

surface plasmon resonances – collective charge oscillations at the interface between metals and dielectrics. In bulk metals these are excitations of oscillations of free electrons at the surface, which are spreading in longitudinal modes at the interface. They are evanescent waves, meaning that they can not spread into free space and are confined to the interface. Because of this they can also only be excited by evanescent waves. Coupling light to these plasmons is normally done with a prism coupler[4], which generates evanescent waves by total internal reflection in the prism, and allows matching the transversal component of speed of light to the phase velocity of plasmons.

Plasmon oscillations at surfaces are strongly dampened, which limits their propagation length, for example the (1/e) decay length at 633nm on gold is 9µm, while it is 60µm on silver. Surface plasmons in nanoparticles have different properties, since they are localised to a single nanoparticle. Periodic oscillations of electrons at the particle surface occur, called surface plasmon resonances (SPR). Unlike plasmons in bulk metals these oscillations are easily excited by light, resulting in a distinct optical absorption. This process is illustrated in fig. 1.1. This absorption effect has been utilised since ancient times to give glass a red colour by adding gold or a yellow colour by adding silver. A very famous example for this is the Lycurgus Cup [5] shown in fig 1.2, which originates from the Byzantine Empire and is now exhibited in the British

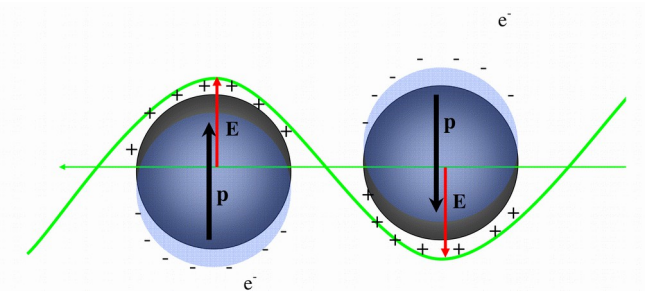

Fig. 1.1: Illustration of surface plasmon oscillations in nanoparticles induced by an electromagnetic wave.

(a) *(b)*

Fig. 1.2: Lycurgus Cup. In (a) light is shining through the cup from the back. The glass looks red because gold and silver particles inside the glass are absorbing blue and green light. In (b) the Lycurgus Cup is illuminated from the front. Without light coming through it shows a green colour.

Museum in London, Room 50. Another typical example are colourful ornaments in church windows.

While this utilisation of plasmon resonances of nanoparticles by artists occurred quite early, some of the first scientific studies on such materials were published in the early twentieth century [2]. A very important step was the now widely used theory of light scattering by spherical particles, developed by Gustav Mie in 1908 [6]. It describes the absorption of metal nanoparticles as an electromagnetic phenomenon. It has taken until 1970, when Uwe Kreibig and Peter Zacharias first described these absorptions in terms of surface plasmons [7].

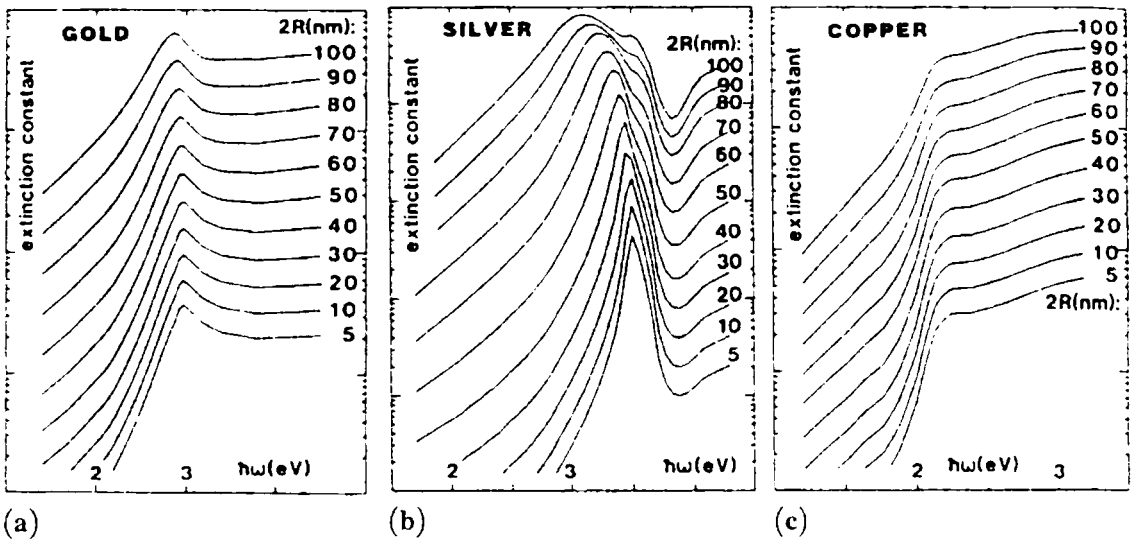

Fig. 1.3: Dependence of surface plasmon resonance on particle material and size, calculated by Mie theory for particles in vacuum. From [1]

The resonance frequency of surface plasmon oscillations depends on the size, shape and material of metal nanoparticles[8]. Examples of the absorption of gold silver and copper nanoparticles of different sizes in vacuum are shown in fig. 1.3. These graphs not only show the absorption due to the plasmon resonance, but also absorption due to interband transitions of bound electrons. For silver the plasmon band is centred at about 3eV (410nm), while interband transitions occur from around 4eV upwards (320nm and less).

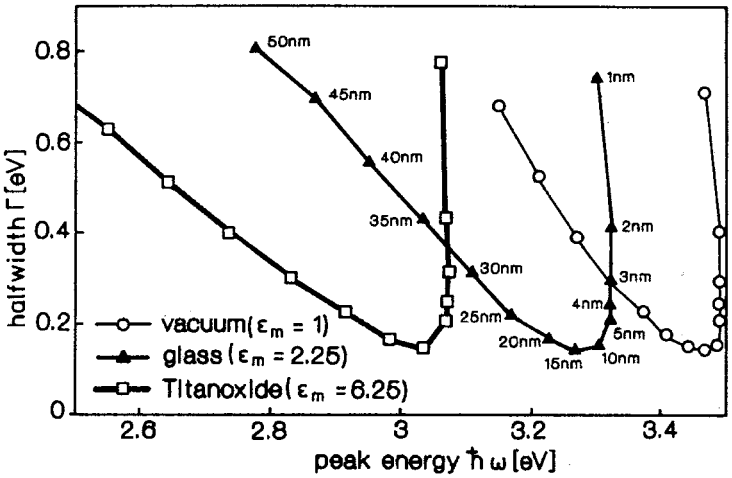

Fig. 1.4: SPR peak position and half width of silver nanoparticles in different host materials and for different particle sizes. From [1]

For gold and copper plasmon resonance absorption and interband transitions are overlapping.

The resonance frequency also depends on the host material. Examples for silver nanoparticles in different materials are shown in fig. 1.4.

The theoretical simulation of surface plasmon resonances is covered in section 1.6.

1.1.2. Enhancement of electromagnetic fields

In 1974 a very important effect was observed for the first time (but not yet understood), the so called surface enhanced Raman scattering (SERS) [9]. Raman scattering is the inelastic scattering of photons on atoms or molecules, which is greatly increased in SERS by electromagnetic fields in the vicinity of finely structured surfaces [9, 10], substrates with nanoparticles [11] or nanoparticles in solution [12].

In Raman spectroscopy a material is irradiated with monochromatic light, and the spectrum of strayed light is analysed. It shows photons with different wavelength than the incoming light, which results from photons transferring a part of their energy to atoms or molecules of the material. Due to the structure of allowed energy levels the spectrum of scattered light shows higher intensities for specific wavelengths, which can be used to identify the material. However Raman scattering is not an efficient process, normally requiring either high laser intensities or large amounts of scattering material.

Nearby metallic nanostructures electromagnetic fields can be enhanced by several orders of magnitude, which is exploited in SERS to generate much stronger signals. There are different processes discussed in literature, for example field enhancement near metallic nanoparticles for excitations close to their plasmon resonance frequency, and

strong emissions from tips on rough surfaces due to plasmons. These effects can increase the efficiency of SERS strong enough to analyse single molecules [12, 13].

This field enhancement near metallic nanostructures recently received a large interest from the field of solar cells. It can be useful to increase the absorption efficiency of solar cells directly [14], by placing nanostructures on solar cells, so that the enhanced fields can generate more charge carriers in the cell. A lot of work was also done on increasing the efficiency of frequency conversion by placing the converting ions or molecules close to metallic nanostructures [14]. It is suspected that the presence of nanoparticles can enhance both absorption and emission of the converting ions or molecules. Frequency conversion can increase solar efficiency by up-conversion [15-17], where two photons with an energy below the band gap of the solar cell are absorbed and a single photon with higher energy is emitted. Efficiency can also be increased by down conversion [18], where photons from the high frequency range are converted. Solar cells are not efficient at using high energy photons since each photon generates a charge carrier with the band gap energy. If a photon has a larger energy the difference is lost in the form of heat. In down conversion high energy photons are absorbed, and one or more photons with lower energy are emitted.

1.1.3. Modification of metallic nanoparticles

Silver nanoparticles in glass are normally spherical, showing a plasmon resonance wavelength between 400 and 450nm, depending on particle sizes. If they are deformed to elliptical nanoparticles they show two or three different resonance frequencies instead, depending on the orientation of the polarisation vector of light relative to the particle. The different absorption for different polarisations is called dichroism.

Two ways have been found to deform them to elliptical particles. This can be done by heating and then stretching the softened glass [19]. The embedded nanoparticles are stretched together with the surrounding matrix. The other way is by irradiation with ultrashort laser pulses [20-22].

The absorption bands produced by particle deformation can be quite wide, especially if particles with different sizes and aspect ratios are involved. This is utilised by the company Codixx, which is mostly selling polarisers that they make by stretching of silver nanoparticle-containing glass.

The elliptical deformation by ultrashort laser pulses can be used to make micropolarisers [23], which can for example be used to make individual pixels of a CCD detector sensitive to specific polarisation. The fine structuring can also be used for durable storing of data [24]. Using different polarisation orientations and plasmon resonance wavelengths roughly five bits per spot can be recorded.

Ultrashort laser pulses can also be used to dissolve nanoparticles locally [25], which allows to generate microstructures consisting of transparent areas and areas with nanoparticles. Such dissolution can also be done by strong electric fields at elevated temperatures [26]. With a structured electrode this can be exploited to produce microstructures on a large scale [27, 28].

1.1.4. Other properties and applications

Another large field of application of metallic nanostructures is plasmonic sensing [29, 30]. Often utilised is the strong effect of refractive index changes close to a nanoparticle on the particle's plasmon resonance frequency. This allows detection of gases and

vapours [31]. For sensing biomolecules functionalised gold nanoparticles are used. These particles are attached to molecules, for example DNA strains or antibodies. A very high sensitivity can be achieved for DNA that binds to two complementary DNA strains, with both complementary strains attached to different nanoparticles or a nanoparticle and a metal surface. The presence of the other nanoparticle or metal surface has a strong effect on the plasmon resonance wavelength, which can be measured with a spectrometer. The same structure is used for sensing antigens, with antibodies bound to nanoparticles.

When nanoparticles are placed very close together energy can be transferred between surface plasmon oscillations of the particles. Placing several nanoparticles in a line, with the right distance between particles, results in guiding of light along this so-called plasmonic chain waveguide [32, 33].

Nanoparticles often show a larger chemical activity due to the greatly increased surface compared to bulk material. This is especially interesting for catalytic processes [3, 34, 35]. Due to the strong absorption of surface plasmon resonances nanoparticles are also interesting for photochemistry [36].

The much larger surface area compared to bulk materials strongly decreases the effect of weight force compared to surface forces. This leads to stability of nanoparticles in liquids due to surface charges and Brownian motion.

If nanoparticles are small enough, then they show quantum mechanical properties. This is utilised in quantum dots, which are nanocrystals made of semiconductor materials. In these excitons, which are bound states of excited electrons and holes, are located to a single quantum dot. If they form optical emitters their emission frequency depends on

the size of the quantum dot. Also they can work like a single electron transistor. This is a device where conductance between two electrodes can be blocked by a single charge localised on a quantum dot.

If metallic nanoparticles are arranged in a three-dimensional lattice structure, then they can form a photonic crystal with a photonic band gap [37]. A photonic bandgap is also shown by two-dimensional arrays of nanorods.

Nanoparticles in glasses show a strong nonlinear absorption [38, 39]. Due to the short lifetime of SPRs of about 10fs [40] these materials are very interesting for applications in optical switching [41].

1.2. Characteristics of silicate glasses

As mentioned earlier glasses with silver and gold nanoparticles have been manufactured since ancient times. This was done by adding small amounts of metallic gold or silver to a glass melt. However this allows to achieve only very small concentrations of metal nanoparticles, since silver and gold can be added in only very small concentrations to the glass melt. In higher concentrations these noble metals will aggregate already in the glass melt, falling out in the form of macroscopic droplets.

Higher concentrations of noble metals can be achieved by ion exchange processes. To understand these processes it is important to know some things about the structure of the used glasses.

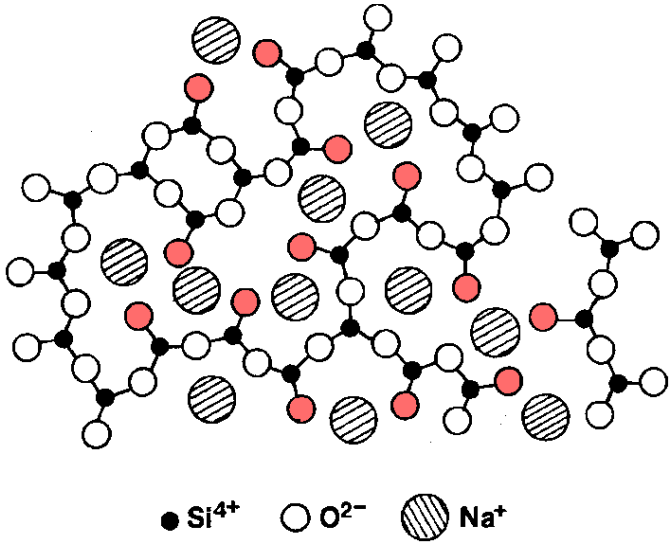

Fig. 1.5: Principle structure of a typical glass. Black are the silicon atoms, which are surrounded by four oxygen atoms and forming the three-dimensional glass network. Embedded in this are positively charged ions. Single-bound non-bridging oxygen ion nearby. are compensating the charge, which are marked in red.

1.2.1. The structure of glass

Glasses in general are a type of amorphous solids. Amorphous materials are lacking the long-range order of crystals, showing a regular structure only for particles that are nearby. Characteristic property of glasses is that they show a glass transition, which is a reversible transition from a solid, hard state to a molten or rubber-like state. This takes place not at a fixed temperature, but over a temperature range.

What we normally understand under glass are materials consisting of amorphous silicon oxide and some additives. Silicon oxide is called the network former since it forms the structure of the glass, which is called the glass matrix. Often different kinds of alkali metals and alkaline earth metals are added, called the network modifiers. They are added to change properties of the glass, most important reducing the softening point to simplify production. In the glass these exist in the form of more loosely bound

monovalent and divalent ions. Their charge is locally compensated by non-bridging oxygen ions in the glass matrix. Fig. 1.5 shows the principle structure of such a glass.

Another component often added is aluminium. This is incorporated into the glass matrix. It is trivalent and replaces silicon atoms, which have a valence of 4. This disturbs the formation of regular crystals of silicon oxide, resulting in an amorphous network.

In glasses several types of defects can occur. These can be caused by many types of impurities, but also the glass matrix itself can have different types of defects. Defects of the glass matrix are well analysed in fused silica [42], which is a glass consisting of pure silicon oxide.

The best known defect in fused silica is the E' centre. It is illustrated by a Si atom which is bound to only three Oxygen and therefore has an unpaired electron (≡Si·). Other defects believed to occur in fused silica are the peroxy linkage (≡Si-O-O-Si≡), the neutral oxygen vacancy (≡Si-Si≡), and the two-coordinated silicon (-O-$\overline{\text{Si}}$-O-).

There are three types of oxygen hole centres in fused silica: the nonbridging-oxygen hole centre (NBOHC, ≡Si-O·), the peroxy radical ≡Si-O-O· and the self-trapped hole centre (STH), which comprises a delocalized electron hole. STH bleach above 130K and disappear at temperatures above 200K. NBOHCs are identical to the non-bridging oxygen mentioned before.

1.2.2. B270 glass

The glass used in this work is B270, a soda lime glass that is often used in optical applications. It is a low-iron crown glass manufactured by Schott AG in an up-draw

process. Float glass sheets are manufactured by floating molten glass on a molten metal, typically tin (Sn). While Sn is immiscible in molten glass and does not diffuse into the whole volume, there is always a surface layer on one side of the glass of about 100nm [43] or less [44] containing Sn in the form of Sn^{2+} or Sn^{4+}[43]. Sn ions are a potential reducing agent [45]. Since it is only on one side of the glass, both sides of a float glass behave differently when used for the formation of silver nanoparticles [46]. Since B270 is manufactured in an up-draw process it does not have the high Sn concentration on one glass side, and therefore both glass sides behave quite similarly.

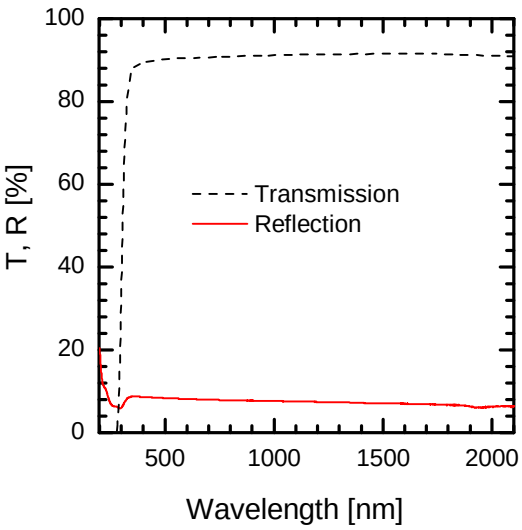

Fig. 1.6: Transmission and Reflection of B270 glass, measured with the Jasco spectrometer.

The composition of B270 is, in wt-%: 69.2 SiO_2, 9.8 Na_2O, 9.5 CaO, 7.6 K_2O, 2.8 BaO, 1.1 Al_2O_3. It is transparent from 300 to 2700 nm as shown in fig. 1.6. Its density is 2.55g/cm³. From these values and the known molar masses the composition in at-% can be calculated: 60.0% O, 25.0% Si, 6.9% Na, 3.7% Ca, 3.5% K, 0.5% Al, 0.4% Ba.

The refractive index at 589nm is 1.5229. Its transition temperature is 533°C, and the mean thermal expansion between 20°C and 300°C is $9.4 \cdot 10^{-6}$ K^{-1}. The heat conductivity [W/(m x K)] is: 0.92 (24.5°C), 1.01 (89°C), 1.08 (127°C), 1.15 (167°C) (from PGO-online.com).

1.3. Silver

Silver is a rare element with an abundance of 0.079ppm in Earth's crust. It is a metal with face-centred cubic crystal structure. In chemical compounds it is normally in the monovalent state.

It has the highest electrical conductivity of all metals and a high heat conductivity. As long as its surface is not oxidised it shows the strongest reflection of visible light of all metals.

It is used for optical mirrors because of its superb reflection in visible range and near infrared. Reflectivity drops considerably in the UV range, starting with a slight decrease from 500nm downwards, and showing a strong drop around 350nm. There exist special UV-enhanced silver mirrors which have an additional dielectric coating to increase UV reflection. Alternatively aluminium mirrors can be used if UV ranges are involved, or purely dielectric mirrors.

In ancient Rome mirrors made of massive silver existed. It is said that metal-coated glass mirrors were already in first century AD. This technique was improved over time. In medieval times metal alloys were inserted into hollow glass spheres while still molten, while later on glass was coated with a mercury-tin amalgam. Finally in 1835 Justus von Liebig published how to make mirrors by precipitation of metallic silver on glass from heated silver nitrate mixed with aldehyde. This was used to start mass production of mirrors. Nowadays household mirrors are often coated with the cheaper aluminium.

There are several other applications of silver, beside the ever-present use. For a long

time of human history silver was used as an investment and for jewellery. There are applications in electrics and electronics utilising its high conductivity. It is used in heat conductive paste and electrically conductive glues. Silver halides are disintegrating under light, which is used in photography. During the 20th century a large fraction of the world-wide silver production was used for this, but this rapidly declined with the increasing usage of digital photography.

Silver is used as a catalyst. It catalyses partially oxidizing reactions, for example for converting ethylene to ethylene oxide [34] or formaldehyde from methanol [47]. At the surface of silver exist different kinds of oxygen centres, some providing oxygen, others which can cause catalytic dehydrogenation. It can also catalyse the hydrogenation of unsaturated organic compounds.

It is also used in medical applications. It shows antibacterial properties and therefore is used in wound dressings, coatings of devices. It is also used in some clothing to reduce smell.

In glass silver can exist as Ag^+ in ionic form, taking the places of a single negatively charged non-bridging oxygen nearby. In low concentrations it can exist in atomic form, dissolved in the glass matrix. In higher concentrations atomic silver is aggregating to silver nanoparticles.

Silver ions show a characteristic Gaussian absorption band centred at 240nm [46, 48]. This is caused by 4f-5s electron transitions. Silver atoms show an absorption band centred at 350nm [49] which is caused by $5sS_{1/2}$-$5pP_{3/2}$ transitions.

The absorption band of silver ions overlaps with the absorption of most glasses. So the

peak of the absorption normally can not be measured, but its flank can be measured as a change of the absorption edge of the material. If both silver ions and atoms are present in the glass these flanks of the absorption of atoms and ions can normally not be separated.

1.4. Materials presented in this work

Production of two different types of metal-glass nanocomposites is shown in this work. Both are produced from silver ion-exchanged glass. Annealing this glass at temperatures of around 550°C, which is close to the glass transition threshold of the glass, will result in the generation of a high number of small silver nanoparticles inside the glass. The other type of nanocomposite forms when the ion-exchanged glass is irradiated with pulsed high-power lasers. With the right laser parameters this results in the formation of a single layer of densely packed silver nanoparticles at the surface of the glass. This is a newly discovered phenomenon.

The silver ion-exchanged glass which is used as a base material here is produced by a field assisted ion exchange process from a solid silver film, which is used as the positive electrode (anode). When an electric field is applied to a glass at elevated temperatures the positive ions (anions) are moving away from the anode towards the negative cathode, where they are neutralised. Under the anode they are leaving negatively charged vacancies. If the anode is supplying other positive ions then they will fill the vacancies, replacing the removed ions. In our case the metallic silver film provides Ag+ ions, which are replacing the Na^+ ions in the glass.

There are other methods for bringing silver into a glass matrix. Since ancient times

silver was added directly to the glass melt. But this allows only to produce very small concentrations of silver in the glass, much lower than the concentrations achieved by ion exchange at lower temperatures. If silver salts are added to a glass melt when the glass is manufactured it can only be dissolved in amounts of 0.003-0.1 wt-% [50].

Another common approach is by thermal diffusion from a salt melt [51]. By adding different salts to the melt the composition of the glass at the surface can be controlled in this process. Though this process involves more hazardous materials such as $AgNO_3$, it works only in a limited temperature range and is slower than field-assisted ion exchange.

1.5. Characterisation techniques

1.5.1. Optical characterization

Optical characterisation methods are a great tool for characterising silver-glass nanocomposites. This exploits the absorption caused by the surface plasmon oscillations of silver nanoparticles, which occurs in the blue spectral range.

The transmission and reflection spectra of large modified sample areas are analysed with a JASCO V-670 UV/VIS/NIR spectrophotometer. The obtained spectra allow to determine the total amount of nanoparticles in the glass from the strength of absorption by the surface plasmon oscillations. Also the shape and position of the plasmon band allows conclusions to be drawn about nanoparticle sizes.

An overview of the general structure of nanocomposites is obtained with a KEYENCE Digital Microscope VHX-1000. It can produce images in transmission mode and in

reflection mode. This allows to characterise the homogeneity and structure of metal-glass nanocomposites. Silver nanoparticle containing areas appear in yellow, orange or brown due to the absorption by SPRs. Optical microscopy also shows any surface structures.

Of some samples thin slices were prepared, which allows to visualize depth profiles with the microscope. For this, the sample was embedded in an epoxy resin (Specifix-20, Struers Limited) to prevent chipping of the glass and to make it physically manageable for grinding, polishing etc. The resin cures at room temperature. The section has been polished on both sides and was just over 30µm thick.

We also had the opportunity to analyse these thin slices with a microscope spectrophotometer of the type Zeiss MPM 800D/UV, which was provided by the Optics Group at the University Halle/Saale in Germany. It allows to measure transmission spectra in small areas of a microscope image, which is defined by an adjustable rectangular diaphragm.

1.5.2. Electron microscopy

Scanning electron microscopy (SEM) is a very useful tool to analyse ion exchanged glasses, especially in electron backscattering mode (EBS). The standard operating mode of SEM devices is the secondary electron mode, which analyses low energy electrons generated by the electron beam at the surface. Due to their low energy of typically less than 50eV these electrons travel only a view nanometres through the specimen, making this imaging method very sensitive to the surface topography.

In electron backscattering mode high energy back-reflected electrons are analysed. The

intensity of back reflection depends on the atomic mass and the density of the scattering materials, making this imaging mode sensitive to sample compositions. Due to the higher electron energy electrons from a depth of up to 500nm are contributing to the image. Due to the high atomic mass of silver compared to the glass constituents this mode clearly shows the ion-exchanged region and silver nanoparticles as bright areas.

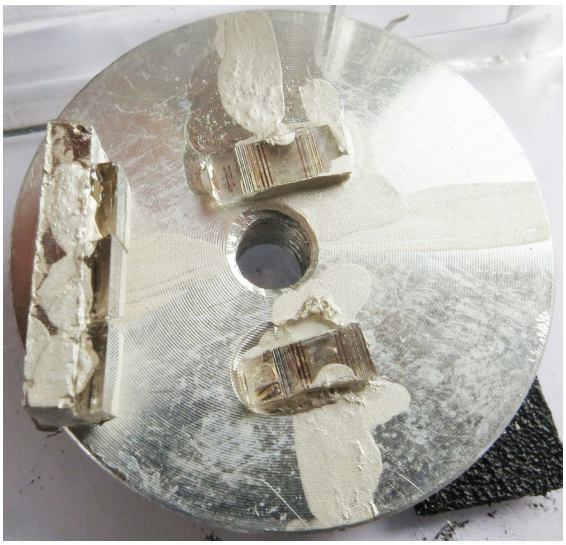

Fig. 1.7: SEM sample holder with glass samples for imaging the top surface (centre top and bottom) and the cross section in the left. Silver paste and carbon coating prevent charge build-ups. The diameter of the sample holder is 25mm

On non-conducting surfaces the electron bombardment in the SEM chamber leads to a charge build-up in the specimen. This is disturbing the imaging, and can make it impossible to depict any features of the imaged object. Because the analysed glass is non-conducting all specimen had to be coated with a carbon layer. The thickness of this was usually 15nm, which is sufficiently thin to not disturb the imaging. To ensure contact on vertical glass pieces silver paste was applied. An example photograph of a sample holder with glass pieces placed vertically and horizontally is shown in fig 1.7.

It was taken care not to contaminate the analysed nanostructures with silver paste, since it consists of the same material as the analysed nanostructures. Any contamination with these silver flakes of a size of 10µm would have been easily spotted in taken images though due to their structure.

The SEM device offers the function to analyse the composition of specimen by energy-dispersive X-ray spectroscopy (EDX). High energy electrons of the electron beam can excite electrons from inner shells of atoms of the analysed specimen. The resulting vacancies are quickly filled with electrons from higher shells, resulting in the emission of X-ray photons with energies which are characteristic for each element. By measuring the energy of the generated X-ray photons an X-ray spectrum is obtained. This allows to determine the elemental composition of the analysed volume.

1.6. Simulating optical properties of metal nanoparticles in glass

The optical properties of glasses with metallic nanoparticles are dominated by the effects of the nanoparticles' surface plasmon resonances [1].

Important characteristics are nanoparticle sizes, expressed either as the diameter d or radius r for spherical nanoparticles. Also important is the filling factor f, expressed as the ratio of total nanoparticle volume to the glass volume.

Most relevant for the optical properties in visible light is the absorption due to the plasmon oscillations. For large nanoparticles (d>50nm) scattering also has to be taken into account. For large filling factors, larger than about 2%, the interaction between nanoparticles has to be taken into account.

Several different approaches are known to simulate these optical properties, all having different advantages and disadvantages. A common simulation approach is to calculate absorption and scattering cross sections of single nanoparticles. Most common are the Mie theory [6] and the dipole approximation [52]. Both allow to simulate the scattering

which has to be included for larger nanoparticles. The Mie theory also includes higher order oscillations that are not included in the dipole approximation. These are relevant for particles larger than 50nm.

The extinction a of a layer of thickness l of a material containing nanoparticles can be calculated from the Beer Lambert law:

$$a = -\ln \frac{I}{I_0} = \sigma_{ext} c_N l = \sigma_{ext} \frac{f}{V_0} l \tag{1.1}$$

where σ_{ext} is the absorption cross section, c_N the number density of nanoparticles, f the filling factor, V_0 the particle volume. I_0 is the intensity of incident light, I the transmitted intensity. The quotient I/I_0 is the transmission, the natural logarithm the extinction. Extinction is a measure for the total attenuation of transmitted light, normally due to absorption, scattering, diffraction and reflection. The Mie theory takes absorption and scattering into account. Diffraction is not relevant here, the effect of reflection can be deducted from measurements by doing reference measurements with a clear glass.

Another common approach are effective medium theories which can compute an effective dielectric function for a composite medium. Most known are the Maxwell Garnett theory (MGT) [23] and the Bruggemann theory [53]. To some extend particle interaction is included, although there are deviations for high filling factors. Scattering is not included in these theories, making them less suitable for larger nanoparticles.

These models are giving an effective dielectric function $\boldsymbol{\varepsilon_{eff}}$ of the composite material. This function is frequency-dependent. This frequency dependence results from the fact that the change of polarisation of materials is not instantaneous. This non-instantaneous response induces a phase change in the resulting displacement D_0, which is expressed

by a complex dielectric function $\boldsymbol{\varepsilon}$:

$$D_0 e^{-i\omega t} = \boldsymbol{\varepsilon}(\omega) E_0 e^{-i\omega t} \tag{1.2}$$

where ω is the circular frequency.

Other optical properties can be calculated from this by the following formulas, starting with the complex refractive index:

$$\boldsymbol{n} = n + i\kappa = \sqrt{\boldsymbol{\varepsilon}_{\boldsymbol{eff}}} \tag{1.3}$$

where n is the refractive index of the medium indicating the phase speed, and κ is the absorption.

The absorption coefficient α of the material is given by:

$$\alpha = \frac{2\omega}{c} \operatorname{Im} \sqrt{\boldsymbol{\varepsilon}_{\boldsymbol{eff}}(\omega)} \tag{1.4}$$

here c is the speed of light. If scattering is negligible the absorption coefficient is identical with the extinction coefficient.

The absorption a of a layer with thickness l is related to the absorption coefficient by:

$$a = \alpha l \tag{1.5}$$

which is a different form of the Beer-Lambert law (eq. 1.1) resulting from

$$\alpha = \sigma_{ext} c_N \tag{1.6}$$

The reflectivity R of a material for normal incidence of light can be calculated from the real part of the refractive index:

$$R(\omega) = \left| \frac{n(\omega) - 1}{n(\omega) + 1} \right| \tag{1.7}$$

In more recent works nanoparticle absorption has been modelled by computer

simulations. Very interesting is the work of Hinsen and Felderhof [54]. They are simulating ensembles of large concentrations of metal spheres and find a strong effect of multipole oscillations which are not included in the more simple effective medium theories.

For modelling the dielectric function of silver is needed, which is covered in the next section. Also needed are the dielectric properties of the host matrix. For B270 glass it is sufficient to use the constant value ε_h=2.4 in the visible range. The individual models are covered in the following sections.

1.6.1. Dielectric function of silver

From the frequency-dependent dielectric function of metal nanoparticles the maximum position of the dipole plasmon resonance can be found easily. It is given by:

$$\mathrm{Re}(\boldsymbol{\varepsilon_i}) = -2\varepsilon_h \tag{1.8}$$

where ε_i is the dielectric function of the metal inclusions, and ε_h that of the host material. ε_i is strongly dependent on the wavelength, while ε_h is approximately constant.

The dielectric function of silver can be approximated with the Drude model [55, 56]:

$$\boldsymbol{\varepsilon_i} = \varepsilon_{i,1} + i\,\varepsilon_{i,2} = \varepsilon_b - \frac{\omega_p^2}{\omega^2 + i\,\gamma\omega} \tag{1.9}$$

ε_b is the bound electron dielectric function, combining the effects of core electrons. γ is the dampening constant of electron oscillations. The electron plasma frequency ω_p can be calculated using:

$$\omega_p = \sqrt{\frac{N e^2}{\varepsilon_0 m_e}} \tag{1.10}$$

where e and m_e are the electron charge and mass, and N is the density of conducting electrons.

For bulk silver the plasma frequency ω_p is 9.2 eV. When simulating nanoparticles it is usually assumed that the particle boundary is abrupt. For small nanoparticles the quantummechanic wave functions of the electrons become relevant, which result in a change of electron density which is not abrupt, but over about the electron Fermi wavelength [1]. This effect is called the spill-out effect [1, 57]. It decreases the density of conducting electrons *N, which* reduces ω_p for small nanoparticles and causes a redshift of the plasmon band [57]. Also it slightly increases the effective radius of nanoparticles [1].

For a bulk metal the dampening constant γ is the ratio of the Fermi velocity v_F and the mean free path of the electrons L. If the size of metal nanoparticles is comparable to or smaller than the electron mean free path, scattering at the particle surface increases dampening. There have been different approaches to compute the dampening effect, with all of them resulting in the term $A\, v_F / r$, with different factors A [1]. Therefore, the dampening constant is [58]:

$$\gamma = \frac{v_F}{L} + A\frac{v_F}{r} \tag{1.11}$$

The size-dependent dampening results in a broadening of the plasmon band for smaller particles.

Values used in this work are $\varepsilon_b = 5.2$ [59], $v_f = 1.38 \cdot 10^6$ m/s [60, 61], $L = 57$ nm [61], and $A = 2$ [58].

The Drude model can also be used for simulating the plasmon band of gold or copper

nanoparticles [1, 62]. For these the interband transitions have to be taken into account in the form of a frequency-dependent complex ε_b. For silver the interband transitions are causing absorption for 320nm and less. These do not need to be taken into account for nanoparticles in glass because they are masked by the glass absorption.

Johnson and Christy determined the dielectric functions of Ag, Au and Cu experimentally [63]. They calculated the optical properties n and k from reflection and transmission measurements on vacuum-evaporated thin films. The values for silver were derived from the average of measurements done on films with thicknesses of 30.4nm and 37.5nm. From these the complex dielectric function was calculated and plotted in comparison with results of the Drude model in fig. 1.8.

Real parts of the dielectric functions are in good agreement, and change only minimally with particle sizes. The imaginary part changes strongly with the particle size used for modelling, and the experimental results are quite different for short wavelengths. The

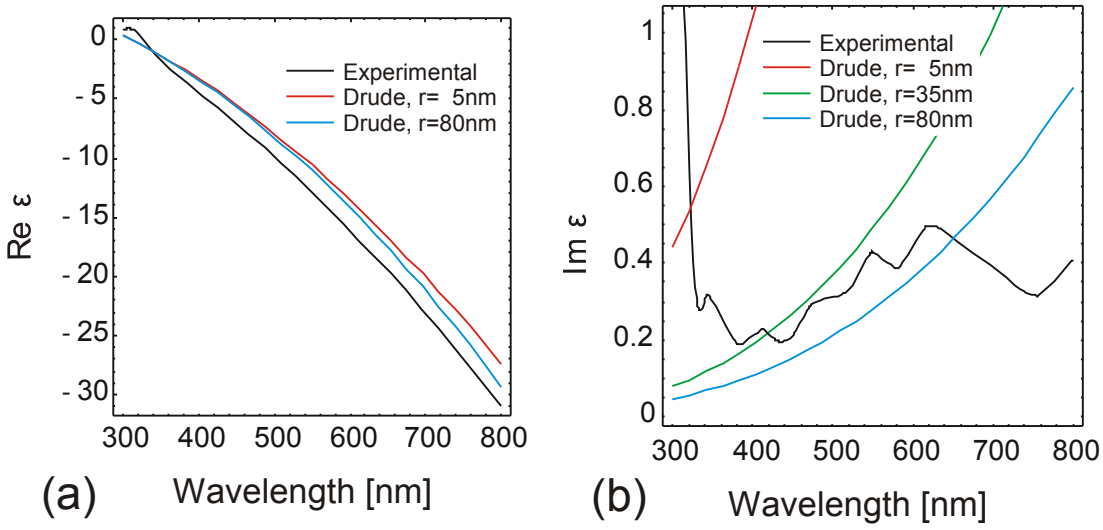

Fig. 1.8: Real (a) and imaginary (b) part of the dielectric function of silver. Comparison of experimental values found by Johnson and Christy for silver films of 30.4nm and 37.5nm [63] *with theoretical values from the Drude model with dampening for different particle radii.*

strong increase of the experimental result around 320nm can be attributed to interband transitions, which have not been included in the model. Otherwise the imaginary part is also quite similar for the measurements on a film and for particles with a size comparable to the film thickness. The similar scales are limiting the electron mean free path to similar values. Therefore the dampening constant is comparable for the film to that used in the Drude model, and the dielectric function becomes similar.

1.6.2. Mie theory and dipole approximation

The Mie theory [6] allows the calculation of scattering cross sections σ_{sca} and extinction cross sections σ_{ext} of spherical particles in a homogeneous matrix. For this Mie solved the Maxwell equations for a single particle and an electromagnetic wave coming from infinity. The obtained solutions describe the shift of plasmon band positions to longer wavelengths for large particle sizes. Formulas are given here following the descriptions in [1] and [64].

The extinction and scattering cross sections can be written as the following multipole expansion:

$$\sigma_{ext}(\lambda)=\frac{\lambda^2}{2\pi\varepsilon_h}\sum_{L=1}^{\infty}(2L+1)\,\mathrm{Re}(a_L+b_L) \tag{1.12}$$

$$\sigma_{sca}(\lambda)=\frac{\lambda^2}{2\pi\varepsilon_h}\sum_{L=1}^{\infty}(2L+1)(|a_L|^2+|b_L|^2) \tag{1.13}$$

λ is the wavelength in air, L is the number of the multipole oscillation, starting with the dipole oscillation for L=1 and the quadrupole oscillation for L=2.

The absorption cross section is the difference of the two:

$$\sigma_{abs}(\lambda)=\sigma_{ext}(\lambda)-\sigma_{sca}(\lambda) \tag{1.14}$$

The expansion coefficients are:

$$a_L = \frac{m\psi_L(m\alpha)\psi_L'(\alpha) - \psi_L'(m\alpha)\psi_L(\alpha)}{m\psi_L(m\alpha)\eta_L'(\alpha) - \psi_L'(m\alpha)\eta_L(\alpha)} \tag{1.15}$$

$$b_L = \frac{\psi_L(m\alpha)\psi_L'(\alpha) - m\psi_L'(m\alpha)\psi_L(\alpha)}{\psi_L(m\alpha)\eta_L'(\alpha) - m\psi_L'(m\alpha)\eta_L(\alpha)} \tag{1.16}$$

with the size parameter α:

$$\alpha = 2\pi r \frac{\sqrt{\varepsilon_h}}{\lambda} \tag{1.17}$$

ε_h is the real dielectric constant of the host matrix. r is the particle radius. m is given by:

$$m = \frac{\sqrt{\varepsilon_i}}{\sqrt{e_h}} \tag{1.18}$$

ε_i is the complex dielectric function of the inclusions (nanoparticles), ψ and η are the Ricatti-Bessel functions, which are defined in terms of the half-integer-order Bessel functions of the first kind ($J_{n+1/2}$) and of the second kind $Y_{n+1/2}$ in the form:

$$\psi_L(z) = \sqrt{\frac{\pi z}{2}} J_{n+1/2}(z) \tag{1.19}$$

$$\eta_L(z) = \sqrt{\frac{\pi z}{2}} \left(J_{n+1/2}(z) - i\, Y_{n+1/2}(z) \right) \tag{1.20}$$

Examples for simulations using the Mie theory were shown in fig. 1.3.

For small nanoparticles up to a diameter of about 50nm only the dipole oscillations have to be taken into account, higher orders have only small contributions. Then the extinction cross section can be simplified to:

$$\sigma_{ext,1}(\lambda) = \frac{24\pi^2 r^3}{\lambda} \frac{\varepsilon_h^{3/2}\varepsilon_{i,2}}{(\varepsilon_{i,1} + 2\varepsilon_h)^2 + \varepsilon_{i,2}^2} \tag{1.21}$$

$\varepsilon_i = \varepsilon_{i,1} + i\,\varepsilon_{i,2}$ is the dielectric function of the nanoparticle material.

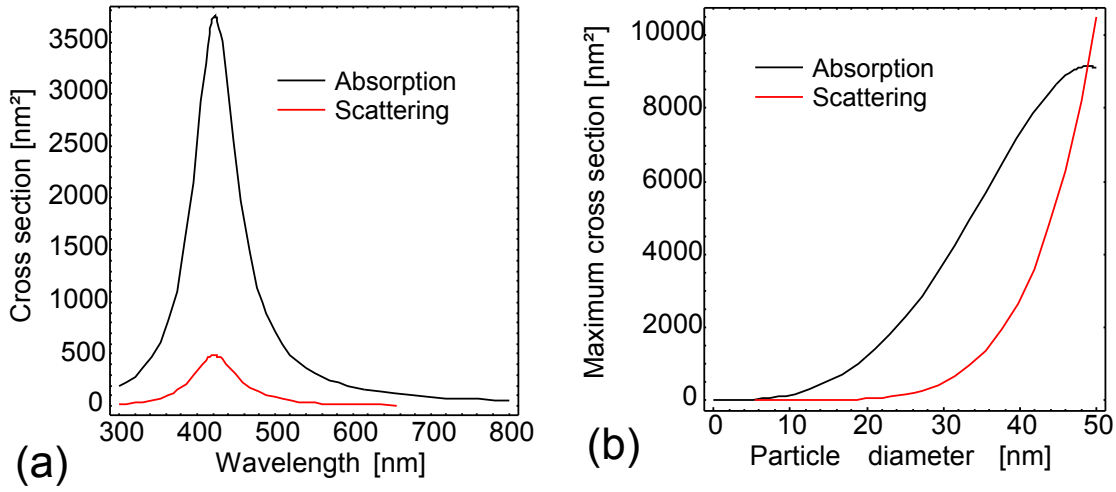

Fig. 1.9: Nanoparticle absorption and scattering calculated with the dipole approximation and the Drude model. ***(a)****: Absorption and scattering cross sections for a particle with a diameter of 30nm.* ***(b)****: Dependence of the peak height of absorption and scattering cross sections on the particle size*

Similar results to eq. 1.21 can be obtained by the dipole approximation [65]. This can be derived by considering a metal sphere as a dipole, and calculating its polarisability α(ω):

$$\alpha(\omega) = 4\pi r^3 \frac{\varepsilon_i(\omega) - e_h}{\varepsilon_i(\omega) + 2\varepsilon_h} \tag{1.22}$$

From this the extinction and scattering cross sections can be calculated:

$$\sigma_{ext} = k\,\mathrm{Im}(\alpha) \tag{1.23}$$

$$\sigma_{sca} = \frac{k^4}{6\pi}|\alpha|^2 \tag{1.24}$$

where $k = 2\pi\sqrt{\varepsilon_h}/\lambda$ is the wave number in the host medium.

With this the wavelength-dependent absorption was calculated. As the dielectric function of the nanoparticles the Drude model was used. The simulation result is shown in fig. 1.9.

1.6.3. Maxwell-Garnett theory

A theory that works better for larger filling factors is the Maxwell Garnett effective medium theory (MGT) [1, 66]. It is a theory describing clustered media which is based on the Clausius Mosotti equation and the dipole approximation. It does not consider multipole oscillations of the nanoparticle plasmons or multipole interactions between particles. Also it assumes spherical, separated particles. For low filling factors it agrees with the dipole approximation. For higher filling factors it describes correctly the shift of the plasmon band peak position [67]. The obtained plasmon band width is smaller than what is obtained with more accurate theories, such as the theory by Hinsen and Felderhof presented in section 1.6.4, but the deviations are acceptable as long as the filling factor is not too large.

For a medium with one type of inclusions with a filling factor f the formula for the effective dielectric constant of the composite medium is:

$$\varepsilon_{eff}(\omega) = \varepsilon_h \frac{(\varepsilon_i + 2\varepsilon_h) + 2f(\varepsilon_i - \varepsilon_h)}{(\varepsilon_i + 2\varepsilon_h) - f(\varepsilon_i - \varepsilon_h)} \tag{1.25}$$

From this the absorption, refractive index and reflection of a medium can be calculated with eq. 1.3 to 1.7.

The dielectric function of the nanoparticles ε_i can be calculated with the Drude model. With the particle size dependent dampening this allows to simulate spectra for different particle sizes and filling factors, which are very useful for analysing glasses with silver nanoparticles by comparison. Fig. 1.10 Shows an example of such simulations.

1.6.4. Spectral density theory, theory of Hinsen and Felderhof

The results of the MGT are not satisfying for large filling factors (>~10%). The form of plasmon bands differs from experimental results and other theories. [68].

The Bergman spectral density theory [69] is a strong tool for analysing effective medium theories [68].It allows to separate the effect of the geometric arrangement of the components of a mixture from the effect of the values of the dielectric functions of the components.

Based on this Hinsen and Felderhof [54] developed a very accurate simulation based on statistical averaging of ensembles of nanoparticles with random arrangement. For specific filling factor values they have found the deviations from the Clausius-Mossotti relation, which the Maxwell Garnett theory is based on. Therefore it delivers much more accurate values. For the simulated ensembles the total averaged induced dipole moment $\overline{M}_S$ is written in the form

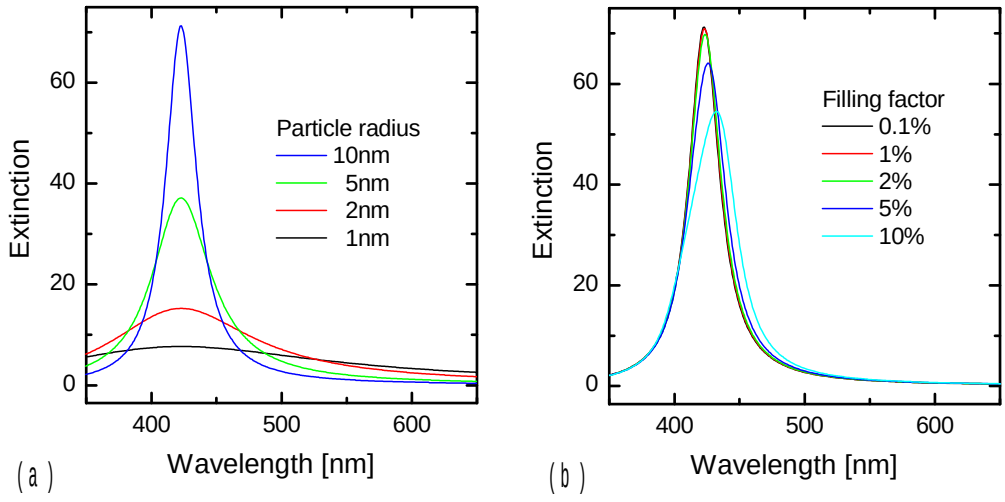

Fig. 1.10: (a) Particle size dependence for f = 0.1 % and a layer thickness of 100 µm. (b) Filling factor dependence for particle radius of 10 nm, and a layer thickness proportional to 1/f, in order to bring the plasmon bands to comparable heights.

$$\overline{M_S} = \frac{1}{3}\varepsilon_h G_S r^3 E_0 \tag{1.26}$$

where r is the particle radius and E_0 a uniform external applied field, ε_h: the dielectric function of surrounding medium. G_S is the response scalar:

$$G_S = 3\frac{\varepsilon_{eff} - \varepsilon_h}{\varepsilon_{eff} + 2\varepsilon_h} \tag{1.27}$$

This can be solved for the effective dielectric function of the effective medium ε_{eff}:

$$\varepsilon_{eff} = \varepsilon_h \frac{3 + 2G_S}{3 - G_S} \tag{1.28}$$

The response scalar is derived from computer simulations and has the continued-fraction representation:

$$G_S(z) = \cfrac{3f}{z - \cfrac{a_1}{z + b_2 - \cfrac{a_2}{z + b_3 - \ddots}}} \tag{1.29}$$

With the volume filling factor f. a_i, b_i: coefficients calculated by computer simulations; values listed in [54], and z is:

$$z = \frac{\varepsilon_i + 2\varepsilon_h}{\varepsilon_i - \varepsilon_h} \tag{1.30}$$

where ε_i: is the dielectric function of inclusions. The coefficients a_j, b_j quickly tend to limiting values a_∞, b_∞. Because of this, the fractions of G_S in formula 1.29 also tend to a limiting value. For high i, the term

$$f_i(z) = \frac{a_i}{z + b_i - \ldots} \tag{1.31}$$

can be replaced with:

$$f_i(z) = \frac{1}{2}(z + b_\infty) - \frac{1}{2}\sqrt{(z + b_\infty)^2 - 4a_\infty} \tag{1.32}$$

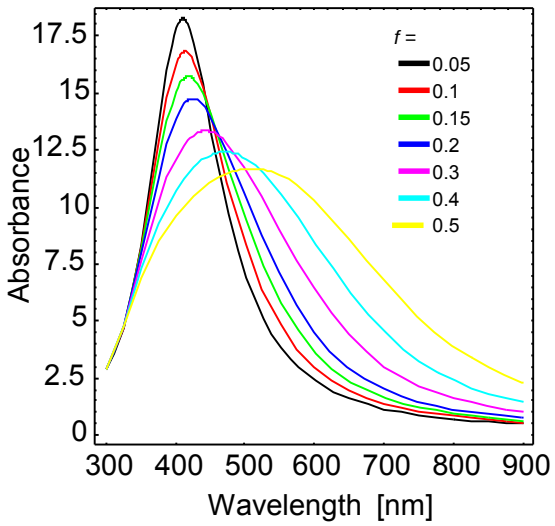

Fig. 1.11: Felderhof simulation results for plasmon bands of silver nanoparticles with different filling factors. Layer thickness is 100nm/f

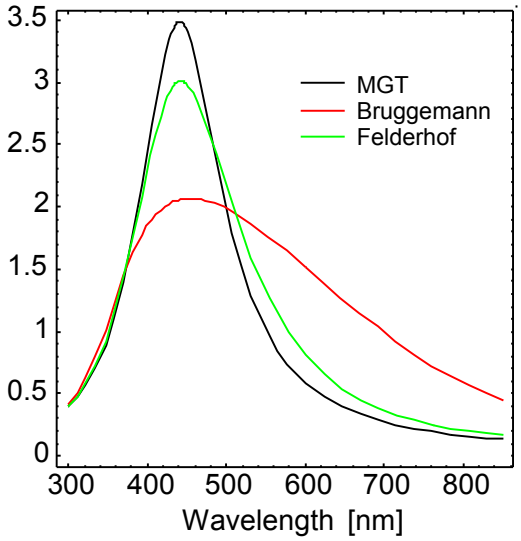

Fig. 1.12: Comparison of different effective medium models for silver nanoparticles in glass, f=0.3, thickness 200nm. The Felderhof theory is the most accurate one.

Fig. 1.11 shows simulations for a glass with silver nanoparticles for all particle sizes simulated in [54]. For ε_i the Drude model with dampening for particles with a diameter of 4nm was used.

Fig. 1.12 shows a simulation done with this theory in comparison to the Maxwell Garnett theory and the Bruggemann theory [1, 53]. The Felderhof theory is the most accurate of these effective medium theories, and this graph shows the deviation of the other theories. Both other theories produce plasmon bands with the same peak position, but their forms are differing.

2. Fabrication and characterisation of silver ion doped glass

A first step for producing the two silver-glass nanocomposites presented in this work is to manufacture silver ion doped glass. The two nanocomposites are glass with silver nanoparticles and the glass-silver composite (GSC) manufactured by laser irradiation.

The glass with silver nanoparticles is a material which is analysed extensively in research and also used in industry. For example Codixx AG is offering polarisers based on this material. The polarisation effect results from the elliptical shape of nanoparticles in their glasses, which are produced from spherical nanoparticles by mechanical stretching of the heated up glass.

Usually these materials are manufactured from glass exchanged in a salt melt. This is a time-consuming process involving hazardous chemicals. Recently such glasses have been produced in a simpler way by replacing the exchange in a salt melt with a field-assisted ion exchange from solid silver [70, 71]. One aim of this work is to improve this manufacturing process, and to do it based on the common standard optical glass B270.

The ion exchange process was quite well analysed in the past for manufacturing of waveguides in glass [72, 73]. Nanoparticle formation was an unwanted process in this though, and the glasses were chosen accordingly. Since a different glass has to be used a further analysis is required to characterise its specific behaviour. The ion exchange process is covered in this chapter, while the glasses with silver nanoparticles are covered in more detail in chapter 3.

The glass-silver composite is manufactured by laser irradiation of the ion exchanged glass presented in this chapter. It is a newly discovered material, which is analysed in chapter 4.

The first part of this chapter describes the theoretical background of the ion exchange process. In the second part materials, experimental procedures and devices are described. The third part shows the experimental results of the ion exchange process and the characterisation of the produced ion exchanged glasses, which are used for manufacturing the metal glass nanocomposites, which are presented in chapter 3. The fourth part shows results on ion exchange with copper and gold ions.

2.1. Theoretical background

At room temperature soda lime glass is an outstanding insulator. When it is heated up to 300°C this is no longer the case because the mobility of anions embedded in the glass matrix, is distinctly increased. It behaves like a solid electrolyte, showing ionic conduction. Applying an electric field results in anions moving away from the anode towards the cathode where they are neutralised. This is utilised in field-assisted ion exchange, where the anode consists of a metallic silver film. That is providing silver ions, which are filling the vacancies left by positive ions moving away when an electric field is applied. This process is utilised for manufacturing the ion exchanged glasses used in this work, and is covered in more detail in section 2.1.3.

2.1.1. Ionic diffusion and conduction in glass

Ionic movement in solid matter usually occurs by a hopping process between localised states in the glass matrix [74]. The hopping mechanism is subject of many

controversies. In a first approximation it can be described by Fick's laws. Fick's first law relates the diffusive flux vector $\vec{j}_D$ of a diffusing species to the gradient of its concentration *c*:

$$\vec{j}_D = -D\vec{\nabla} c \tag{2.1}$$

where *c* is the volume concentration of the diffusing species. *D* is the diffusion coefficient.

Fick's second law follows from the first law and mass conservation and describes the change of concentration over time:

$$\dot{c} = D\nabla^2 c \tag{2.2}$$

where $\dot{c}$ is the time derivative of the concentration.

This can be solved analytically for a diffusion starting with an infinite step profile with the concentration changing from 0 to 1 at x=0. The solutions are:

$$c = \frac{1}{2} erf\left(\frac{x}{\sqrt{2Dt}}\right) + \frac{1}{2} \tag{2.3}$$

Since the profile is infinite it does not include any effects of object boundaries. The concentration profile starts with c=1 for all x>0, which represents an infinite supply, while the x<0 half space is representing an infinite sink. This always keeps the concentration at 0.5 at x=0. In an ion exchanged glass the are with c=1 would be limited by the glass surface. If there is no ion exchange at the surface the concentration at the surface inside the glass can decrease quite far below 1, given a long enough diffusion time. In this situation this formula would give wrong results, though for shorter diffusion times where the surface concentration does not decrease much it would be appropriate.

Cations in glass are fixed in their location due to the bound negative charges in the glass matrix. These negative charges result in a potential well for the positive ion. An activation energy E_A is required to overcome the potential well. The energy of ions is proportional to the temperature. The temperature dependence of diffusion coefficients of ions in glass generally follows an Arrhenius equation:

$$D = D_0 e^{-E_A/RT} \tag{2.4}$$

where k is the Boltzmann constant and R the Gas constant.

The electric current induced by an electric field is proportional to the field strength:

$$\vec{j} = \sigma \vec{E} \tag{2.5}$$

where σ is the conductivity and $\vec{j}$ the electric current density.

Diffusion and ionic conduction are related processes. An external electric field increases the probability for a cation to jump in the direction parallel to the electric field towards the cathode. If conductivity and diffusion are due to identical processes, i.e. there is no diffusion of neutral pairs, then diffusion coefficient D and ionic conductivity σ are related over the Nernst-Einstein relation:

$$\frac{\sigma}{D} = \frac{c q^2}{f k T} \tag{2.6}$$

where q is the ionic charge, k the Boltzmann constant and T the temperature in K. f is a correlation factor that expresses a difference in diffusive and electrical diffusion coefficients, which is in the range of 0.2 to 1 [75]. This difference is a consequence of the correlation of subsequent ion jumps in thermal diffusion. There is an increased probability that an ion jumps back to its former location, which is not the case for jumps induced by an electric field [72].

The particle current density $\vec{j}_p$ and the electric current density due to particle motion are related by:

$$\vec{j}_p = \frac{\vec{j}}{q} \tag{2.7}$$

From this follows for the particle current:

$$\vec{j}_p = \frac{D\,c\,q}{f\,k\,T}\vec{E} \tag{2.8}$$

2.1.2. Ion diffusion coefficients in glass

For silver ion exchange it is most interesting to know the diffusion behaviour of silver ions. In this ion exchange Ag^+ are replacing other monovalent cations present in the glass, mainly sodium ions since these have a vastly higher diffusion constant than the other ions present in B270.

In the literature diffusion coefficients can be found for different ions in glasses with different compositions. There are two different ways to qualify diffusion. It can be characterised by the Ag^+ concentration profiles resulting from ion exchange. Since Ag^+ is replacing Na^+ this is also called the silver-sodium interdiffusion coefficient. Diffusion coefficients of silver and sodium can also be evaluated individually by using radioactive tracers. This is called the self diffusion coefficient.

For Ag ions in B270 glass Zhang [76] identified the following interdiffusion coefficients:

300°C: $D = 0.5 \cdot 10^{-12}$ cm²/s

320°C: $D = 1.3 \cdot 10^{-12}$ cm²/s

350°C: $D = 4.5 \cdot 10^{-12}$ cm²/s

and found an activation energy of 134 kJ/mol.

The conductivity of B270 is related to the diffusion coefficients of ions present in the glass, and is therefore also temperature-dependent. Values can be found in data sheets [77]. The conductivity of B270 is plotted in fig 2.1.

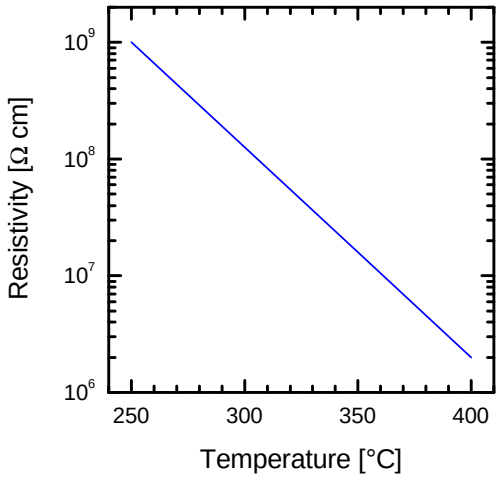

Fig. 2.1: Temperature dependence of the conductivity of B270 glass

From this the diffusion constant of Na^+ can be obtained with equation 2.6, assuming that conduction is carried completely by sodium ions. The concentration of Na^+ can be calculated from the known composition and density of B270 glass. It is $4.9 \cdot 10^{27}$ m^{-3}. The correlation factor is set to 1. With this the self diffusion coefficients of Na^+ have been calculated:

Table 1: Self diffusion coefficients of sodium ions in B270

T [°C]	ρ_D [Ω cm]	D [cm²/s]
250	10^9	$5.7 \cdot 10^{-14}$
350	$1.6 \cdot 10^7$	$4.3 \cdot 10^{-12}$
400	$2 \cdot 10^6$	$3.7 \cdot 10^{-11}$

From an Arrhenius plot of these diffusion constants (ln D vs. 1/T) an activation energy of 124 kJ/mol has been found.

Interestingly the ion mobilities at 350°C are nearly identical for the Ag-Na interdiffusion coefficient for thermal diffusion and for the Na^+ self diffusion coefficient found from resistivity. Self diffusion coefficients found in the literature are higher for Na^+ than for Ag^+. The ratio of the two depends on the glass compositions. Values reported are in the range from 1.4 [78] to 12 [79], often around 10 [80].

2.1.3. Field-assisted ion exchange

A common approach for silver ion exchange is to immerse glass in a salt melt which supplies silver ions. Often used is a mixture with a few percent silver nitrate in potassium nitrate [81] or sodium nitrate [51]. This melt is heated up to 300 to 400°C, and silver ions are moving into the glass due to thermal diffusion. This is a slow process, often taking several hours. Silver nitrate is a hazardous chemical that should not get in contact with skin. The temperature range is limited by the melting temperature of the salts and the decomposition of silver nitrate at 440°C. An advantage is the option to change the silver concentration in the salt melt, allowing to create glasses with low silver concentration over a quite large range of glass thicknesses.

Silver ions are replacing mainly sodium ions because these are the most mobile ions present in B270 and common soda lime glasses. Na^+ has a much higher diffusion coefficient than e.g. potassium ions. In diffusive ion exchange sodium ions are diffusing out of the glass at its surface and are replaced by silver ions. These can diffuse deeper into the glass, while sodium ions are moving to the surface. All movements are random and all directions of diffusion have the same probability, though the concentration gradient of the diffusing species results in a net movement of both ionic species.

The ion exchange can be accelerated by an electric current [72]. For this salt melts are forming *two* liquid electrodes on the glass, which have to be sealed and isolated from each other to avoid short circuits. Here both diffusing species are moving in the same direction following the electric field. Sodium ions are moving out of the glass at the negative cathode, and the electric field leads to an ionic current of sodium ions inside the glass. This opens vacancies at the positive side of the glass, which are filled by silver ions from the salt melt at the anode. This method is used only rarely because the sealing of the two electrodes is difficult.

Another possible ion source is a silver film which has been evaporated onto the glass. Thermal diffusion of silver from this metallic film is negligible at usual process temperatures [82]. Though an electric voltage can be applied easily to the silver film, which can induce a quick ion exchange resulting in a high silver ion concentration in the glass. An advantage of this process is that the amount of exchanged silver can be obtained by measuring the electric charge transfer during the process, since ion exchange due to thermal diffusion is negligible [72, 83]. The charge transfer can be obtained simply by integrating the electric current over time. This ion exchange from a metallic silver film is used in this work.

Ion exchange with silver leads to an increase of the refractive index of the glass. The index change is nearly proportional to the silver concentration and can reach values of around 0.1. It is caused by the larger ion radius and larger polarisability of Ag^+ compared to Na^+ [84].

Also sodium-silver ion exchange causes a volume increase of the glass. If the ion exchanged layer is thin compared to the thickness of the glass then the glass can not

expand in lateral directions. It results in mechanical stress, which contributes to the refractive index change. For potassium ion exchange the increase is around 4% [85]. Such compressive surface stress can drastically increase the surface strength by reducing the weakening effect of surface defects [86]. This is used nowadays to increase the resistance to scratches of the famous Gorilla glass.

For silver the volume increase is about 60% of that of K^+ ion exchange [72], which is 2.5%. No stress forms perpendicular to the surface since the glass can expand in this direction. The lateral stress induces a refractive index change on the order of 10^{-3}, causing a slight birefringence of the ion exchanged layer [72, 85].

The ion concentration profiles after field assisted ion exchange can be calculated by taking the effects of thermal diffusion and field-induced particle current into account. The diffusive particle current of equation 2.1 and the field-induced particle current given in equation 2.8 can be added to obtain the total currents of Ag^+ and Na^+ ions [73]:

$$\vec{j}_{Ag^+} = D_{Ag^+} \frac{c_{Ag^+} e}{f k T} \vec{E} - D_{Ag^+} \nabla c_{Ag^+} \tag{2.9}$$

$$\vec{j}_{Na^+} = D_{Na^+} \frac{c_{Na^+} e}{f k T} \vec{E} - D_{Na^+} \nabla c_{Na^+} \tag{2.10}$$

If no ion vacancies are forming and interdiffusion with other ions can be neglected the sum of both ion concentrations stays constant in every volume element:

$$c_{Ag^+} + c_{Na^+} = c_0 \tag{2.11}$$

Because the total ion concentration c_0 is constant we obtain another condition:

$$\nabla c_{Ag^+} + \nabla c_{Na^+} = 0 \tag{2.12}$$

The silver concentration is replaced with a normalised concentration $C = c_{Ag}/c_0$, which

can have values between 0 and 1. With Fick's second law (eq. 2.2) the time evolution of the ion concentration profile can be obtained [73]:

$$\frac{\partial C}{\partial t}=\frac{D}{1-C(1-M)}\left(\Delta C+\frac{(1-M)(\nabla C)^2}{1-C(1-M)}-\frac{q\vec{E}}{kT}\nabla C\right) \tag{2.13}$$

with $M=D_{Ag^+}/D_{Na^+}$ and D_{Ag^+} relabelled as *D*. The first term in the large bracket represents the thermal diffusion, the second term internal field drift and the third term external field drift.

This equation can be solved analytically in one dimension if it is assumed that the silver concentration follows a constant profile which is moving deeper into the glass during ion exchange. This approximation is quite accurate for exchange times long enough to achieve a nearly complete ion exchange (surface concentration close to C = 1) at the surface. Then the solution is:

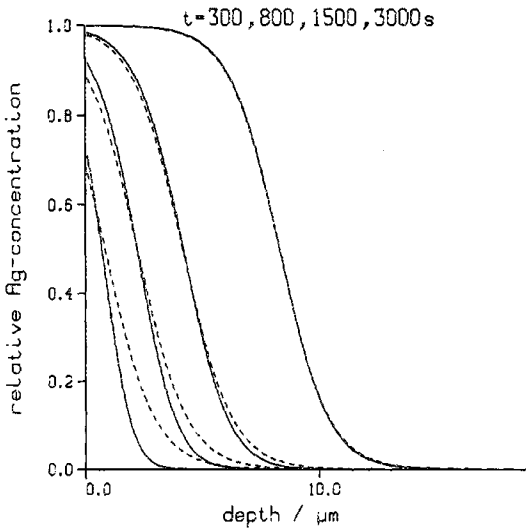

Fig. 2.2: Theoretical silver concentration profiles after field assisted ion exchange. Straight lines are numerical solutions, dashed lines analytical approximation according to eq. 2.14. The approximation is accurate for long exchange times. Graph from [78]

$$C(x)=\left(1+\exp\frac{J_0(1-M)}{D_{Ag^+}}(x-J_0t)\right)^{-1} \tag{2.14}$$

where J_0 is the total particle current divided by c_0. Fig. 2.2 Shows silver concentration profiles simulated numerically according to eq. 2.13 and profiles calculated with eq. 2.14 for comparison, taken from [78]. There is no difference between the profiles for 3000s ion exchange.

These profiles differ considerably from profiles resulting from ion exchange by thermal diffusion. By field-assisted ion exchange nearly rectangular ion distributions can be achieved if thermal diffusion is negligible [87]. If thermal diffusion occurs during field-assisted ion exchange this steep distribution gets smeared out. Ion exchange by thermal diffusion without an electric field produces different profiles. Complete ion exchange can only be achieved directly at the surface since Ag^+ ions can only be added to the glass as long as they can replace other ions at the surface. Therefore a thermal ion exchange with high concentration always results in a concentration profile decaying from the surface.

In glasses with more than one type of ions the self diffusion coefficients and conductivity depend on the concentration of all ions.

There are discrepancies between concentration profiles calculated by this simple method and experimental profiles. This is due to not taking diffusion of other ions present in the glass into account and due to an anomaly of glasses called the mixed alkali effect or mixed ion effect [73, 88]. This is an anomalous behaviour of the diffusion coefficients which become dependent on the ion concentrations in the glass. The effect has not been explained completely yet, but it is for certain that it is related to the formation of different site environments for ions with different radii, and to the formation of percolation pathways for the majority ion [88].

The ionic radius of Ag^+ is 126pm, while that of Na^+ is only 97pm. Therefore there is a relaxation of the surrounding glass matrix after an ion is replaced, resulting in different bond lengths and oxygen coordination numbers for Ag^+ and Na^+. While Na^+ forms ionic bonds with an oxygen coordination number of 5 the Ag^+ sites have a smaller bond

length and generally show covalent characteristics similar to Ag_2O, and an oxygen coordination number of 2 to 3 [89].

2.1.4. Ion depletion of glass

A different glass-changing process can be induced if the silver film at the anode is replaced with an anode that does not supply cations, for example graphite. Then the application of a voltage at elevated temperatures will still induce diffusion of Na^+ from the anode to the cathode. Cation vacancies are forming under the anode, leaving a negative charge in the form of non-bridging oxygen.

Sodium ions are moving first since they have the highest ionic mobility. This reduces the conductivity in the sodium-depleted layer. Thus a larger part of the applied voltage is dropping over this thin layer, resulting in a very strong electric field. This higher field strength induces the migration of less mobile cations, namely K^+ and Ca^+. This results in a profile of the ion concentrations similar to fig 2.3. This figure also shows H^+ ions, which are forming due to electrolysis of water which is adsorbed at the glass surface or diffused into the glass. Though the length scale of this graph is small, making the amount of hydrogen negligible for processes with larger charge transfer.

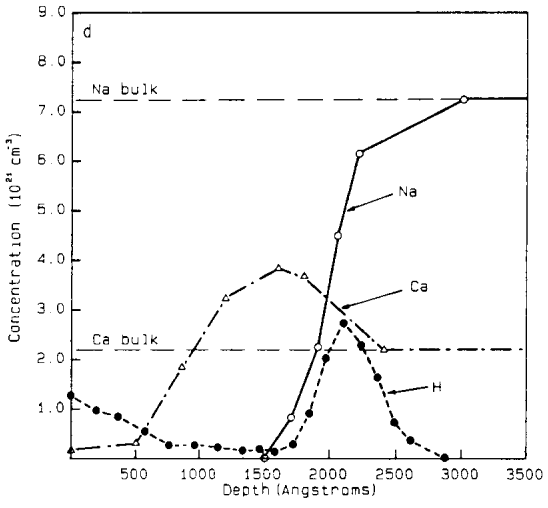

Fig. 2.3: Ionic distribution close to the surface of an ion-depleted soda lime glass, subjected to a charge transfer of 0.025As/cm². From [90].

With the further decreasing conductivity the field strength increases further. The field increases to field strengths close to

dielectric breakdown of the material [91]. This and the strive for local charge neutrality are driving the remaining negative charges in form of electrons to the anode. At this stage the glass modification becomes irreversible [92].

These processes occur in a layer of the glass which is called the dissociation zone. Over time it is moving deeper into the glass, and the thickness of ion-depleted glass is growing over time. The voltage drop over this ion-depleted layer decreases the field strength and therefore the speed of ion depletion. If the field strength is no longer sufficient to induce charge separation and to overcome diffusion the process is eventually coming to a halt.

Characteristic for ion depletion is a decrease of the volume of the glass, which results in the formation of microscopic cracks in the surface. For a glass consisting of 80% SiO_2 and 20% Na_2O the volume decreases by up to 20% [92].

If the glass is cooled down while the voltage is still applied a persistent electric field is created in the glass. This process is called poling [93-95]. This creates a second order nonlinearity in the glass, which is attributed to the breaking of the inversion symmetry due to the frozen-in electric field..

If a glass containing silver nanoparticles is subjected to ion depletion this can result in the dissolution of nanoparticles in the ion-depleted layer [96]. Localised dissolution can be used to create nanostructures of metallic nanoparticles [27].

2.2. Experimental methods

2.2.1. The ion exchange setup

The field assisted ion exchange is done in a furnace of the type Carbolite RWF. The ion exchanged glass is placed inside the oven between two electrodes. These are connected to an external power supply. A high voltage is provided to the electrodes for a controlled time, and the current flow is monitored. A schematic of the setup is show in fig. 2.4.

The sample holder with the two electrodes is shown in fig. 2.5. The electrodes are held and isolated by ceramic plates, which are pressed together by screws on the four corners. The glass with a silver film on one side is placed between the electrodes, with a graphite foil on both sides of the glass. The graphite foil ensures a good contact on the negative side due to its flexibility. It acts as a non-blocking electrode since it accepts sodium ions [92]. This results in much lower ion exchange voltage than with for example a silicon electrode. The graphite foil is also always providing a fresh surface clean of contaminants from earlier experiments, for example sodium which is coming out of the glass at the negative side. And it acts as a spacer, confining the contact area.

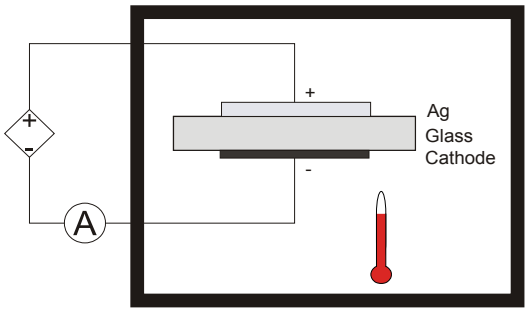

Fig. 2.4: Schematic of the field assisted ion exchange setup. The glass is placed in a furnace between two electrodes, which are connected to a high voltage power supply.

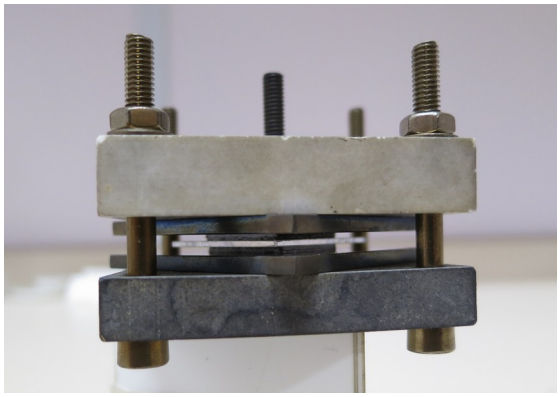

Fig. 2.5: In the sample holder the glass is fixed between two metal electrodes

It is important to ascertain that all used materials can withstand the temperatures that occur during experiments. Also mechanical stress due to different thermal expansion coefficients has to be avoided. This problem is mitigated by the arrangement of electrodes and holding plates and screws, which gives lateral flexibility, and by the flexibility of the graphite foil, which gives vertical flexibility. Still, materials were chosen which do not differ much in their thermal expansion coefficients. Thermal expansion coefficients and maximum operating temperatures are listed in table 2.

Table 2: Materials used inside the furnace, their thermal expansion coefficients and maximum operating temperatures

Material	Thermal expansion coefficient [K^{-1}]	Maximum continuous temperature [°C]	Maximum short time temperature [°C]
B270 glass	$9 \cdot 10^{-6}$	533	
MACOR ceramic	$10 \cdot 10^{-6}$	800	1000
Alumina ceramic	$5.4 \cdot 10^{-6}$	1700	
Steel	$13 \cdot 10^{-6}$	800	
Brass	$19 \cdot 10^{-6}$	450	
Nickel wires		600	750
Graphite foil		550	

The sample holder is connected to a high voltage power supply. It should be mentioned here that the used nickel wires are not ideal for this purpose since they do not resist the high voltages used. Appropriate wires which resist experimental voltages and temperatures were only available when ordered on the scale of kilometres. Health safety is still ensured though since the wires are placed inside the oven and a warning label is placed on it.

The power supply is of the type F.U.G. HCP 35-6500. It can supply voltages up to

6500V at currents up to 5mA. Limits for both voltage and current can be set. The negative pole of the output voltage is grounded. This power supply offers a quite accurate output voltage control, with a high stability and very low ripple of typically $5 \cdot 10^{-5}$ peak to peak. It has a built-in USB controller. It offers functions to set voltage and current limits, and to read out the actual voltage and current.

Over the USB controller the power supply is connected to a computer and controlled by a self-written program. Beside the basic controlling and monitoring functions it offers recording, plotting and saving of data, and a simple script language with timer functionalities for experiment automation.

2.2.2. Sample preparation process

A piece of glass is cut to proper dimensions and then cleaned with acetone. This is sufficient to remove the usual residuals. Subsequent cleaning with deionised water removes any marks left by the acetone. After the cleaning a silver film is created on the glass. This is done by applying a suspension of silver flakes (10µm) in isopropanol, followed by sintering at 300°C for 20 mins. During this sintering the silver flakes are turning into a solid film of light brown colour. Scratching the surface reveals a solid metallic silver film under a thin surface film. A typical

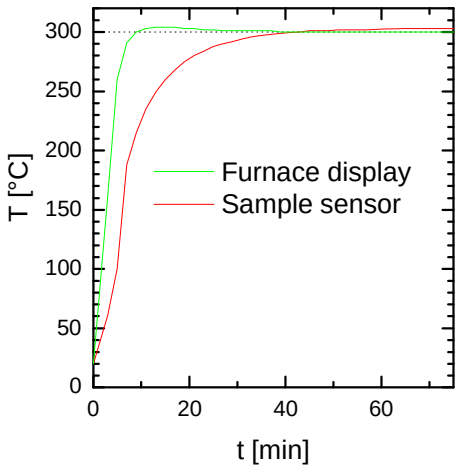

Fig. 2.6: Timing diagra of sample heat up to 300°C in the furnace. A thermal sensor was placed in contact with a glass sample; furnace and sample were heated up from room temperature. The sample reaches the set temperature after 40 mins.

thickness of the silver film is 15µm..

The glass with silver film is then pressed between the two electrodes within the sample holder, together with the graphite foil on both sides. The sample holder is placed into the furnace and connected to the power supply, with the positive voltage connected to the Ag side. The furnace is set to heat up to usually 300°C. It is taking about 40 mins until the sample inside the sample holder reaches the set temperature of 300°C (see fig. 2.6). 50 mins after starting heat-up the voltage is turned on, and automatically turned off after the set time. Current-time dynamics are recorded during the ion exchange.

Shortly after the ion exchange is finished the sample holder with the glass sample is removed from the furnace. After cooling down the sample is cleaned with a scalpel and deionised water, followed by rubbing with a cleaning tissue and water. This allows easy removal of the graphite foil and the remaining silver film.

2.3. Silver ion exchange results

After a view early tries a temperature of 300°C was chosen for all presented ion exchange experiments. Lower temperatures resulted in very low electric currents. Voltage was varied in a range from 100 to 1000V. Fig. 2.7 shows the current curves recorded during experiments done with different voltages. For 100V the current stays nearly

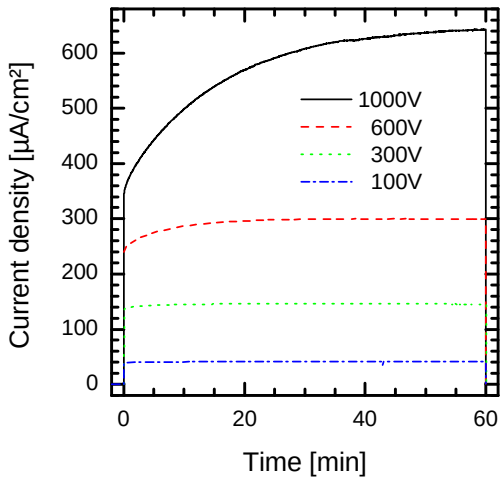

Fig. 2.7: Ion exchange current densities different exchange voltages at 300°C.

constant, while for higher voltages the current curves show a clear increase of the current over time. At 1000V the current density rises from 360 to 640 µA/cm^2. The initial current for the different voltages is about proportional to the voltage.

Kapila [97] proposed that the growth of a metal oxide layer between metal film and glass is causing this current increase. This oxide layer would form from oxygen that originates from the glass, and would be the actual source of silver ions. Silver oxide decomposes above 230°C though, which is considerably lower than our process temperature. Other mechanisms can be an increase in the number of charge carriers and rearrangements in the glass matrix that increase the ion mobility.

For the later experiments the thickness of the ion exchanged layer is most important. This was measured in electron microscopy images taken in backscattering mode. For this cross sections of the glasses were prepared by scratching the glass from the back side with a glass cutter and breaking it. This often leaves a straight intact edge at the ion ion exchanged layer on the other side. Polishing is not done because it is breaking off the ion exchanged layer at the edge due to mechanical stresses in the glass caused by the

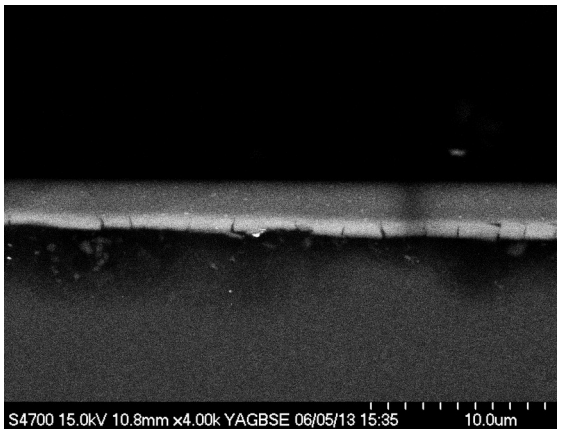

Fig. 2.8: SEM image of cross section of sample exchanged at 100 V. The ion exchanged layer shows as bright bar. Its thickness is 2.7 µm

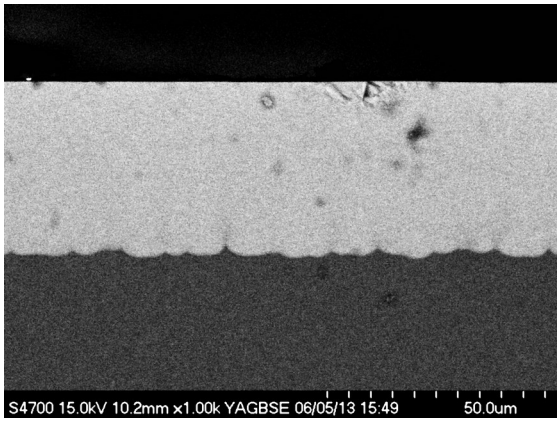

Fig. 2.9: SEM image of cross section of sample exchanged at 1000 V. The thickness of the ion exchanged layer is 46 µm.

volume change during ion exchange. Images of the cross sections of the 100V and 1000V ion exchanged samples are shown in fig. 2.8 and 2.9.

Such images were taken from all four samples which were exchanged with different voltages. Thicknesses were measured and are plotted as a function of the charge transfer density in fig. 2.10. The charge transfer density was calculated by integrating the current density over the processing time.

The points in fig. 2.10 are very close to a linear function with a slope of 16.2 ± 1.4 µm / (As cm^{-2}). This is equal to a charge transfer of $3.9 \cdot 10^{21}$ electron charges per cm^3. The sodium content of B270 is $4.9 \cdot 10^{21}$ per cm^3. These values are quite close to each other as it would be expected for a complete sodium-silver ion exchange. The slightly smaller charge transfer density indicates that about 80% of the sodium ions are replaced with silver ions. This means that the silver concentration is 5.5 at-% in the ion exchanged layer since B270 contains 6.9at-% Na^+ ions.

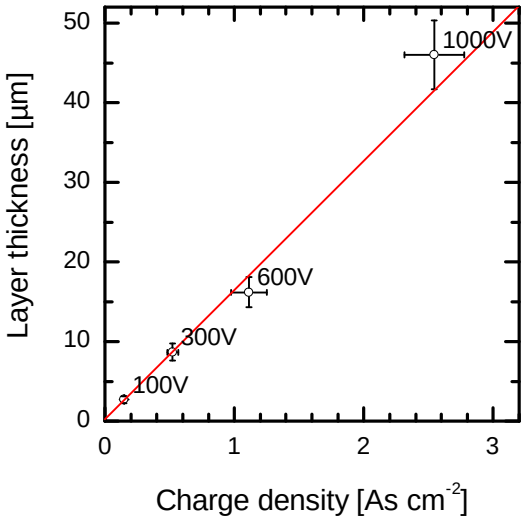

Fig. 2.10: Thickness of ion-exchanged layer as a function of charge transfer density for different voltages applied during ion exchange.

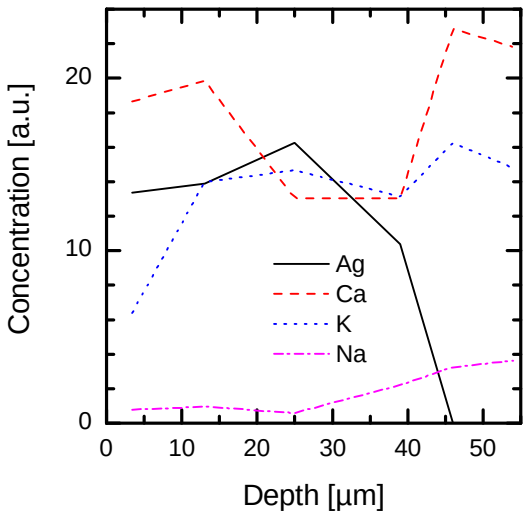

Fig. 2.11: Elemental composition profile of the cross section of a glass sample exchanged at 1000 V.

2.3.1. Elemental composition profile

The composition of the cross section of the 1kV exchanged sample shown in fig. 2.9 was analysed by EDX. The obtained concentration profile for the diffusing ions is shown in fig. 2.11. It shows the profile of silver concentration, which has replaced sodium ions over a depth of 40µm. The sodium concentration is very low within this ion exchanged layer, but it is also reduced below that layer. Potassium concentration is only lowered directly at the surface, but unaffected deeper in the ion exchanged layer.

2.3.2. Effects on negative glass side

In a field-assisted sodium-silver ion exchange sodium ions are driven out of the glass on the negative glass side. We are using a graphite film, which is taking up this sodium. After ion exchange the film is connected firmly to the glass, but can be removed easily with water. Presumably this connection is due to small amounts of metallic sodium or sodium oxide, which are both reacting with water to soluble NaOH. However after cleaning the glass surface looks white and rough. Analysis by microscope reveals that the glass surface is damaged, showing holes with a depth of up to 5µm (fig. 2.12). This

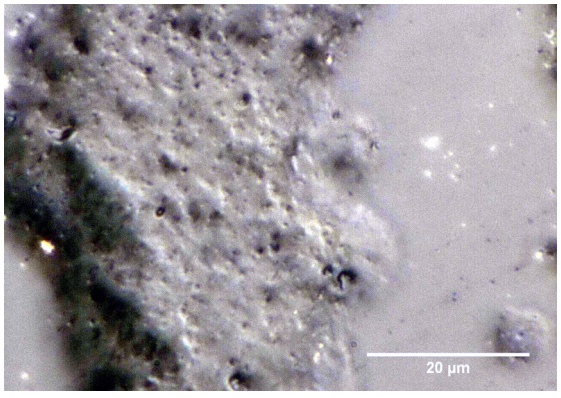

Fig. 2.12: Microscope image of a damage of the glass at the negative electrode

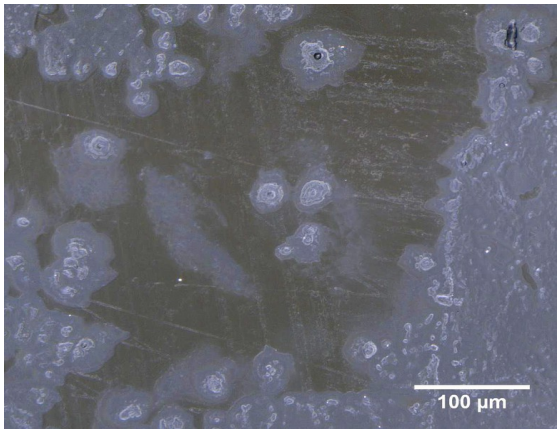

Fig. 2.13: Brown surface change on negative glass side

image and all other analyses of these negative contact effects are obtained on a 1000V for 1h ion exchanged sample.

For large electrodes with a border length of at least 20mm a different effect occurs on the negative glass side, resulting in a brown colour. A microscope image of such a change is shown in fig. 2.13. Interestingly there are no hole damages in the area with brown colour change and in a border region with a width of 5 to 25µm. These brown changes occur only in the centre of the negative electrode, the border region with a width of more than 5mm contains only white hole damages. The extent of these brown areas varies between samples. It has been observed that the current density during ion exchange is up to 20% higher when brown areas occur.

Both effects and all observations can be explained by the occurrence of an ion exchange process in the brown areas and ion depletion causing the hole damages. Since the process occurs at the negative electrode this must be due to negative ions. Negative charges in glass are in the form of non-bridging oxygen, which must be the ion that is depleted in the damaged areas. The negative electrode is not providing any negative ions in these areas, which results in quite strong electric fields capable of driving non-bridging oxygen out of the glass. In the brown areas an ion exchange occurs, which prevents these strong electric fields in these and the adjacent areas.

The ion which is brought into the glass in the brown areas must be a negative ion, since this effect occurs at the negative electrode. The effect does not occur at the border of the electrode, which indicates that the responsible substance is evaporated from the outer areas of the electrode. Also the usual cleaning with IPA and water does not remove that substance. It can not be oxygen ions since that would not induce any change in the glass

and therefore could not explain the colour change. A candidate for this would be hydroxide ions, which can form at the negative electrode from the electrolysis of water.

The interest of this work is on nanoparticles and metallic nanostructures created in the ion exchanged layer on the positive contact side of the glass. Therefore the altered layer on the negative contact side was removed from the glass by polishing to prevent any effect on optical measurements.

2.4. Summary and conclusions

Ion exchange with silver ions was performed on B270 glass. As exchange temperature 300°C were chosen. The electrical current flow was measured and recorded, and the transferred electrical charge determined. The thickness of the ion exchanged layer was determined from SEM images. A comparison of these two results confirmed a linear relation between charge transfer and layer thickness, with a transfer equivalent to about 80% of the sodium ions being replaced by silver ions. A specific layer thickness can be achieved by controlling the charge transferred per electrode area, the resulting thickness is 16.2 ± 1.4 µm / (As cm^{-2}). There were damages occurring at the negative side of the glass, which are attributed to oxygen ion depletion, while colour changes in that area are explained by hydroxide ion exchange.

3. Fabrication and characterisation of glass doped with silver nanoparticles

In this chapter glasses with silver nanoparticles which are made from the ion exchanged glasses introduced in chapter 2 are presented. These glasses are produced in a solid-state process, which is simpler than the ion exchange in a salt melt that is usually utilised for fabrication of glasses with silver nanoparticles. The aim of this chapter is to characterise the nanocomposites produced from the simpler solid state process. Parts of the results of this chapter were presented in publications [98, 99].

The ion-exchanged glasses are annealed in a furnace at a temperature around the glass transition temperature of B270, which is 531°C. Most samples are annealed at 550°C. This annealing induces the reduction of silver ions to atoms and their agglomeration to silver nanoparticles.

Samples are characterised by the optical characterisation methods introduced in section 1.5.1. Microscopical imaging gives an overview of areas with silver nanoparticles, showing homogeneity and surface structures. Transmission spectroscopy is used to analyse position, height and shape of the plasmon absorption band. This allows conclusions to be drawn about particle sizes and filling factors. The relation between these and transmission spectra can be found by theoretical simulations of plasmon band oscillations, which were presented in section 1.6.

Also cross sections of samples are analysed with a microscope spectrophotometer. For this thin slices of the cross section are prepared, and transmission spectra measured at different distances from the former sample surface. This allows the profiles of particle

concentration and size to be determined.

In the experimental section the effect of changing three different process parameters is analysed separately. In section 3.1.1 an analysis of the effect of different annealing times is presented. These different process durations allow the particle formation process and occurring diffusion processes to be examined, which are covered in section 3.3. Also the behaviour of glasses ion exchanged with different applied voltages is presented in section 3.1.2.

B270 glass is known to have a very low concentration of iron. Normally the redox reaction of Ag^{+} with Fe^{2+} to Ag^{0} and Fe^{3+} is considered as the reduction mechanism for the formation of silver nanoparticles in glass. In B270 reduction mechanisms must be different, and different processes that can occur are discussed in section 3.4.

3.1. Experimental results

Generating nanoparticles in the ion exchanged glass is a quite simple process. The furnace is preheated to the process temperature of 550°C. The glass is placed on an alumina plate, and that plate is put into the furnace with large temperature-resistant tweezers. When the desired processing time has passed the alumina plate with the glass sample is taken out of the furnace and is allowed to cool down quickly.

Heating and cooling times were kept short to not distort the processing time. A slow cooling would cause additional diffusion and agglomeration.

During the annealing silver ions are reduced to atoms and are agglomerating to silver nanoparticles. This results in a strong change of colour to yellow or brown, depending on the amount of nanoparticles present in the glass. Fig. 3.1 shows such a glass with

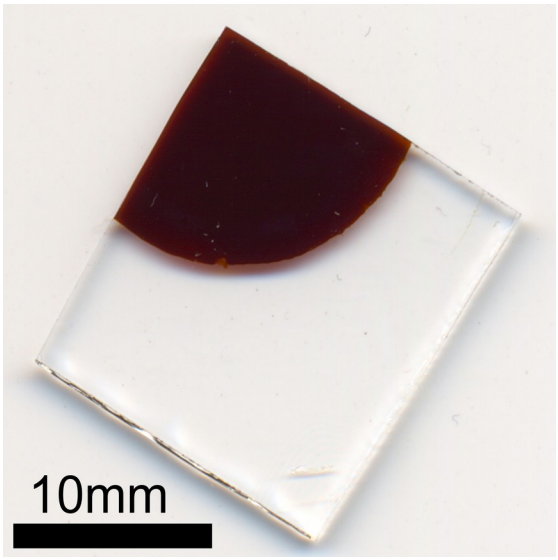

Fig. 3.1: Glass with silver nanoparticles produced from ion-exchanged glass by annealing at 550°C for 2 h. The ion exchange was done with a circular electrode at 300°C, 1000V for 1 h.

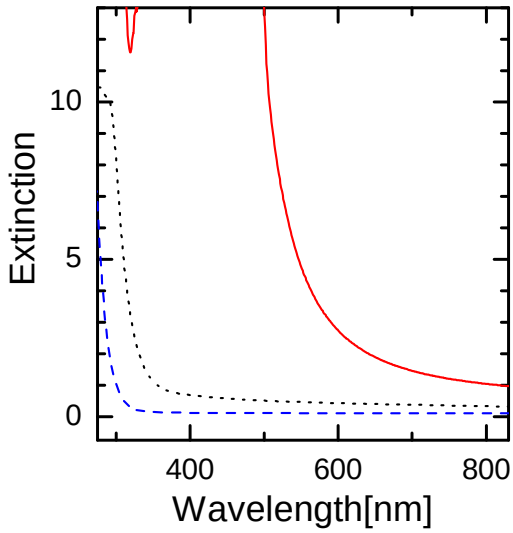

Fig. 3.2: Extinction spectrum of the glass with silvernanoparticles shown in fig. 3.1 (straight red curve). Extinction of B270 glass (dashed blue) and ion-exchanged glass (dotted black) for comparison.

silver nanoparticles, which was annealed for 48h at 550°C. The ion exchange was done with a circular silver electrode, and the ion-exchanged sample then was cut into four pieces, which were annealed for different annealing times. Fig 3.2 shows the extinction spectrum of the area with silver nanoparticles shown here. The plasmon band is centred at about 410nm. The height of the plasmon band is extremely high, making it impossible to measure with a spectrometer. The peak position is calculated as the average of the highest values measured at the flanks of the absorption band, so it is assumed that the cut off part of the band is symmetrical.

The ion-exchanged area looks very homogeneous, not showing any colour variation. To verify the homogeneity and to analyse the depth profile of the particle-containing layer a thin slice of a whole cross section was prepared. The location where the thin slice was cut from the glass sample is illustrated in fig. 3.3. The glass sample was embedded in

epoxy resin(Specifix-20, Struers Limited). This prevented chipping of the glass and made it manageable for grinding and polishing. All samples were polished down to a thickness of around 30µm.

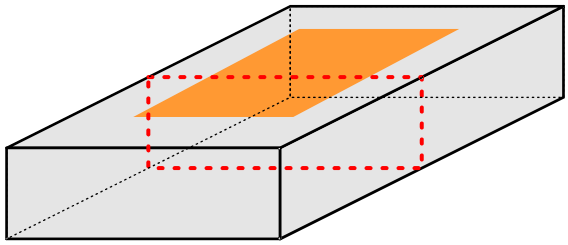

Fig. 3.3: Schematics showing where the thin slice was cut (dashed red square) from the glass sample with the area with silver nanoparticles

Fig. 3.4 shows a microscope image of the whole thin slice, which is split up over four lines. The border region between the treated and untreated area (edge of the electrode) can easily be identified. The thickness of the nanoparticle-containing layer is about 230 µm, and as it can be seen the nanoparticle-containing layer is homogeneously

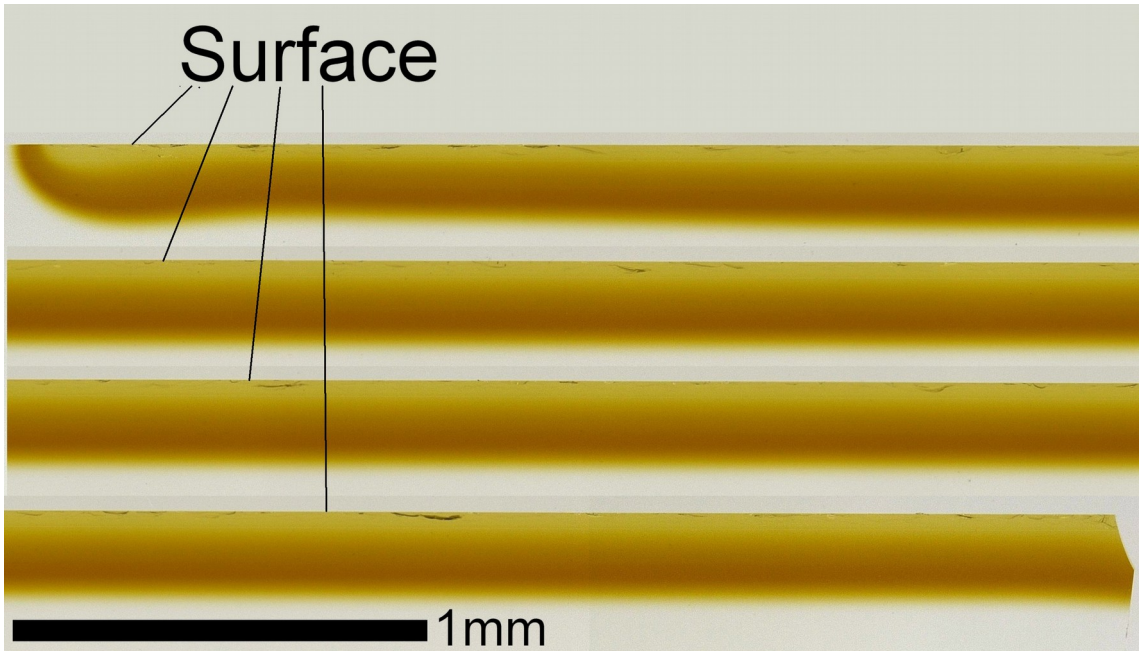

Fig. 3.4: Thin slice of the whole cross section of the ion-exchanged glass shown in fig. 3.1. Since the slice was too long it was split up into four sections, which are shown on top of each other. Colour changes slightly with depth. The colour profile is constant over the whole length of the thin slice, beside a small thickness variation at the beginning of the slice.

distributed throughout the sample. Only at the border (located in the top left corner of the slice) the profile is slightly disturbed due to the edge effects. This is where one of the edges of the electrode was placed. The lower layer is darker (dark yellow) in comparison to the area close to the surface (light yellow).

On this thin slice transmission spectra were measured with the microscope spectrophotometer. The probed sample area is limited by a rectangular diaphragm of 10µm×100µm. The spectra were taken every 10 µm across the cross section (20 spectra in total). The sum of the individual extinction spectra a_i can be fitted to the spectrum measured through the whole sample a_{tot} with the following formula:

$$a_{tot} = \frac{\Delta x}{l} \sum_i a_i + a_0 \tag{3.1}$$

where a_0 is a constant value taking surface reflections into account, Δx is the distance between the measuring points (10 µm) and l is the thickness of the thin slice. The resulting sum of spectra and the spectrum measured through the whole sample are shown in fig. 3.5.

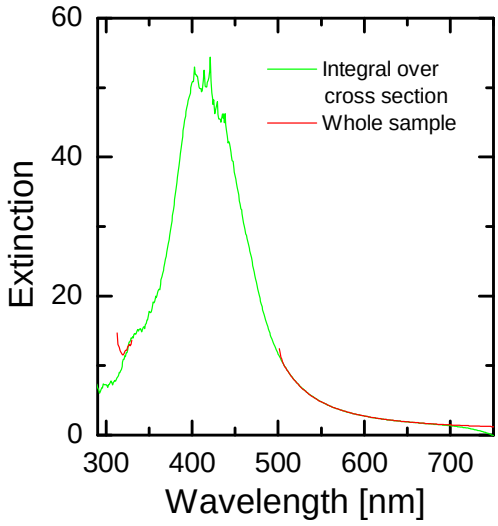

Fig. 3.5: Sum of all spectra measured on the thin slice of the cross section (green) and spectrum measured through the whole sample. The integral is fit to the whole spectrum with the thin slice thickness as a fitting parameter.

Fig. 3.6 shows the transmission spectra taken at different depths in the thin slice, converted to extinction coefficients in mm^{-1} with the now-known thickness of the thin slice. For the definition of extinction and absorption coefficient see eq. 1.5 and 1.6.

The depth where each spectrum was measured is assigned to the horizontal-axis, while the wavelength is assigned to the vertical-axis.

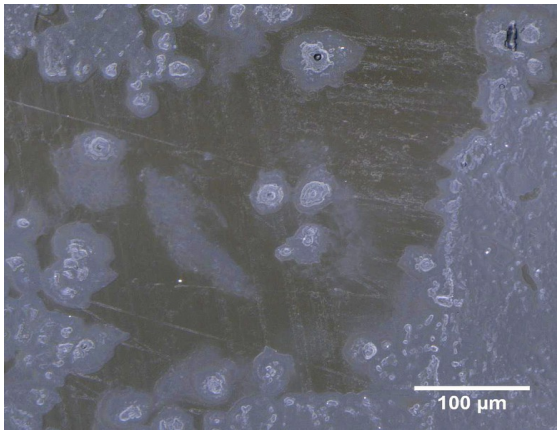

Fig. 3.6: Brown surface change on negative glass side

The darker contours in fig. 3.6 indicate higher absorbance. Each contour line is labelled with an individual value. In all depths shown in this fig. there is a plasmon band centred around 410 nm, corresponding to the formation of nanoparticles with diameters ranging from about 5 to 12 nm. The plasmon band becomes narrower for the area closer to the surface and becomes wider for lower layers. This is attributed to the formation of larger particles with lower number density closer to the surface (~ 8 – 12 nm in diameter) and smaller nanoparticles (~ 5 – 8 nm) with higher number density in the deeper layers.

Here, due to the high absorption, the surface plasmon band was mostly cut off making it very difficult to register the exact peak position and its small red shift caused by the spill-out effect of the nanoparticles [1, 57]. The spill-out effect of the electrons will lead to the volume-average mean electron density decreasing and consequently peak position red shifting. It is more prominent with decreasing particle size [100]. Although we were not able to register the red shift caused by the spill-out effect, nevertheless broadening of the plasmon band in the depth of the sample can clearly be seen from the spectra presented in Fig. 3.6.

3.1.1. Analysis of particle development by varying annealing duration

Following the analysis of the first thin slice a set of identical ion exchanged glasses was annealed for different durations. This allows to analyse how the nanoparticle containing layer is forming over time.

A piece of B270 ion-exchanged at 300°C with 1000V for 1h was cut into five pieces. These were annealed at 550°C, each for a different duration (1h, 2h, 4h, 8h, 48h). This resulted in the formation of silver nanoparticles inside the glass, changing the colour of the glass to dark yellow for short annealing times and brown for longer times. Extinction spectra of these five samples were measured and are shown in fig. 3.7. They show stronger absorption for longer annealing times.

Thin slices of cross sections were prepared of all five pieces, and spectral profiles measured with the microscope spectrometer. Spectra were measured every 1.5µm, the diaphragm limiting the measuring area was set to 20µm × 1.5µm. The slice thicknesses were determined by fitting the sum of all spectra of the cross section of a slice to the extinction measured through the whole glass, according to equation 3.1. The obtained slice thicknesses are 28.7µm for the 1h

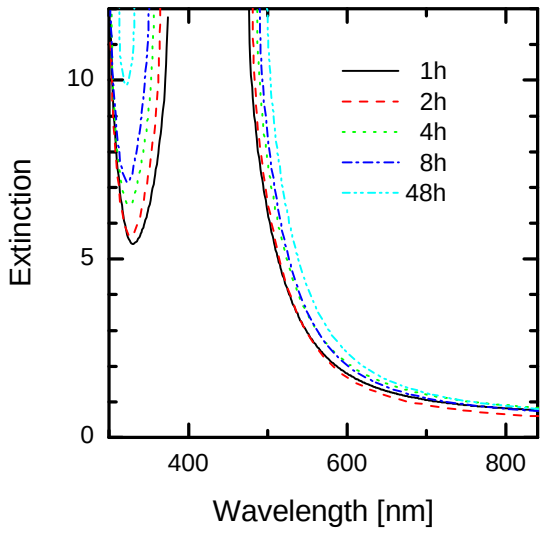

Fig. 3.7: Extinction spectra of glasses produced with different annealing durations. Longer annealing increases the extinction. The plasmon bands are centred at 410nm; the maximum is too high to be measured.

annealed slice, 34.0µm for 2h, 31.1µm for 4h, 23.4µm for 8h and 21.9µm for 48h.

Fig. 3.8a shows microscope images of the thin slices of the cross sections of the generated silver nanoparticle-containing layer. The former glass surfaces are at the top of the image, while the lower parts of the image show the layers deeper inside the glass. For short annealing times the nanoparticles cause a dark yellow colour close to the surface, which changes to brown at the inner end of the layer. For longer annealing times the colour at the surface changes to light yellow, while it turns to a darker yellow

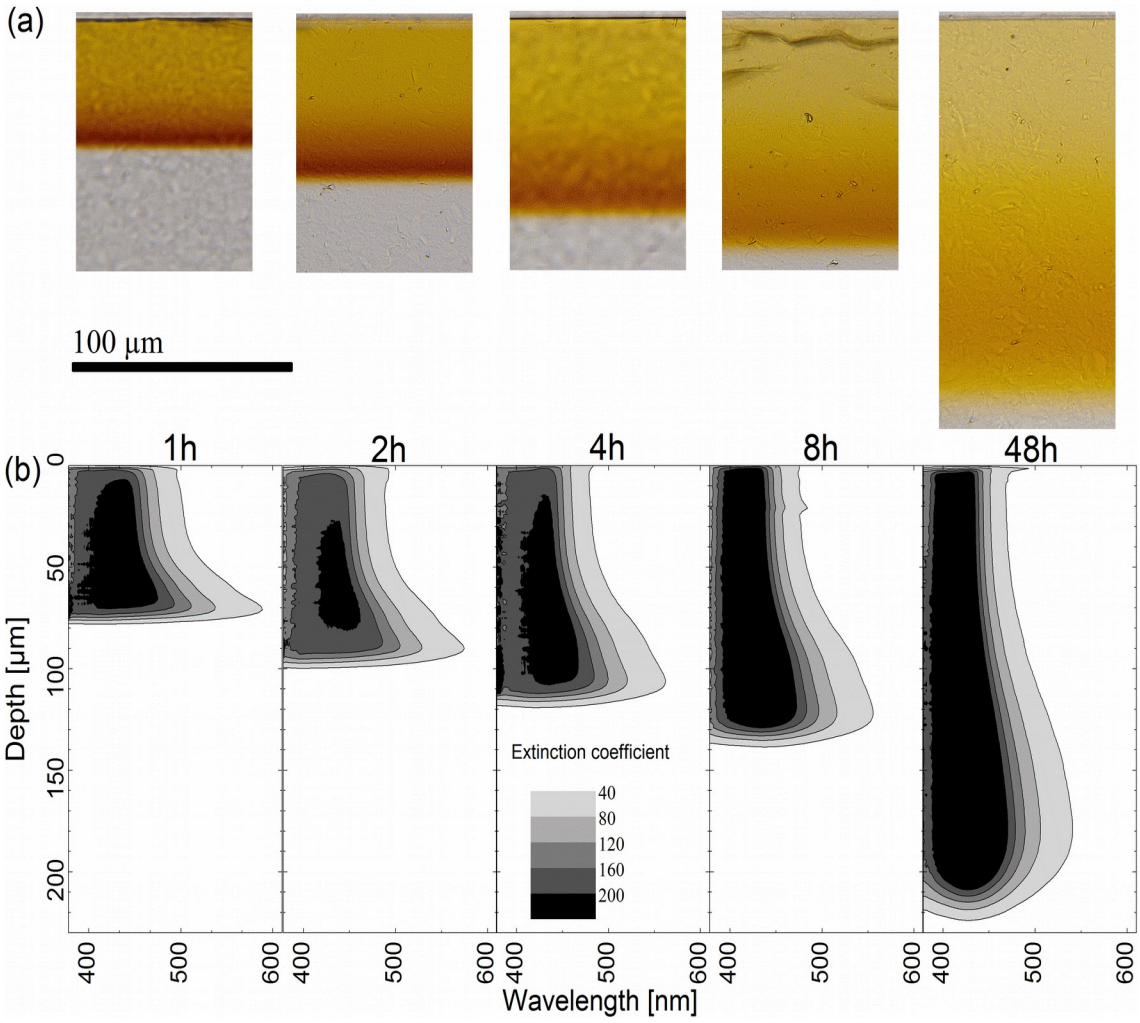

Fig. 3.8: Thin slices of the cross sections have been prepared from samples annealed for 5 different times (1h, 2h, 4h, 8h, 48h). The top pictures (a) show microscope images of the thin slices. The bottom images (b) show extinction coefficients [1/mm] of the five slices.

for the inner region.

Fig. 3.8b shows the extinction coefficient profiles calculated from the spectra measured on these thin slices. The depth in the glass is assigned to the vertical axis, while the wavelength is assigned to the horizontal axes. The former glass surface is at the top end. Darker colours stand for stronger extinction. For the 2h and 4h annealed samples the area with maximum extinction coefficient in the graph is reduced due to the limited measurable extinction and the higher thickness of these slices.

These graphs show how the plasmon band changes in the depth of the glass and with longer annealing times. For 1h annealing the plasmon band at the surface is centred at about 430 nm. In the lower layers the plasmon band becomes much wider, similar to the simulated plasmon bands for very small nanoparticles. Also in the deeper layers of the glass the absorbance decreases. Both effects are caused by a low amount of silver located in nanoparticles in this region.

The maximal absorbance could only be measured correctly for the deepest layers with lower particle concentrations because it was too high for most of the glass since the amount of NPs is too high. Therefore the exact plasmon band position and height could not be determined, but what has been measured allows making several conclusions.

For longer annealing times the silver spreads out into deeper layers. The nanoparticle-containing layer becomes thicker. Near the surface the plasmon band becomes narrower over time, which fits to the simulated spectra for growing particle sizes. This can either happen by the agglomeration of more silver or by Ostwald ripening [101]. In this process smaller NPs are dissolved and redeposited onto larger NPs. In the depths where the shorter-annealed samples have the wide plasmon band the width decreases strongly,

while the plasmon band width at the lowest edge of the profile is slightly lower for longer annealing times. This means that NPs already have a larger size when they reach a comparable concentration. Since the speed at which the thickness of the layers grows is decreasing we can conclude that the growth of the particle sizes does not slow down as much with longer annealing times as the growth of the layer thickness.

The spectral profiles are analysed more thoroughly in section 3.2.

3.1.2. Effect of different exchange voltages

Presented in chapter 2 were glasses ion-exchanged with different exchange voltages. Voltages used were 100, 300, 600 and 1000V. The exchange temperature was 300°C, the exchange duration 1h. In this section an investigation of the particle formation behaviour of these glasses exchanged with different voltages is presented.

For this the glasses were annealed at 550°C for 2h. Fig. 3.9 shows a photograph of the four samples, fig. 3.10 their extinction spectra. The reduction in voltage compared to the

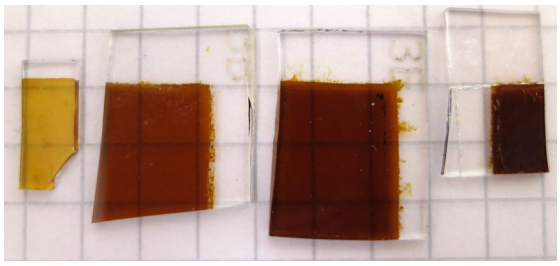

Fig. 3.9: Photograph of nanoparticle-containing glasses produced with different exchange voltage. From left: 100V, 300V, 600V, 1000V. Exchange was done at 300°C for 1h; afterwards the glasses were annealed at 550°C for 2h. The grid in the background is 5mm.

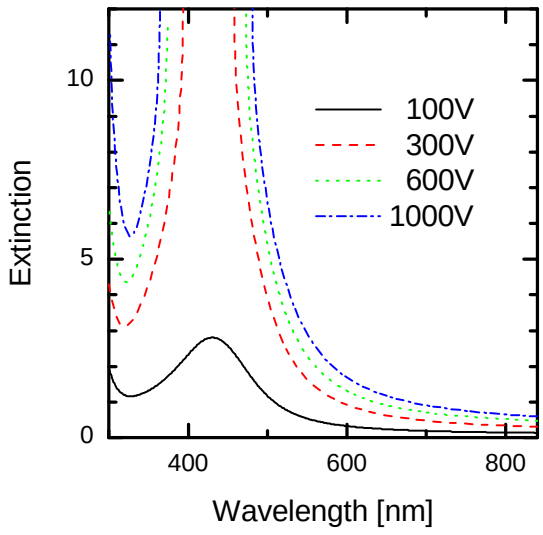

Fig. 3.10: Extinction spectra of the glasses shown in fig. 3.9

samples presented in the last chapter results in a lower height of the plasmon band. For the 100V ion exchanged sample the maximum extinction is reduced to 3. This lower height of the whole plasmon band results in a lighter brown colour for the 600 and the 300V sample, and a dark yellow colour for the 100V exchanged glass.

Of all these glasses thin slices of the cross sections were prepared. Transmission microscopical images are shown in fig. 3.11. Also spectral profiles of the cross section were measured with the microscope spectrometer. Spectra were measured every 1.5µm, with an iris of 20µm × 1.5µm. Thin slice thicknesses were determined by fitting the sum of the extinction spectra measured in the profile to the spectrum measured through the whole sample, using equation 3.1. The obtained thicknesses were 13.8µm for 100V, 24.6µm for 300V, 23.5µm for 600V, and 34.0µm for 1000V.

For the 100V sample the thickness of the nanoparticle-containing layer is very low, less than 10µm. Due to this the extinction measured through the thin slice was limited by straylight from above the thin slice and below the particle-containing layer. While for all other thin slices extinctions up to 6 were measured the extinction only reached 4.2 for

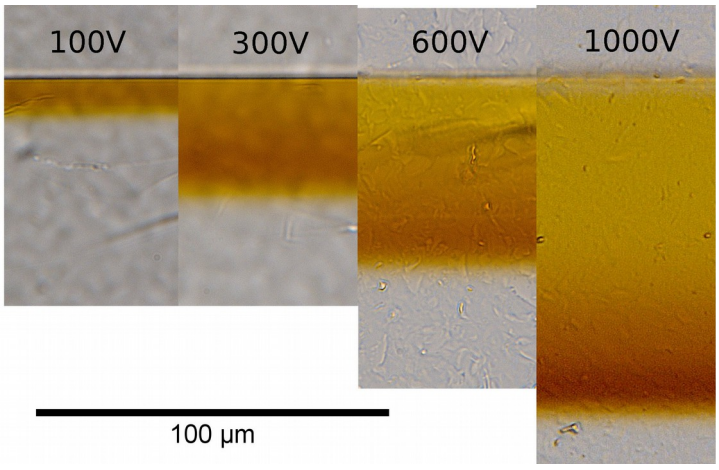

Fig. 3.11: Thin slices of the cross section of the samples exchanged with different voltages.

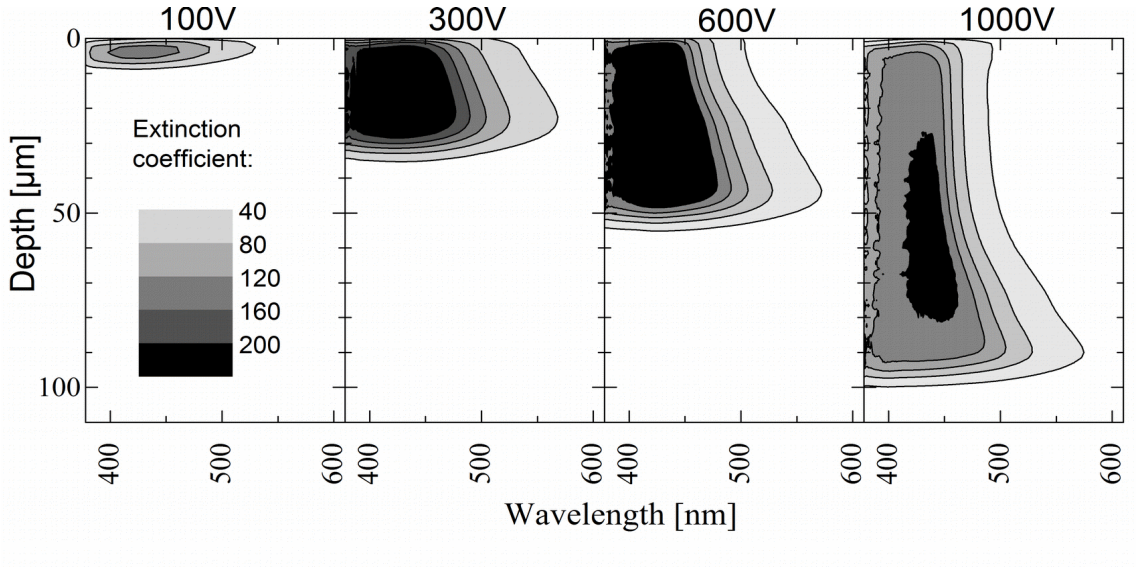

Fig. 3.12: Spectral profiles measured on the thin slices made from samples exchanged with different voltages, which are shown in fig. 3.11. Darker contours show higher extinction. Shown are extinction coefficients [1/mm].

the thin slice of the 100V exchanged sample. Also the thin slice thickness obtained from fitting of the sum of spectra is very low. This results from the decrease of the measured extinction due to straylight. The spectral profiles are shown in fig. 3.12. The graphs show the extinction coefficients in mm^{-1}, which were derived from measurements of light transmitted through the thin slices and the obtained thicknesses. For the 100V sample a thickness of 30µm was assumed to correct for the error by straylight.

3.2. Simulation of nanoparticle absorption

The Maxwell Garnett theory described in section 1.6.3 has been used to fit plasmon bands to all measured spectra. For the dielectric function of the silver nanoparticles the size-dependent Drude model was used. Over this the particle radius is introduced as a fitting parameter. Another fitting parameter is the filling factor. Not included in this model is a shift of the plasmon band due to the spill-out effect [57]. This small shift could not be determined since the peaks of the plasmon bands are cut off.

Figure 3.13 shows examples of spectra measured on a thin slice and for the obtained fits. Measured extinctions of more than 5.8 were ignored since the corresponding weak signal gets distorted by straylight, sensor noise and sensor temperature changes. Often an extinction below that was measured on the short wavelength flank of the plasmon bands. The light intensity of the used halogen lamp is very low in this wavelength region though, therefore this could be an effect of the measuring setup. Fitted plasmon bands show a different angle in this wavelength region, making the accuracy of this part of the spectrum doubtful.

The fitting parameters obtained for the series with different annealing times are shown in the graphs in fig. 3.14. The filling factors are plotted in the left graph and the particle radii in the right graph, both as a function of the position where the spectra were measured. For large parts of the thin slices it was not possible to find reliable values since the peaks of the plasmon bands were not measured. Plasmon bands with very different heights and therefore widths can be fitted to this, which corresponds to

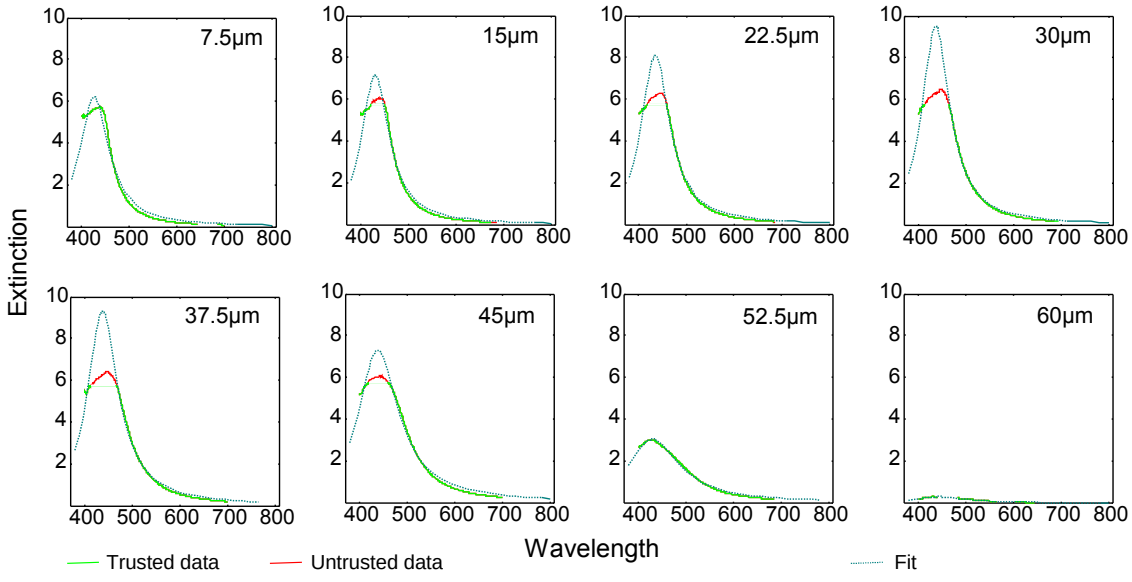

Fig. 3.13: Example fits for profiles measured on the 600V exchanged sample. Every 5th fit is shown.

different filling factors and particle sizes. These values have been removed from the graphs shown, so only the values from the deepest particle-containing layers with lower concentration are plotted.

Also the obtained filling factor values at the glass surface have been plotted to show the actual surface position and the maximal slope measurable with the microscope spectrophotometer. For the filling factor profiles the slope measured at the glass surface (depth=0) is also shown in fig. 3.14a. The ideal result would be a vertical line; however the slope is 0.02%/µm. This results from straylight going through the microscope beside the sample. Since these effects are comparable all over the thin slice, 0.02%/µm represents about the maximum slope that can be measured. This slope is only reached for the 1h profile for $x \leq 78\mu m$, where the filling factor is 0.06% and higher.

Interestingly the slopes for different durations have similar shapes, they only get shifted with longer annealing times. For a standard diffusion process the concentration profile

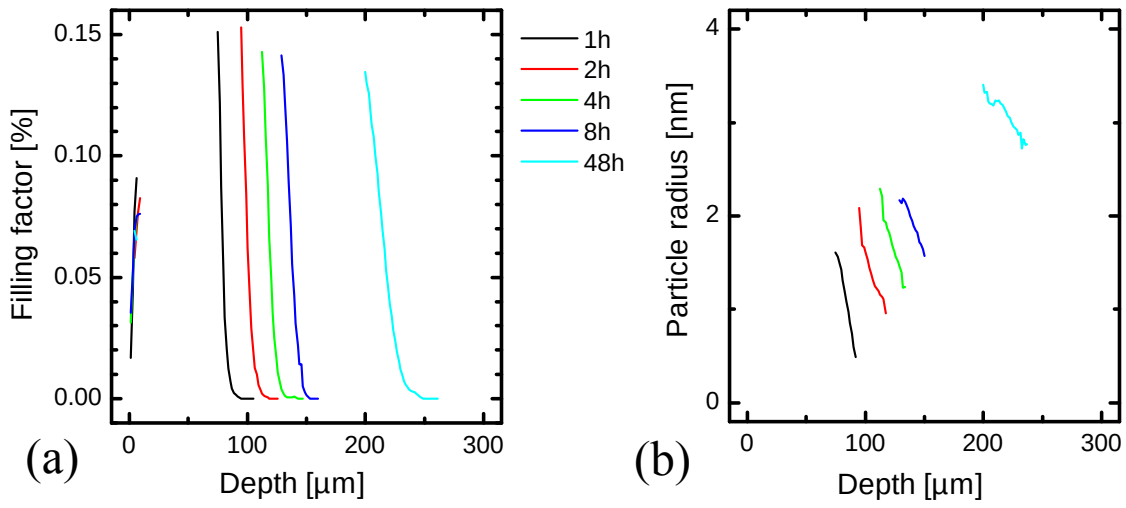

Fig. 3.14: Fitting parameters for the plasmon band profiles measured on the thin slices (solid lines). The filling factor profiles are shown in (a) and the particle radii in (b), both as a function of the depth in the glass. Only the low-concentration end is shown since the concentration was too high in most of the sample to determine it reliably.

would become more flat with longer diffusion times.

The thickness of the nanoparticle-containing layers l_L of the whole uncut sample has been determined from the filling factor profiles. Usually the width would be measured at half of the maximum filling factor, or at a fraction of 1/e. Since the maximum value is unknown an arbitrary value had to be chosen, so all thicknesses were obtained at $f = 0.05\%$. There the thicknesses are: 76µm after 1h, 97µm after 2h, 115µm after 4h, 135µm after 8h and 214µm after 48h. As can also be seen in fig. 3.14a the edge of the filling factor profile is shifting by about the same value for each doubling of the annealing time. This corresponds to a nearly logarithmic growth of the layer thickness. To this a function has been fitted:

$$l_L = 70.8\mu\text{m} + 35.5\mu\text{m} \ln t \tag{3.2}$$

where t is the annealing time in hours.

The particle radii graphs show a decreasing particle size with decreasing filling factor. This effect can also be seen in the spectra shown in fig. 3.8 as a broadening of the plasmon band at the edge of the particle-containing layer. For short diffusion times the spectra show very broad plasmon bands at the edge, equivalent to very small particle radii. For longer diffusion times the plasmon band becomes much more narrow in this depth, which corresponds to a particle radius growing over time. This growth is caused by the well-known Ostwald ripening [101]. For longer annealing times the spectra show more narrow plasmon bands at the edge, equivalent to larger particle radii in areas with similar filling factor. This results from the longer annealing time and lower growth speed of the layer thickness.

Similar spectral fits were also done for the profiles of the samples exchanged with

different voltages. The fitting parameters are plotted in fig. 3.15. Regions where the peak of the plasmon band was cut off are not shown since the fits were ambiguous.

The filling factor curves again show similar slopes for the different voltages. For the 100V exchanged sample filling factors were found for the whole particle-containing layer since the highest measured extinctions were quite low. However this is due to the limitation of the measurable extinction due to straylight from above and below the range with nanoparticles. Due to the small thickness of the particle-containing layer this straylight limits the extinction for the whole range. The peak of the plasmon band is flattened, resulting in a broader plasmon band with less height. This also changes the particle radius fitting parameter for the 100V exchanged sample. For the other samples the particle diameters were fitted properly for the edge of the slice again. The sizes at the edge of the layer are similar for all exchange voltages, while thicker slices created with longer annealing times are showing larger nanoparticles in the depth.

Again the thicknesses l_L of the particle-containing layer were determined from the spectral fits. The layer thickness with a filling factor of 0.05% or more is 9µm for the

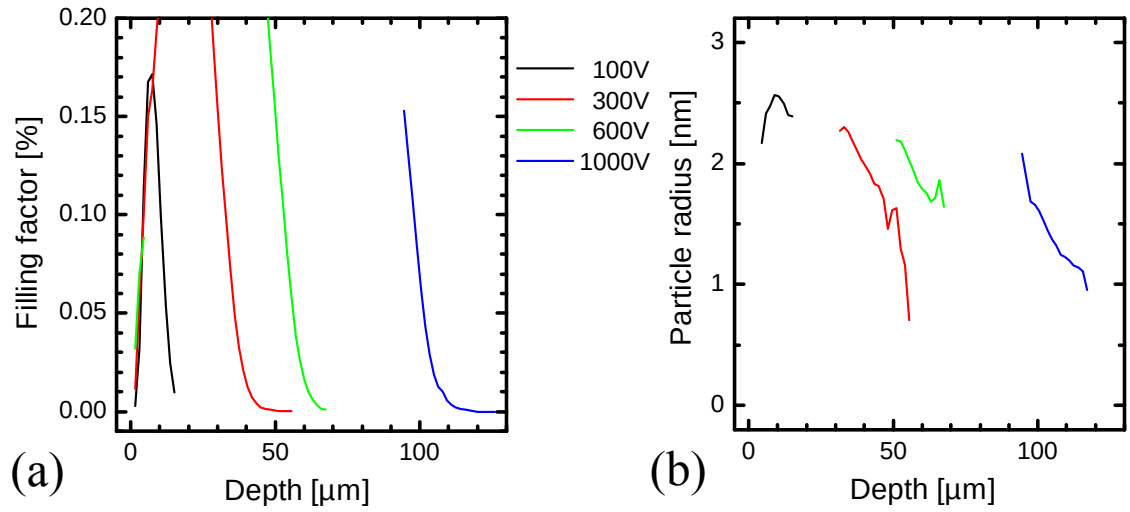

Fig. 3.15: Fitted filling factors (a) and particle radii (b) for cross section profiles of samples produced with different exchange voltage.

100V exchanged sample, 31µm for 300V, 52µm for 600V and 97µm for 1000V. To this a linear function can be fitted, which describes the dependence of the layer thickness l_L on the exchange voltage U:

$$l_L = 0.095\,U \tag{3.3}$$

Before annealing the thickness of the silver ion-containing layer had been measured in SEM images, which was shown in fig. 2.10. This shows an increase of the layer thickness proportional to the charge transfer during ion exchange. This is a stronger than linear increase because the charge transfer is increased for higher voltages by the stronger current increase during the process, while the initial current is proportional to the applied voltage. The increase of the layer thickness during the annealing process happens due to diffusion. The diffusion increases the layer thickness at a speed that is not increasing proportionally with layer thickness, it would be independent of the thickness for very large thicknesses. This compensates the larger than proportionally increasing initial thickness, resulting in the linear relationship here. That it is linear here might be a random coincidence.

When looking at the spectral profiles for different annealing times, which were shown in fig. 3.8b, it stands out that the plasmon bands are quite narrow in a layer of 40µm to 50µm thickness. The plasmon band width shows nearly no change over the depth of this layer, while in deeper layers plasmon bands are wider. The width in the surface layer decreases with increasing annealing time.

Plasmon band widths are smallest for particle diameters of about 5nm. Larger and smaller nanoparticles show wider plasmon bands. For 1h annealing time the plasmon bands are very wide in a depth of about 70nm. Berger [51] observed a similar

broadening in deeper layers for a glass exchanged from a salt melt, and then annealed in air. He attributes this to the growth of very large particles.

In the profiles for longer annealing time the initially very broad plasmon bands in a depth of 70µm are decreasing over time. This can not be explained with large particles. It would mean that particles sizes increase rapidly first, and then decrease again. Therefore the broad plasmon bands must be caused by very small nanoparticles with a diameter of 1 to 2 nm. These are growing over time, resulting in more narrow plasmon bands. In Berger's work the broad plasmon bands were observed after 3 to 4 days annealing time, therefore it is obviously a different effect.

The thickness of the surface layer is quite close to that of the ion exchanged layer before annealing, which was 46µm (see fig. 2.10). Spectral profiles for different voltages were shown in fig. 3.12. For 600V the thickness of the silver ion containing layer after ion exchange was 16µm. The spectral profile after annealing also shows a layer with narrow plasmon bands with a thickness of about the same size. For lower 300V and 100V the thicknesses of the ion exchanged layers were 8.7 and 2.7 µm, which is too thin to see a clear effect in the spectral profiles.

In large areas of the spectral profiles of the cross sections, especially in the initially ion exchanged layer the peak height of the plasmon bands could not be measured. But conclusions can still be drawn about the filling factor from the measured base of the plasmon band. A large change in filling factor would also change the base of the plasmon band, increasing the overall absorption and respectively making the measured plasmon band wider. The plasmon band in the initially exchanged area becomes more narrow with longer annealing times. This corresponds to average particle sizes growing

over time due to Ostwald ripening. If there is a growth of the filling factor it is not showing in this part of the plasmon band, and can therefore only be small. The reduction of silver and agglomeration to nanoparticles in this area must occur on a time scale which is short compared to the used annealing times.

3.3. Simulation of silver diffusion during annealing

The growth of the particle-containing layer during annealing is the result of the diffusion of silver, either in ionic or atomic form. Hence the filling factor profiles show similarities to diffusion profiles obtained for silver ion diffusion in glass [72]. Each profile shows a gradual decrease of the filling factor with the depth, and the slopes become more flat for longer annealing times, similar to diffusion processes in general.

The particle formation is a rather complex process, not only consisting of diffusion processes but also of reduction and agglomeration processes. For a first evaluation of the occurring processes only the diffusion is simulated with the rather simple Fick's second law, which was also given in eq. 2.2. Here the concentration is replaced with the filling factor:

$$\frac{\partial f}{\partial t} = D\frac{\partial^2 f}{\partial x^2} \tag{3.4}$$

This is neglecting any change in concentration of the diffusing silver by the agglomeration in nanoparticles or differences in the behaviour of atomic and ionic silver.

To simulate diffusion process, this equation is discretised using the finite difference method. The diffusion equation is often used as an introductory example in lectures on finite difference methods. Filling factors are calculated for discrete values of x and t.

Values of x are indexed with an i and the distance between subsequent values is always Δx. For t values the index is n and the distance is also constant at Δt. Filling factor values in certain coordinates are indicated by the indices of these coordinates, in the form $f_{i,n}$.

Replacing the time deviation by a forward difference quotient and the second deviation with respect to x by a central difference quotient results in:

$$\frac{f_{i,n+1} - f_{i,n}}{\Delta t} = D \frac{f_{i-1,n} - 2f_{i,n} + f_{i+1,n}}{(\Delta x)^2} \tag{3.5}$$

By rearranging and combining Δt, $(\Delta x)^2$ and D to R this can be transformed into the explicit representation:

$$f_{i,n+1} = R(f_{i-1,n} - 2f_{i,n} + f_{i+1,n}) + f_{i,n} \tag{3.6}$$

In the explicit representation the condition R<0.5 must be fulfilled to preserve stability of the method. This can require that smaller time steps are chosen. The advantage of the explicit difference method is that it uses only simple arithmetic without equation systems or integrals, which makes simulations simple and fast for the same resolution.

Eq. 3.6 was used for a one-dimensional numerical simulation of the development of the silver concentration profile during annealing. The starting profile of the diffusion is the silver concentration profile of the glass directly after ion exchange. In chapter 2 it was presented how this has been obtained from a backscattering electron microscopy image of the ion-exchanged glass, which showed a well-confined homogeneous silver layer of 46µm just below the surface.

The concentration of silver in this layer has been determined by EDX to be about 15 atom-%. This has to be converted to the volume concentration since we want to

simulate the filling factor. From the known composition of the B270 glass its molar density can be calculated, which is 0.041 mol/cm^3. This means that the silver concentration was 0.0061 mol/cm^3. The nanoparticles are assumed to have a density comparable to macromolecular silver, which has a molar density of 0.0972 mol/cm^3. From the latter two values results in a volume filling factor of 6.3%.

The whole thickness of the glass of 1mm was simulated, with a resolution of $\Delta x = 0.15\mu m$. The time step size Δt was 0.02s, and the simulation was initialized with a step profile with 6.3% Ag in the first 46µm.

The diffusion coefficient D is not known. It has been fitted by running a diffusion simulation with an initial value, and by finding the time where the sum of the squares of the difference of the simulated filling factor profile and the profile obtained from spectral fits for a diffusion time of 1h is minimal. Multiplying the initial D value with the diffusion time gives the fitting diffusion coefficient. The obtained value for this diffusion at 550°C is:

$$D = 0.098\mu m^2 / s \tag{3.7}$$

With this value the diffusion was also simulated for longer durations. The resulting profiles and the filling factor profiles are shown in fig 3.16. The filling factor profiles are shown as solid lines, the diffusion simulation results as dotted lines.

The position in the depth of the glass matches quite well for the profiles simulated for 1, 2 and 4h diffusion time. However for longer annealing times the simulation shows a distinctly deeper diffusion than the particle filling factor profiles. The trend is different: When comparing the filling factor profiles for 1,2, 4 and 8h it catches one's eye that the

distance from one profile to the next continuously becomes smaller. For the diffusion simulation for the same durations the distance from one profile to the next is increasing on the other hand. Profiles from diffusion simulation and filling factor profiles both become flatter for longer diffusion times. But the simulated profile for 1h annealing is more flat than the measured profile for that diffusion time. A steeper profile can be simulated by assuming a much larger initial filling factor, the best fit is achieved for an impossibly high filling factor of 4000%. So there are processes that are leading to a steeper profile of the silver nanoparticle concentration than what would result from a simple diffusion process.

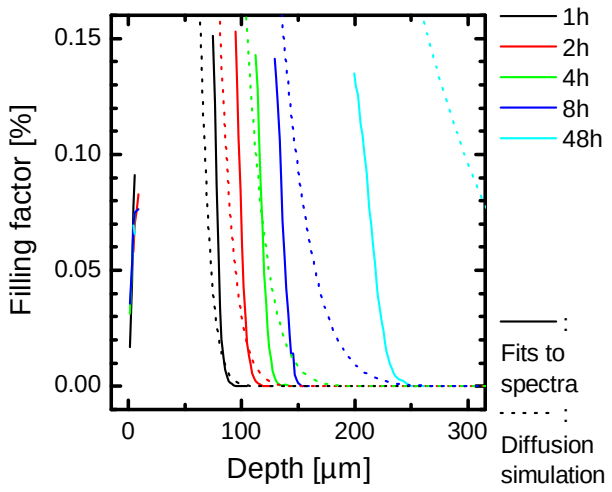

Fig. 3.16: Comparison of diffusion simulation results (dotted lines) to filling factor profiles obtained from fits to transmission spectra measured on a thin slice (solid lines).

One process that could lead to this increased steepness of the actual profile and the slowing down of the actual diffusion compared to the simulated is the gradual agglomeration of silver, since that is reducing the amount of silver that is taking part in diffusion. If that effect is stronger for low silver concentrations than for higher concentrations, for example due to a reducing agent that is quickly consumed completely, it would slow down the diffusion only while the concentration is low. The diffusion in the area with higher concentration would not be affected, so the profile would become more steep at the edge.

Another very likely cause for the increased steepness is the mixed alkali effect, which can be explained by the formation of percolated pathways for the major diffusing species by the rearrangement of the glass matrix [73, 88] (also see section 2.1.3). Silver ions have a larger ionic radius than sodium ions. Therefore the glass matrix is rearranging after a few silver ions diffused into a specific glass volume to give space for the larger silver ions. Once a certain concentration is reached percolated pathways for the diffusion of silver are forming, which greatly increase the diffusion speed of silver. This will result in a steeper concentration gradient, and in a slowing down of diffusion when concentrations are low. This would result in a slowing down of diffusion for long diffusion times, where concentrations become lower.

3.4. Discussion of reduction mechanisms

In the field of nanoparticle generation in glass the reduction of silver ions is mostly explained by the reaction with iron ions present in the glass in the form:

$$\begin{aligned} Fe^{2+} &\rightarrow Fe^{3+} + e^{-} \\ Ag^{+} + e^{-} &\rightarrow Ag^{0} \end{aligned} \tag{3.8}$$

Glasses with increased iron content show a strong formation of silver nanoparticles [102]. The presence of even low concentrations of iron in a glass results in a slightly green colour due to the absorption of iron ions. It can often be seen easily by looking through a sheet of glass from the side. This absorption is unwanted in optical applications, hence optical glasses like B270 are made with a very low iron content. B270 does not show any colour when looking through a piece from the side. Therefore reduction by iron can not explain silver nanoparticle formation in B270.

Ma et al [70] found by XPS analysis of glass treated by field-assisted silver ion-

exchange that a small amount of Ag^{2+} is present. They concluded that the following reduction reaction may take place:

$$Ag^{+} + Ag^{+} \rightarrow Ag^{2+} + Ag^{0} \tag{3.9}$$

A great source for explanations of reduction mechanisms for silver in glass lies in publications about research on waveguide fabrication in glass by silver ion exchange [73]. In this field reduction is an unwanted process because the forming nanoparticles are causing losses in the waveguides. In many studies ways were explored to eliminate reduction, resulting in the finding of several causes for silver reduction.

In these works it was found that not only Fe ions, but also arsenic and antimony can cause the reduction of silver. These elements all reside in the glass matrix as polyvalent ions, and exist in different states of ionisation. By changing glass compositions it was also found that silver ion reduction is related to the presence of non-bridging oxygen in the glass matrix [103]. By adding large amounts of Al_2O_3 to the glass composition the formation of non-bridging oxygen atoms can be prevented. The Al atoms are replacing Si atoms in the glass matrix, also with bonds to four oxygen atoms. Aluminium has a valence of 3, while the valence of Si is 4. Therefore a negative charge is located at each Al atom, which compensates the positive charge of an alkali ion in the same way as a non-bridging oxygen. Fig. 3.17 shows how the addition of K_2O leads to the formation of non-bridging oxygen in (1), and how adding similar amounts of K_2O and Al_2O_3 prevents the formation of non-bridging oxygen in (2). Also (1) shows how two alkali ions and two non-bridging oxygens normally occur together.

During this work a very interesting observation has been made when a piece of B270 glass, which was exchanged in a salt melt by Codixx, was annealed at 550°C. It did not

form any nanoparticles.

Since B270 contains nearly no impurities and because the glass processing in an electric field is required it can be concluded that the electrons for silver reduction are extracted from atoms that are intrinsic to the glass, namely the non-bridging oxygen atoms which had already been identified as a possible reducing mechanism by Araujo [103]. The following reactions are considered for this reduction reaction [104, 105]:

$$2(\equiv Si - O^{-} Ag^{+}) \rightleftharpoons \equiv Si - O - Si \equiv + O^{-} + (Ag_2)^{+} \tag{3.10}$$

$$2O^{-} + 2Ag^{+} \rightleftharpoons 2Ag^{0} + O_2 \tag{3.11}$$

Another reaction that can produce atomic silver is by formation of Ag^{2+} and Ag^{0} from two Ag^{+} (3.9). This and also reaction 3.10 might require the presence of $(Ag^{+})_2$ dimers. These dimers are equivalent to both alkali ions in the structure shown in fig. 3.17 (1) to be replaced by Ag^{+}.

Because the ionic radius of Ag^{+} is larger than the radius of Na^{+} this would require a

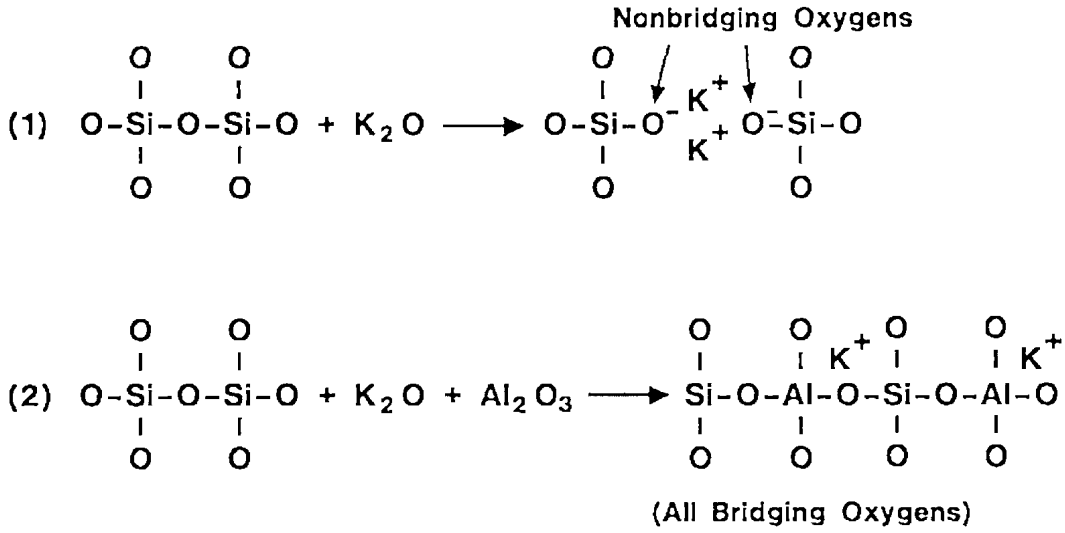

Fig. 3.17: (1): Formation of non-bridging oxygen in a glass matrix by addition of K_2O. (2) Addition of equal amounts of K_2O and Al_2O_3 prevents the formation of non-bridging oxygen. From [103].

larger rearrangement of the glass matrix. The energy provided by the electric field during ion exchange might induce strong local changes, and might induce the formation of percolation pathways for silver ions, which will result in locally increased silver concentrations. This will also result in the formation of $(Ag^+)_2$ dimers, which are needed for this reduction reaction.

Codixx produces nanoparticle-containing glasses by making glasses that were ion-exchanged in a salt melt and then annealing them in a hydrogen atmosphere. This causes a very quick reduction, which results in the agglomeration of the atomic silver in large particles with a diameter of about 30nm in a layer with a thickness of a few µm [106]. This behaviour is different to that of our samples presented in section 3.1.1. We do not observe the formation of such large nanoparticles, particles with a diameter over 10nm would have been visible in SEM. Also the approximately constant nanoparticle concentration in layer thicknesses much larger than the initially ion exchanged layer shows that the silver is diffusing over a long time. Since atomic silver agglomerates quickly the silver must be diffusing in ionic form. The reduction reaction must take place not only in the initial ion exchanged layer, but also in deeper layers when silver diffuses there during annealing.

The $(Ag^+)_2$ dimer concentration should be proportional to the square of the fraction of Na+ sites occupied by Ag+. Since the Ag+ concentration is decreasing during the annealing due to diffusion the number of dimer sites would decrease quite strongly over time. This can not explain the nearly constant amount of reduction per glass volume.

Another explanation would be a slightly different reduction reaction that occurs on sites where single alkali ions have been removed by the electric field. The negative charge of

the associated non-bridging oxygen also would have been removed since local charge neutrality is required. With a second alkali ion-NBO complex this would result in a complex of the form

$$\equiv Si - O^- Ag^+ + \equiv Si - O^0 \tag{3.12}$$

The neutral non-bridging oxygen would tend to find a binding partner because it lacks a valence electron for a full shell. It can not bind to the charged non-bridging oxygen since its outer electron shell is full, and the sodium ion does not tend to be neutralised by the excess electron. Though when a silver ion replaces the remaining sodium ion it could enable the following reaction:

$$\equiv Si - O^- Ag^+ + \equiv Si - O^0 \leftrightarrow \equiv Si - O - O - Si \equiv + Ag^0 \tag{3.13}$$

Silver ions have a much higher tendency to accept an electron and to be neutralised than sodium ions. The structure is called a peroxy linkage, which is a diamagnetic defect in silicate glasses [42].

What was concluded from the spectral analysis of the sample cross sections is that the reduction in the ion-exchanged layer happens on a short time scale, and then is not relevant any more. When silver ions are diffusing into deeper layers that were not ion exchanged a comparable amount of silver gets reduced. These two observations are pointing to an effect that is limiting the amount of silver reduced in a given volume. The analysis of samples exchanged with different applied voltages does not show a clear dependence of particle filling factor on voltages, rather the results are also pointing to a roughly constant peak filling factor.

The model of reduction linked to $(Ag^+)_2$ dimers can explain the observed spectra if a

process is limiting the reduction rate in a given glass volume. For example the number of sites suitable for dimer formation could be limited. For the model of reduction at dimer sites which are depleted of one ion a strong dependence on the applied voltage would be expected. This should show more clearly in the cross sections of samples exchanged with different voltages, making this explanation unlikely. The reduction at $(Ag^+)_2$ dimer sites is the most probable explanation. This could be tested in further experiments, testing for example the dependence of peak filling factors on exchange temperature, exchange duration or annealing temperature. Also the presence of $(Ag^+)_2$ dimers and their disappearance due to reduction reactions could be identified by photoluminescence [107].

3.5. Summary and conclusions

Annealing of the ion exchanged B270 glass at 550°C induced the formation of silver nanoparticles in the ion exchanged layer. Very interesting results were found by optical analysis of these glasses, especially on thin slices of cross sections of these.

Transmission spectroscopy shows that the produced glasses have a quite strong absorption due to the plasmon band of the nanoparticles. Thin slices of cross sections showed that the nanoparticle-containing layers are very homogeneous. Transmission spectra of these slices were measured in different positions which correspond to different depths in the original samples. The absorption due to surface plasmon oscillations of the nanoparticles was simulated with the Maxwell Garnett theory. Fitting the simulations to the measured spectra allowed to find particle filling factors and particle sizes.

A series with different annealing times allowed to analyse the development of the particle-containing layer over time and to derive filling factor profiles. These were compared to a diffusion simulation, which simulates the formation of the particle layer from freely diffusing silver. In principle this simulation agreed with the experimental results, but it also showed interesting differences. The experimental results show in a steeper profile, with the steepness changing only minimally with diffusion times. Diffusion simulation shows a concentration profile that becomes considerably more flat over time. Also diffusion depths for longer annealing are smaller compared to the simulation. This shows that there is a slowing-down effect at the edge of the silver-containing layer, compared to the diffusion within the layer. This is explained by the formation of percolated pathways.

A second series of experiments was performed with varying exchange voltages. This allows to greatly vary the thickness of particle containing layers. Interestingly there was no indication of a variation of nanoparticle concentrations within the layers for different voltages. This effect narrows down the potential reduction mechanisms. In B270 reduction must be related to non-bridging oxygen, because it is a high purity glass free of other reducing agents. Reduction must be limited to certain sites in the glass, possibly anion dimer sites which are occupied by two silver ions.

Several results presented in this chapter were published. The first publication was on the analysis of the first thin slice made of a cross section of a glass with silver nanoparticles made with field assisted ion exchange. The second publication was on the series with different annealing times.

4. Pulsed laser irradiation of silver-ion-doped glass

When silver ion exchanged glass was irradiated with a nanosecond pulsed laser it showed an interesting metallic shine. When this was first observed it seemed as if the observed reflection might originate from cracks and other damages of the glass surface, though further analysis showed something very interesting. A metallic-looking film had formed at the surface of the silver ion doped glass. This has never been noticed before, and it was surprising that ionic silver from the glass is reduced to metallic form in such a large amount. Imaging with a scanning electron microscope showed that the surface film is not a solid metallic film, but consists of a single layer of silver nanoparticles with a size above 100nm. This chapter is aimed at the characterisation of this newly discovered material. During this work several results presented in this chapter were published in two publications [108, 109]. A patent was filed on the manufacturing process for this new material [110].

This glass-silver composite (GSC) is formed by pulsed laser irradiation of the silver ion exchanged glass, which was presented in chapter 2. It is characterised by optical microscopy, optical spectroscopy and scanning electron microscopy. These methods were described in section 1.5.

The chapter starts with an introduction of the laser irradiation method and a characterisation of the lasers in section 4.1. It is followed by the experimental results in section 4.2, which start with an analysis of single lines written with different laser parameters, and continues with optical spectroscopy of squares written line by line. This is followed by a simulation of laser heating, which gives an idea of the temperatures

during the process. The final section discusses the mechanisms of the formation of the GSC.

4.1. Experimental methods

The GSC is manufactured by laser irradiation of silver ion exchanged glass. The methods of ion exchange were presented in chapter 2.

Laser irradiation is done with two different laser systems. Both lasers operate at a wavelength of 355nm, but offer different pulse lengths. The first laser system is a Laservall Violino UV laser, which delivers 10000 to 80000 pulses per second with a pulse length of 10 ns. The second system is a Coherent Talisker laser. It delivers laser radiation of 1064, 532 and 355 nm, of which the last one was used for irradiation of ion exchanged glass. Its pulse length is 10 ps, the repetition rate can be from 200kHz down to single pulse mode.

Each laser system is equipped with a galvanic scanhead for positioning of the laser beam. These are equipped with a flat field scanning lens system, meaning that the laser beam is focussed in the same plane for all (x,y) beam positions. The scanhead can be equipped with different lenses. The experiments were done with a lens with a focal length of 160 mm.

4.1.1. Laser beam profiling

The intensity profile of an ideal Gaussian laser beam in three dimensions is:

$$I(x,y,z)=I_0\left(\frac{d_0}{d(z)}\right)^2\exp\left(\frac{-8(x^2+y^2)}{d^2(z)}\right) \tag{4.1}$$

where z is the propagation direction of the beam and the x-y-plane is perpendicular to it. The coordinates are chosen so that the centre of the beam waist is at $(x,y,z) = (0,0,0)$. d_0 is the beam diameter at the waist of the beam. It measures the diameter of the area where the intensity is large than e^{-2} of the peak intensity. I_0 the peak intensity which occurs in the centre of the beam waist. $d(z)$ is the beam diameter at position z:

$$d(z) = d_0 \sqrt{1 + \left(\frac{z}{z_R}\right)^2} \tag{4.2}$$

The Rayleigh range z_R is a measure for the focussing properties of the laser beam. In large distances from the waist the beam diameter grows linearly with the distance z. There the full divergence angle of the laser beam is:

$$\Theta = \frac{d_0}{z_R} \tag{4.3}$$

For the TEM_{00} mode of a laser with wavelength λ the divergence angle is:

$$\Theta = \frac{4\lambda}{\pi d_0} \tag{4.4}$$

If higher oscillation modes are contributing to the beam both the divergence angle and the beam waist diameter are increased by the factor M compared to the TEM_{00} mode. From this the beam quality factor M^2 can be calculated:

$$M^2 = \frac{\pi d_0 \Theta}{4\lambda} \tag{4.5}$$

The laser beams were characterised with a beam profiler. This was with a lensless digital black and white camera which is connected to a computer. It is controlled by a program that I have written in C++ during this work. The camera is placed in the laser beam in the x-y-plane at a certain z position and records an image. With all image processing functions turned off the grey value of each pixel is proportional to the laser

intensity in that spot. A two-dimensional Gaussian fit is made for the obtained image, giving the diameter of the laser beam in x and y direction. From multiple beam diameters at different z positions the whole three-dimensional beam profiles can be obtained. The pixel size of the camera is $6 \times 6\ \mu m^2$. This is quite large compared to the analysed beam diameters. To allow correct measurements of such small beam diameters the fitting formula was adapted by integrating the intensity over the area of the pixels, which is defined by the length of the pixel sides l_P:

$$I(x,y) = I_0 \int_x^{x+l_P} \int_y^{y+l_P} \exp\left[-8\left(\left(\frac{x'-x_0}{d_x}\right)^2 + \left(\frac{y'-y_0}{d_y}\right)^2\right)\right] dy'\,dx' \tag{4.6}$$

(x,y) is the coordinate of the lower left corner of the pixel, while (x_0, y_0) is the coordinate of the centre of the laser beam. Doing the integration gives the used fitting function:

$$I(x,y) = I_0 \frac{\pi d_x d_y}{32} \left[\mathrm{Erf}\left(\frac{\sqrt{8}(x'-x_0)}{d_x}\right)\right]_x^{x+l_P} \left[\mathrm{Erf}\left(\frac{\sqrt{8}(y'-y_0)}{d_y}\right)\right]_y^{y+l_P} \tag{4.7}$$

This allows to make accurate fits for beam diameters on the order of the pixel size. Fitting parameters are d_x, d_y, x_0, y_0, I_0 and an added constant background intensity.

4.1.2. The Laservall Violino UV laser system

The Violino laser system is a complete industrial-style system with an integrated scanhead. For safety it is mounted in an enclosure with a safety switch that prevents laser operation when the enclosure is opened. The focus distance is adjusted by a translation stage, which moves the whole laser resonator and scanhead in the z direction.

This is a diode-pumped pulsed Nd:YAG laser system running internally at 1064 nm.

After the laser resonator two nonlinear conversion crystals generate light of 355 nm, the first one doubling the frequency to a wavelength of 532nm and the second one generating 355 nm from the 532nm. It produces a Gaussian laser beam with a beam quality factor of M^2 = 1.1. The laser system also has output windows for the 532nm and 1064nm radiation, these were not used for the experiments presented in this thesis.

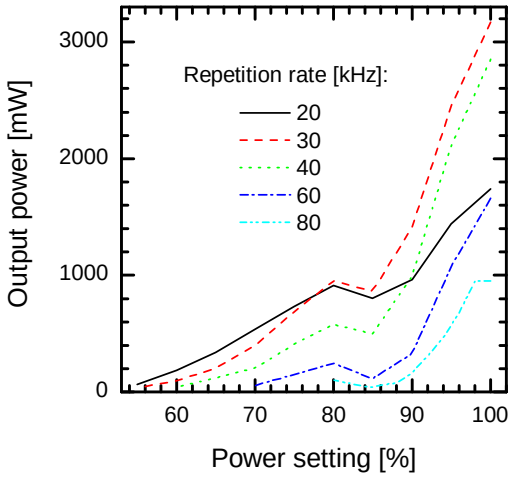

Fig. 4.1: Output power of the Violino laser system as a function of power setting for different repetition rates.

The output power is set as a percentage value, which sets the driving current of the pumping diodes. This is not linearly related to the actual output power because of the threshold current of the pumping diodes, the laser threshold of the Nd:YAG resonator and the nonlinearity of the frequency conversion. Therefore the output power was measured with a power meter for different settings. The measured values are shown in fig. 4.1. The output power also depends on the repetition rate at which the laser is running.

The beam profile of the Violino laser has been characterised by placing the camera under the laser and changing its z position. A grey filter has been added to reduce power, whereby it was taken care to place the filter under an angle to avoid back reflection into the laser. The measured beam profile is shown in fig. 4.2. The beam profile is elliptical in certain depths, with the axes of the ellipsoid slightly different than

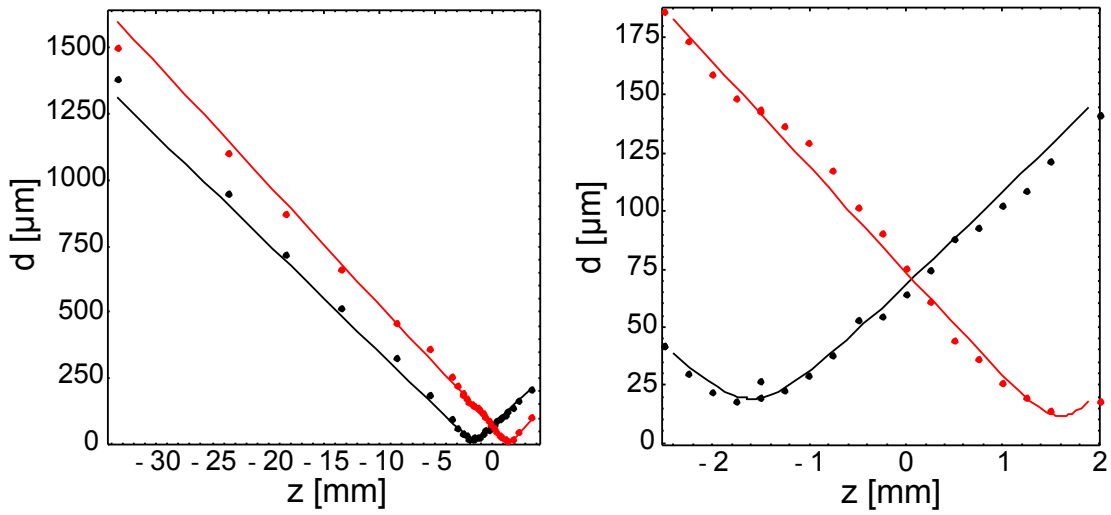

Fig. 4.2: Beam profile of the Violino laser system. For each z position a Gaussian profile was fit. Beam diameters in x direction are shown as black dots, diameters in y direction as red dots. Solid lines are fitted beam profiles. Left: overview of the whole measured range. Right: Area around the focal point.

the x and y translation directions. The camera rotation has been aligned with the ellipsoid axes.

The measured beam profile shows that the focus in x and y direction is in different z positions. This results in elliptical spots, for example at z = -1.75 mm the beam diameter is 18 µm in x direction and 149 µm in y direction. Near z = 0 the beam is circular with a diameter of about 65 µm. The fitting parameters for the three-dimensional beam profile are given in table 3.

Table 3: Beam profile fitting parameters for the Violino laser

	z_0 [mm]	d_0 [µm]	Θ [°]
x	-1.59	19.2	2.4
y	1.60	11.6	2.6

4.1.3. The Talisker laser setup

The Talisker laser system is a tabletop picosecond laser system designed for industrial use. It consists of a small modelocked fibre seed laser which produces low-energy ultrashort pulses at 1064 nm. Seed pulses are selected through a Pockels cell and coupled into the diode-pumped amplifier. There they are circulating for several passes and get amplified in the gain medium until the ejection Pockels cell opens. The amplifier is optimised to run at a repetition rate of 200 000 pulses per second. An acousto-optic modulator (AOM) after the amplifier acts as a pulse picker, which allows to change the repetition rate or to select single pulses. The output power of the amplifier can be controlled by a motorised waveplate and the AOM. The waveplate allows to greatly reduce the power throughout the whole experiment, while the AOM can change the output power quickly for individual pulses.

The amplifier is followed by a harmonics compartment, which contains two lithium triborate (LBO) crystals for frequency conversion. The compartment has exit windows for three different wavelengths, specifically the unconverted 1064 nm, frequency-doubled 532 nm and frequency-tripled 355 nm. For the irradiation of ion exchanged glass only the 355 nm is used.

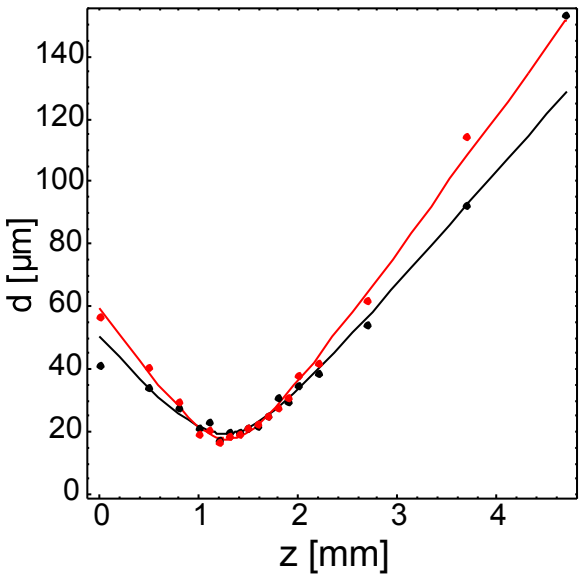

Fig. 4.3: Beam profile of the Talisker laser after focussing by the scanhead. This shows the beam diameter in x direction in black and y direction in red, as a function of the focal position.

The laser system is situated on an optical table, and the laser light is guided by several mirrors to a galvanic scanhead for beam positioning. A beam expander increases the diameter of the laser beam before the scanhead to allow optimal focussing.

The output power of the laser can be controlled by setting the waveplate position at the laser controller, and by controlling the AOM over an analogous input of the laser system. This input is connected to an analogous output of the scanhead controller. This allows to change the laser power by the software provided with the scanheads. This software contains a calibration table.

The amplifier is always running at a repetition rate of 200kHz and at full power. This ensures a very high reproducibility and constance of the output power, undisturbed by temperature changes in the resonator or amplifier. The power setting of the AOM controls the pulse energy, therefore the scanhead software is calibrated on pulse energy values and not directly on the output power.

The beam profile of the Talisker laser has been characterised under the scanhead, using the f = 160mm lens that is also used for irradiations. The laser power was fully attenuated by the waveplate, and reduced further by the AOM. The profile of the beam around the focus is shown in fig. 4.3. Fitting parameters are shown in table 4.

Table 4: Fitting parameters for the Talisker laser.

	z_0 [mm]	d_0 [µm]	Θ [°]
x	1.26	19.4	2.1
y	1.28	17.7	2.5

4.1.4. Surface profiling

The surface profiles of GSCs were measured with a Dektak 3 surface profiler. This mechanically measures surface profiles along a single line by moving a stylus with a diamond tip over the analysed surface. The vertical resolution in the used measuring range of 655 kÅ (65.5 µm) is 10 Å (1 nm). The diamond tip has a radius of 2.5µm.

4.2. Experimental results

Laser irradiation experiments were done with B270 glass ion-exchanged at 300°C with an applied voltage of 1000V for 1h. This type of ion-exchanged glass was also thoroughly analysed in chapter 3 with a series of different annealing times. It has a silver ion-exchanged layer with a thickness of 46µm.

First an experiment done with the Violino laser is presented. This is a ns-pulsed laser with a wavelength of 355nm. It has a Gaussian laser beam, and irradiation was done in focus where the spot diameter d is 65µm. The laser beam was scanning over the glass with a scanning speed v_s of 14mm/s. This resulted in linear modifications of the silver ion doped layer, and multiple lines were joined to form a square, with a line distance of 60µm. The laser repetition rate f_{rr} was 80kHz. The density of pulses during irradiation of lines is characterised by the number of pulses per spot N_p:

$$N_p = \frac{d\, f_{rr}}{v_s} \tag{4.8}$$

which is 340 here. The first experiment was done with a pulse energy of E_p = 12µJ, which is equivalent to an averaged laser power of 950mW, and a fluence of F = 420mJ/cm^2. The fluence is given by

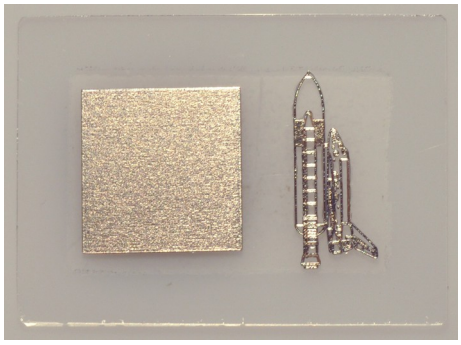

Fig. 4.4: Silver -glass composite (GSC) fabricated by laser irradiation of ion-exchanged glass. The square is written line by line with a pulse energy of 12 µJ. The area of the square is 144 mm². The drawing is written with the same parameters.

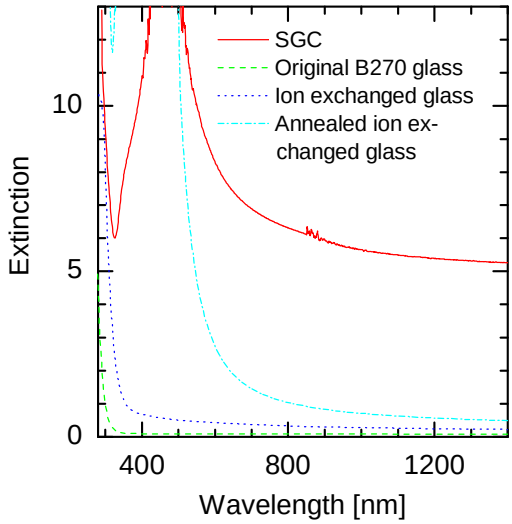

Fig. 4.5: Extinction spectra measuring the transmitted light. The surface plasmon resonance of silver nanoparticles causes an absorption band around 470 nm. Annealing the silver ion exchanged glass results in the formation of silver nanoparticles with a plasmon band centred at 405 nm, as shown in chapter 3. The original glass (before ion-exchange) only shows absorbance for less than 300 nm, while the ion exchanged glass has a considerable absorption at 355 nm.

$$F = \frac{E_p}{A} = \frac{4\,E_p}{\pi\,d^2} \tag{4.9}$$

where A is the cross section area of the laser beam, which can be calculated from the beam diameter d.

Fig. 4.4 presents an image of the fabricated GSC material. It shows a large square which is used for optical and electron-microscopical characterisation of the modification, and a drawing to show the capability for linear modifications. Fig. 4.5 shows the extinction spectrum of the modified square, displaying an SPR band as the red line. The peak

absorption is at about 450nm, assuming that the cut-off part is symmetrical. The graph also shows in cyan for comparison the extinction of an ion-exchanged glass prepared under the same conditions, which was annealed at 500°C for 2h to form nanoparticles in the glass volume. Compared to this the GSC shows a redshifted absorption band and a broadband extinction of about 5.2 over the whole measured spectral range. This is equivalent to a transmission of 0.6%. The blue line shows the extinction of the ion-exchanged glass, This shows an absorption of about 65% at the laser wavelength. The green line shows the extinction of the original B270 glass.

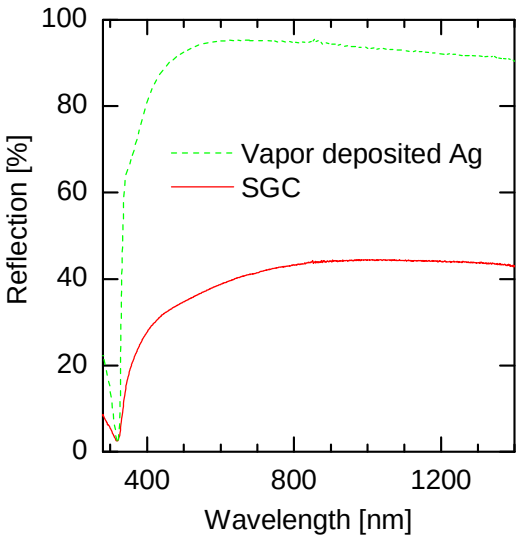

Fig. 4.6: Reflection of GSC (red) and of an evaporated silver film for comparison (blue).

Also the reflection of the square was measured with the Jasco spectrometer, using the integrating sphere. In this way total reflected light integrated over the whole hemisphere is measured, including both specular and scattered reflection. Reference measurement is done with a standard white sample, which is reflecting nearly ideally homogeneously to all directions. The result of this measurement are shown in fig. 4.6. The reflectance of the GSC is shown in red. The graph also shows for comparison in blue the integrated reflectivity of an evaporated silver film on glass. The GSC reflectivity reaches values up to 45%, while the plain, compact silver film is showing a reflectivity above 90%. Both have a deep drop centred at 320nm, which is characteristic for the reflection of silver.

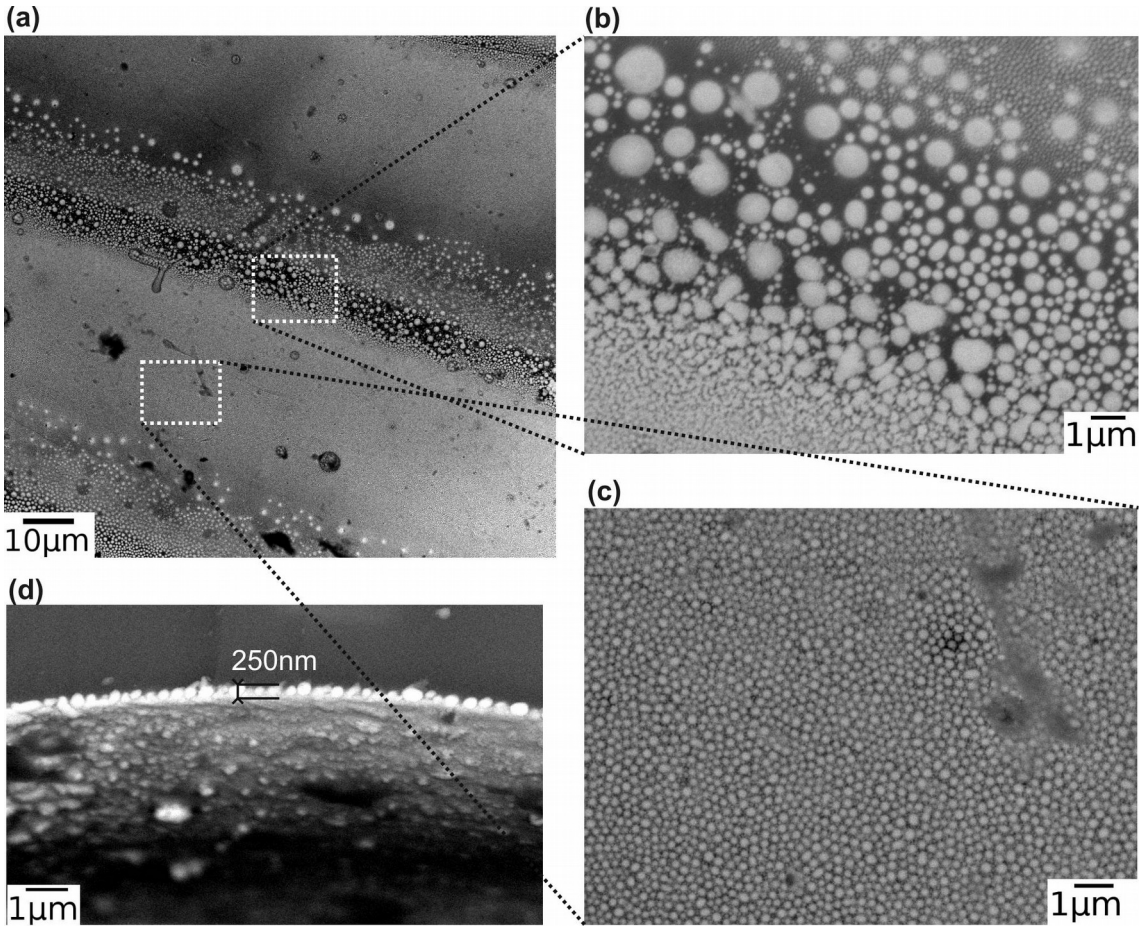

Fig. 4.7: Electron microscopy images of the GSC, taken in backscattering mode. Brighter pixels mean heavier elements, in this case silver. ***a****: Top view of the surface. The laser-written line is shown as a large brighter area going down from left to right under an angle of 20°.* ***c*** *shows an image zoomed into the centre of a line,* ***b*** *to the border.* ***d*** *is a view of the cross section of a written line, showing the thickness of the surface layer of about 250nm.*

The laser-written square has been analysed with a scanning electron microscope operating in backscattering mode. In this mode heavier elements such as silver show as brighter areas. The images are shown in fig. 4.7, starting with an overview in (a). It shows the laser-written lines going in an angle of 20°, with the top line written first. The centre of the lines shows as nearly homogeneous bright area at this magnification, while the large nanoparticles become visible at the border. A zoomed-in image of the centre of

the line, which is shown in (c), shows silver nanoparticles with a diameter of 200 to 300nm in a quite regular pattern with only small size variations. The zoomed in image of the border shown in (b) shows particles with differing sizes with a diameter of up to 1.4µm. The large particles are not in a regular pattern. In (d) an image of the cross section of the centre of a line is shown. It shows that the nanoparticles are located in a dense monolayer with a thickness of about 250nm, which is similar to the particle diameter.

4.2.1. Laser-written lines and their properties

Following these first experiments single lines were analysed in more detail. This allows the properties of single lines to be analysed without the effect of line overlapping. Lines were written with different pulse energies, and with 8 ns pulses from the Violino laser and 10ps pulses from the Talisker. Other laser parameters are identical to the first experiment shown above. The line experiments are done in preparation for writing squares with different pulse energies, which are presented in section 4.2.2. Squares are then irradiated with identical parameters.

Often a laser modification requires a certain threshold fluence F_{th}. Then only the sample area is modified where the laser fluence at the surface is equal or larger to F_{th} This is the case for processes directly related to the laser intensity, such as colour centre generation, photoionisation and other photochemical processes. Heating processes can only be described by a threshold fluence if lateral heat conduction is negligible.

For a Gaussian beam profile the square of the width d of the beam where the threshold fluence is achieved is given by [111-113]

$$d^2 = 8w_0^2 \ln\left(\frac{F_0}{F_{th}}\right) \tag{4.10}$$

F_0 is the peak fluence, which is $8/\pi$ times the laser fluence. w_0 the radius at which the fluence decreases to F_0/e^2. So a semi-logarithmic plot of the squared diameter of the modified area d^2 versus fluence F will produce a straight line if the modification is limited by a threshold fluence. The line intercepts the F axis at the threshold fluence, and the beam radius can be determined from the slope.

For pulsed laser irradiation the fluence is normally given by dividing the pulse energy by the laser cross section area.

Lines were written with both lasers with different fluences. Lines written with ps pulses are shown in fig. 4.8. The pulse energies in μJ are written as numbers between the images. Also an irradiation was done with a lower pulse energy of 2μJ, not resulting in any modification. Image (a) was taken in reflection mode, which shows the reflection of the surface. By contrast the image taken in transmission mode (b) also shows particles created in the volume, while the reflecting areas of the surface result in darkening. For ns-pulsed irradiation the pulse energies were, in μJ: 2.4, 2.9, 3.3, 4.0, 5.5, 6.5, 7.5, 10.0 and 12.0.

Noticeable in the pictures of ps-irradiated lines is surface roughening that occurs for pulse energies of 8μJ and more. This is accompanied by the formation of bubbles in the glass, which are visible in the transmission mode image. For ns irradiation this effect occurs for 6.5μJ and more.

Modified widths were measured in both transmission and reflection mode images on lines written with ps and ns pulses. In transmission mode the total modified width was

measured, including the area with colour change due to nanoparticle formation in the glass volume. In reflection mode only the width with a changed surface structure was considered. The changes are attributed to melting of the glass. Squares of the measured line widths are plotted as a function of fluence on a logarithmic scale in fig. 4.9.

Linear functions have been fit to the measured widths, which are also shown in the plot. From these threshold fluences and beam

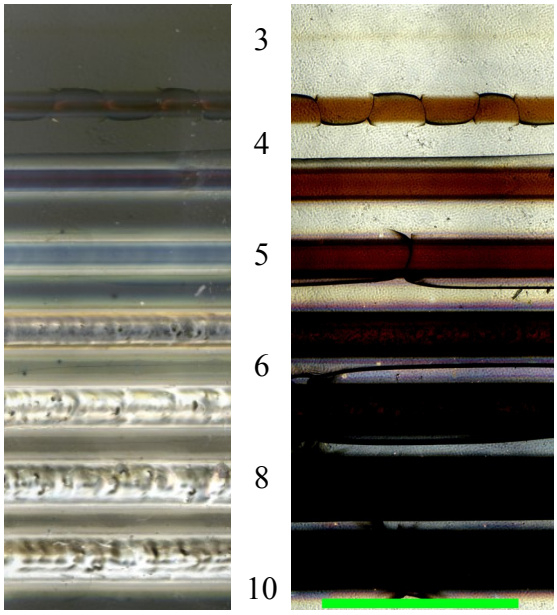

(a) *(b)*

Fig. 4.8:Microscope images of lines written with ps pulses. Pulse energies in µJ are written as numbers between the images. Images are taken in reflection mode (a) and in transmission mode (b). The reflection image shows mainly surface modifications, while the transmission image also shows modifications in the volume. The green scale bar in the bottom right is 1mm; the distance between the centre of lines is 200µm.

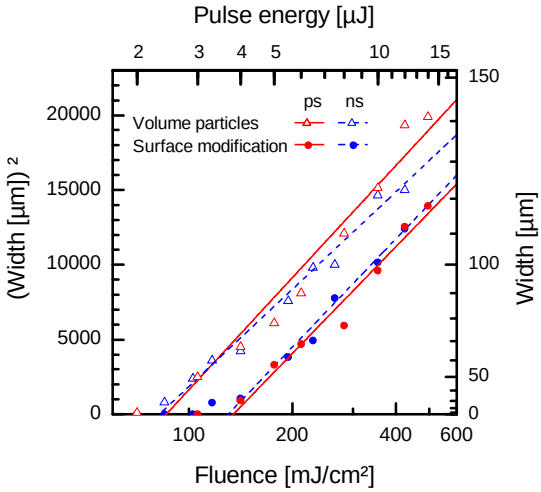

Fig. 4.9: Widths squared of laser induced modification versus fluence on a logarithmic scale for ps pulses (red) and ns pulses (blue). Top axis shows laser pulse energies for comparison, right axis the actual non-squared width values. The width of the area with particles in the volume (triangles) has been measured by transmission microscopy. Similarly the width of the area with surface modification (filled circles) was measured by reflection microscopy. Linear fits shown as red and blue lines are giving the threshold fluence as fluence axis intercept.

radii were determined:

Table 5: Threshold fluences for line modifications and fitted beam radii.

	Threshold fluence [mJ/cm^2]	Fitted beam radius [µm]
ps pulses, volume	85.8 ± 5.3	73.5 ± 2.9
ps pulses, surface	134.5 ± 6.7	71.8 ± 2.8
ns pulses, volume	81.9 ± 3.6	68.5 ± 1.8
ns pulses, surface	130.0 ± 4.8	72.3 ± 2.3

Interestingly the modification widths are nearly similar for ps and ns pulses, as are the fitted functions. The obtained beam radii are more than twice as large as the actual beam radii. This indicates that the assumption made in this calculation that modifications are determined by a threshold fluence does not apply here. There is a different mechanism which determines the modification width, presumably the achieved temperature. This is not only determined by local laser fluence, but also by heat diffusion. We are analysing this further down in this paper. The function is still a quite good fit to the experimental data and is therefore good for comparing ps and ns pulses, and also the obtained threshold fluences are valid.

4.2.1.1. Electron microscopical analysis

The microscopic structure of the single lines written before the squares was also analysed with an SEM device working in electron backscattering mode. Silver-containing areas are shown as bright areas in the obtained images.

Fig. 4.10 shows SEM images of the line written with the ps laser with a pulse energy of

12µJ. The left image shows an overview of the whole width of the laser-written line. The laser beam was scanning over the glass from top to bottom. Silver at the surface shows up in backscattering SEM images as bright areas due to its higher atomic mass compared to the glass constituents. The centre of the line is generally slightly darker than the border, with some considerably darker areas. Higher magnifications of this centre region show nanoparticles of nearly similar sizes and distances in all brighter regions, and smaller particles with smaller distances in dark areas. Such brightness variations were not observed in the square written with 12µJ 8ns pulses, but it is also present in the single lines written with ns pulses. The origin of this different behaviour is not clear.

The border of the line shows several interesting features, which are shown in more detail in the right image. There is a region with very large spherical particles in the centre of the image. Right of that region, towards the centre of the line, particles are

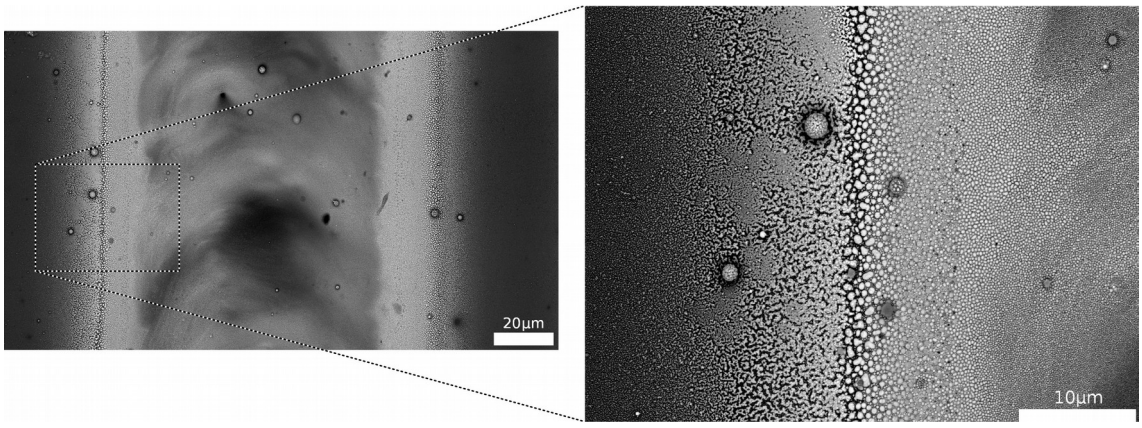

Fig. 4.10: Electron microscopy images of a line written with the ps laser with a pulse energy of 12,14µJ. ***Left****: overview of the line, which was written by a laser beam scanning from top to bottom. The laser had a Gaussian profile with highest power in the centre, and decreasing power to the sides. Bright areas are indicating the higher atomic mass of silver at the surface.* ***Right****: magnified image of the border region. The structure changes from unaffected glass on the left to a structure comparable to that in the centre of the line on the right of the image.*

getting smaller. To the left the silver forms non-spherical agglomerations. Similar changes in structure are reported by Peng for laser sintering of silver nanoparticles [114], and are attributed to the onset of melting. The smaller particles just right of the region in image centre are irregular in size and distances. Some particles also show up only very dim, some with dark cores. This could be either particles consisting of a lighter material, or leftovers of ablated silver particles. In the right third of the right image the structure changes to equidistant particles of locally similar sizes, larger first than in the centre of the line, but arranged in a similar structure. At the right edge of the right image the structure becomes considerably darker. There is a narrow region with very large nanoparticles with low concentration where melting starts. This is not present in that form on the right side of the laser-written line. Also the left half of the small-particle region is slightly darker than the right half. Both effects are attributed to a slight non-circularity of the laser profile resulting from the used optical setup.

The particles in the centre of the laser-written lines were analysed in more detail. Therefore images were taken of the centre of each line. The dark areas with smaller particles were avoided, only the bright regions of each line were chosen.

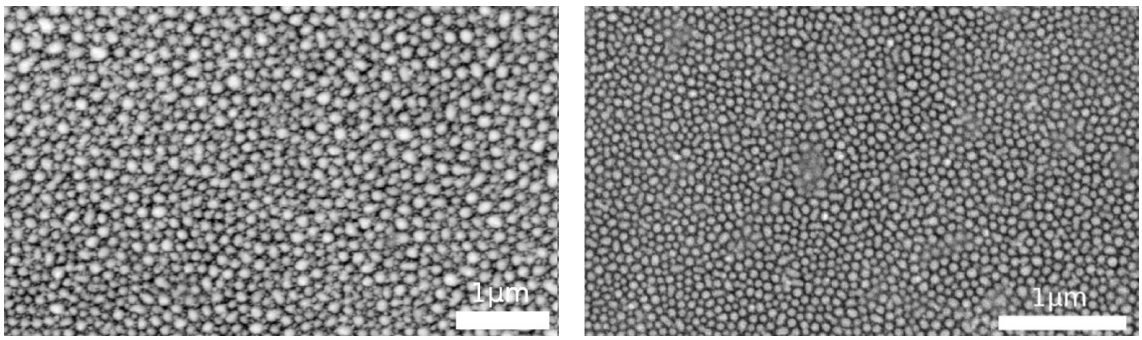

*Fig. 4.11: Highly magnified image of the centre of lines where laser fluence is highest. These were both written with a pulse energy of 12µJ, with ps pulses in the **left** and ns pulses in the **right** image. Particles have a diameter of about 100nm for ps irradiation and 60nm for ns irradiation, with only small variations in particle sizes and distances.*

Fig. 4.11 shows images from the centre of the line written with 12µJ. The image on the left is written with ps pulses, while the one on the right is of the line written with ns pulses. Mostly particles have similar sizes in each image.

Similar images were taken from the centre of all laser-written lines. The image analysing software ImageJ [115] was used to determine particle diameters and distances for different laser parameters. Distances were measured between particle centres. The individual sets of sizes and distances for each image were following Gaussian distributions. Parameters of these distributions were determined by a fitting algorithm, giving the mean value and the standard deviation. Due to the method of of this calculation method extreme values have not much effect on the determined distribution. This was done since there were a view very large particles detected due to dirt, and small particles due to noise, which are both ignored due to this method.

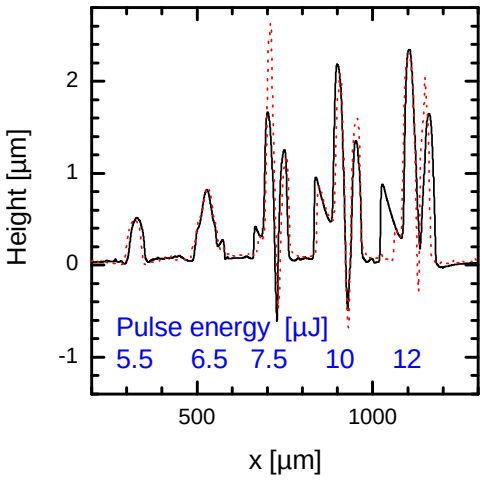

Fig. 4.12: Surface profiles of lines written with ns pulses, with pulse energies given in blue. The profiles show bulging, and a dent in the centre of the line for high pulse energies.

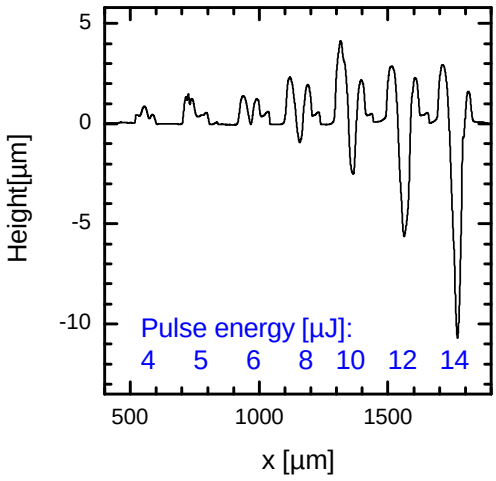

Fig. 4.13: Surface profiles of lines written with ps pulses. The bulging of the glass starts at lower pulse energies than for ns irradiation, and the dents are deeper.

The particle sizes and positions determined by this are plotted in fig. 4.14. The mean values are plotted as data points, and the standard deviation of size and distance distributions as error bars. The data shows a strong correlation between particle distances and sizes, the distances are always only slightly larger than the sizes. With decreasing pulse energy the measurements become smaller. The ns irradiation produces considerably smaller particles than the ps irradiation.

Microscope imaging already showed the formation of bubbles within the material. In some cases the cross sections prepared for SEM imaging were broken through one of the bubbles, allowing to see its inside. One of these bubbles is shown in fig. 4.15. Interestingly the inner surface of it shows silver nanoparticles similar to the ones formed at the surface.

4.2.1.2. Surface profiling of laser-written lines

The surface structure of laser-written lines was analysed with the Dektak 3 ST surface

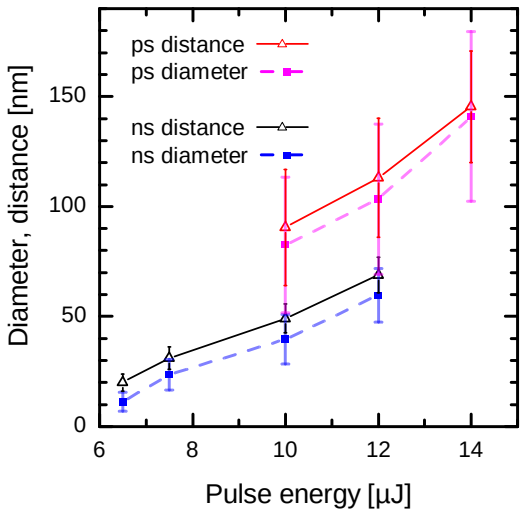

Fig. 4.14: Plot of particle diameters and distances (from centre to centre) determined for different laser parameters.

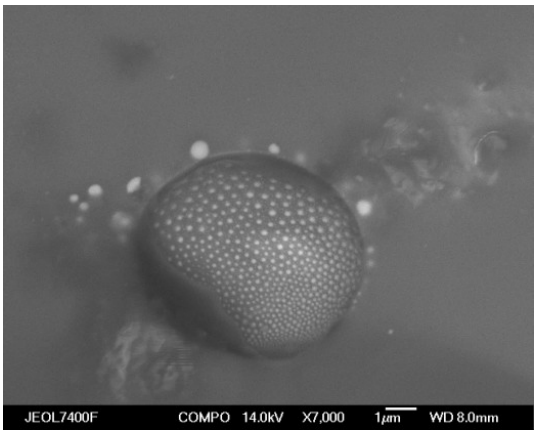

Fig. 4.15: A bubble that formed in the glass below the metallised surface.

profiler. This shows any changes in height of the surface, allowing to see the effects of volume increase and ablation. All lines written with ns pulses were analysed in one scan, and so were all lines written with ps pulses.

The scan of the ns-pulsed written lines are shown in fig. 4.12. It shows the profile of the five lines written with highest pulse energies, with the pulse energy written in the graph in blue. Lower pulse energies did not induce any measurable surface profile change. For 5.5 and 6.5μJ the volume a bulging of the glass surface is measured. For higher pulse energies also a dent is measured in the centre of the line. The black line shows a scan done from lowest to highest pulse energy line. The red line shows a scan taken in the opposite direction by rotating the sample. It is not taken at the same sample position, because it is not trivial to position the stylus that accurately. There are a few differences between the two measurement runs, but most features are identical. The differences can result from a slightly different sample structure at the changed measurement position. This shows that the surface profiler is giving reproducible results, and that the results are not distorted by jumping or bending of the stylus, or other direction-dependent effects.

Fig. 4.13 shows the profile of the lines written with ps pulses. Here a bulging is measured already at a lower pulse energy of 4μJ. The heights of bulging are slightly higher. There are also dents in the centre of the lines, which are much deeper than for ns-pulsed irradiation.

The profiles were analysed to evaluate the bulging of the surface and the formation of dents in the line centres. Fig. 4.16 shows the minimum and maximum position of each line profile. This shows only a small difference between peak heights of lines written by

ps and ns irradiation. The minimum value, which mostly represents the dents, is similar for pulse energies up to 8µJ. For higher pulse energies the dents become considerably stronger for ps-pulsed irradiation, while this is not the case for ns-pulsed irradiation.

Fig. 4.17 shows the difference in area between the measured cross section of each line and a straight line connecting both ends of the measured range. This represents the volume change due to irradiation effects. For ns irradiation this shows a volume increasing nearly linearly with pulse energy. ps-pulsed irradiation shows a stronger volume increase for up to 10µJ, and a strong volume decrease for 12 and 14µJ.

The observed volume increase can be attributed to gas bubbles trapped inside the glass, and partly also to cracks that formed in irradiated areas. The dent in the centre of lines can be caused by ablation, but also by a redistribution of molten material from the centre to the sides of the written lines. For ps-pulsed irradiation with 12 and 14µJ a clear volume decrease is observed, which clearly indicates ablation. For other irradiation parameters it is not certain if material redistribution is the dominating effect, or if the

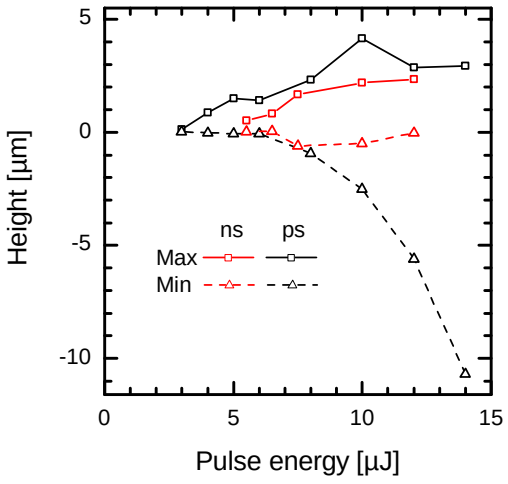

Fig. 4.16: Minimum and maximum level of the profile of each laser-written line.

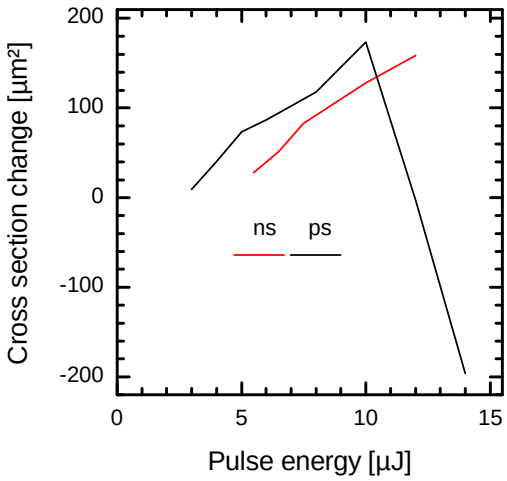

Fig. 4.17: Change of cross section area for lines written with ps and ns pulses with different energies.

observed profiles result from a combination of volume increase and ablation.

4.2.2. Laser-written squares

After writing lines squares have been written with the same fluences and laser parameters as the lines for measuring optical transmission spectra. They were written by filling the square homogeneously with parallel lines. The line distance, which is the scan pitch during irradiation, had to be varied for different fluences since the modification width varies strongly. A constant line distance would either result in unmodified spaces between the lines for low fluences or multiply overlapping lines for high fluences. Therefore the line distance was always set to 90% of the surface modification width measured for single lines written with the same fluence. For fluences below 130mJ/cm^2 the line width was set to 90% of the volume modification width since no surface modification was observed for these fluences. Images of the produced squares are shown in fig. 4.18, the ps-pulsed irradiated areas in the left picture and the ns-irradiated areas in the centre and the right picture. These pictures were taken with a microscope working in reflection mode. The left two pictures were taken with a white background behind the sample. In this configuration images show both surface reflections and transmitted light. Nanoparticles inside the glass are visible as red colour, while the image also shows the metallic look resulting from the surface particles. The right image was taken with a black background, showing strongly the surface reflection. Image stitching was used to obtain an image of all irradiated areas.

The ps-irradiated areas show only volume particles for up to 4µJ. At 5µJ a reflective film formed, which reflects stronger for the squares written with higher pulse energies. At 6µJ the surface becomes rough in parts of the square, while the whole squares turn

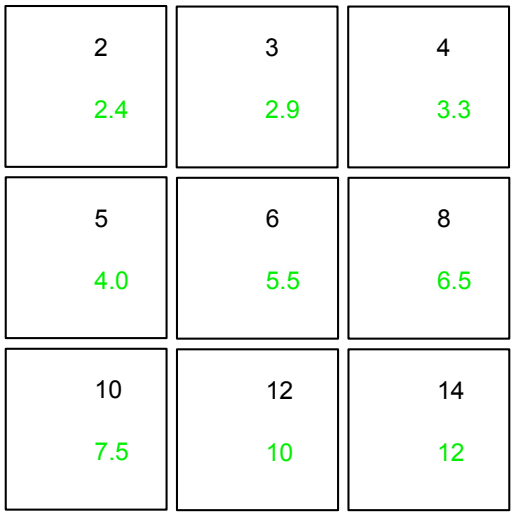

(a): *Pulse energies. top ps, bottom ns*

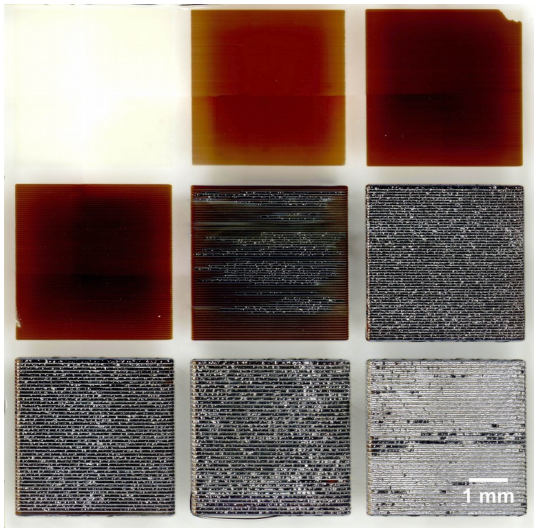

(b): *ps, white background*

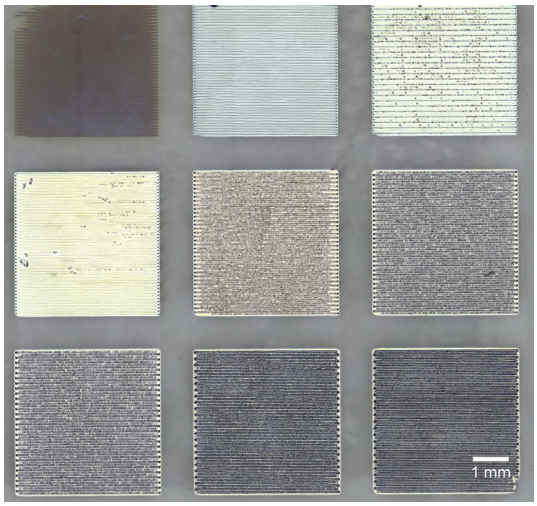

(c): *ns, black background*

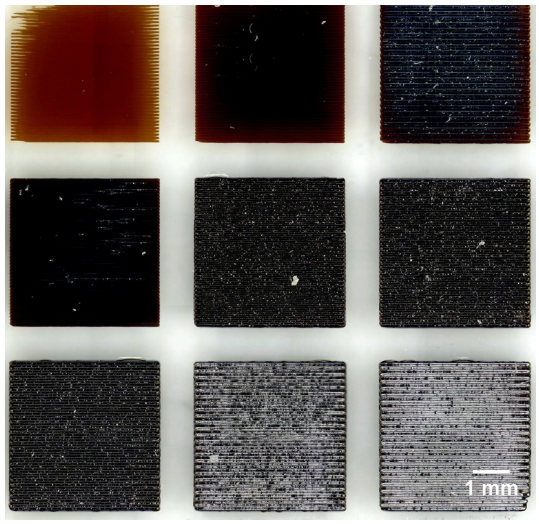

(d): *ns, white background*

Fig. 4.18: Images of laser-irradiated areas. ***(a):*** *pulse energies used in the individual squares shown in the photographs. Top (black) values in each square are for ps irradiation, the bottom (green) values for ns irradiation.* ***(b):*** *ps-irradiated squares. The image was taken with a microscope working in reflection mode, with a white background behind the glass.* ***(c):*** *ns-irradiated squares, taken with a black background.* ***(d)*** *shows the same glass as (c), but taken with a white background again.*

A white background reflects light back through the glass, adding transmitted light to the reflection image. Due to this the particles inside the class make squares in the right images more red, while image (c) is showing only the surface reflection.

rough for higher powers. This roughening coincides with the formation of bubbles inside the glass. The threshold of this process was found to be very sensitive to small fluence variations, which explains the inhomogeneity of the square written with 6µJ.

Optical transmission spectra measured on all squares are shown in fig. 4.19. Spectra are measured as extinction, which is the negative natural logarithm of transmission. Plots also show the extinction of the original, unirradiated but already ion-exchanged glass. At the laser wavelength of 355nm this shows an extinction of 1.07, equivalent to a transmission of 34.3%.

For low energies graphs are showing a distinct plasmon band, which is growing quickly with increasing pulse energy. At 4µJ a broadband extinction over the whole wavelength range occurs. This becomes stronger with increasing pulse energy. It is stronger for smaller wavelengths. Possible causes of the broadband extinction are the surface

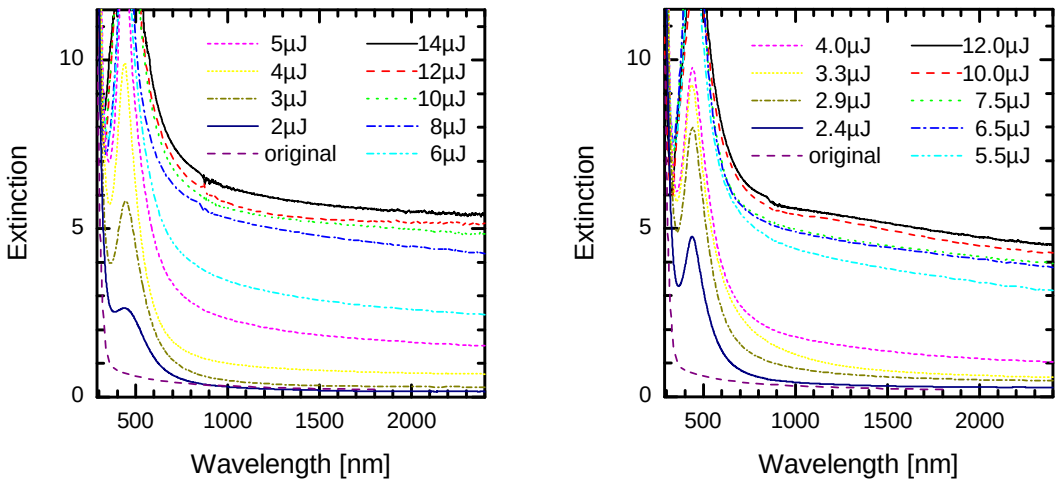

*Fig. 4.19: Extinction spectra areas irradiated with ps pulses on the **left**, and ns pulses on the **right**. There is a plasmon band showing for all irradiated squares which is centred at 440nm, which is typical for silver nanoparticles. There is also a nearly constant broadband extinction, which is measured for 4µJ and higher. It also becomes stronger with increasing pulse energy.*

reflection, surface roughness, straying at bubbles, and possibly also a broadband absorption effect caused by interacting nanoparticles at the surface.

To compare ps and ns-written spectra the extinction at the plasmon band peak and the extinction at 1700nm were determined, the latter being a measure for the broadband extinction. To find the height of plasmon bands which were cut off these were fitted with the plasmon band measured for the 4µJ ps-pulsed irradiation, multiplied with a fitting factor. This resulted in a very good fit, considerably better than what could be achieved with standard theories like Mie theory or Maxwell Garnett effective medium theory. The obtained plasmon band heights and broadband extinctions are shown in fig. 4.20.

Overall the obtained spectra are also very similar for both pulse lengths. For both the plasmon band height increases about linearly with pulse energies up to 6µJ, then increases slower. The broadband baseline also increases with pulse energies, showing a strong increase between 4 and 6µJ. Both are increasing at slightly lower energies for ns pulses. The differences are within the range of experimental errors.

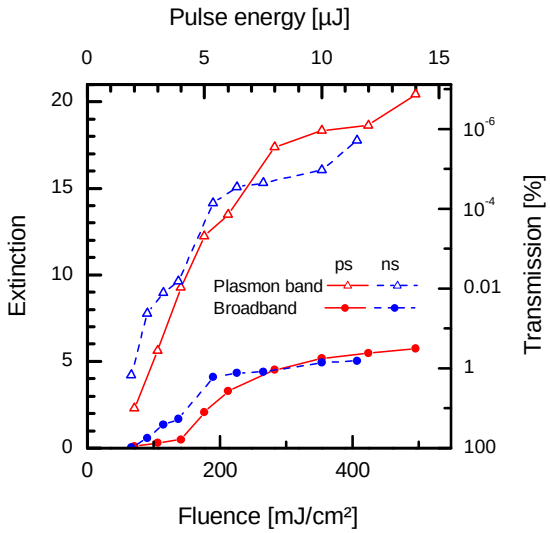

Fig. 4.20: Peak heights of the plasmon bands (triangles) and broadband extinction represented by the extinction value at 1700nm (filled circles). Values from ps irradiated squares are shown in red, from ns irradiated squares in blue with dashed lines. Top axis shows pulse energies for comparison, right axis the transmission equivalent of the given extinctions.

4.3. Simulating laser heating

An important effect of laser irradiation is the heating up of irradiated materials. Laser light is absorbed by the material, and the absorbed energy induces a local increase in temperature T. Several experimental observations can be related to heating. Particle formation observed in laser-irradiated glass has also been observed when the same glass was heated in a furnace to 550°C, as was shown in chapter 3. For 6µJ and more bubble formation has been observed in the glass. The release of gas from the glass requires a strong increase of mobility of the atoms of the gas, which results from the strong temperature increase. Also heating increases the speed and shifts the equilibrium of chemical reactions, which can be responsible for reduction of silver and formation of the gas trapped in bubbles.

With pulsed laser irradiation single pulses can induce large temperature changes in a small volume, which can result in melting and evaporation. If material is evaporated the absorbed heat is taken away from the rest of the material. Heat that does not leave due to evaporation stays in the material. From this local heated area the heat is diffusing into the material. This heat diffusion is described by the heat equation:

$$\frac{\partial T(x,y,z,t)}{\partial t} = \nabla [D \nabla T(x,y,z,t)] \tag{4.11}$$

D is the thermal diffusivity.

The heat from individual pulses is accumulated over time, resulting in further heating. In materials with strong heat conduction, for example metals, and if the heated volume is not too large, the heat accumulation can be neglected.

In subsections of this different approaches to heat simulation are shown. First the heat

diffusion length approach is presented, which allows the effect of laser heating to be quickly estimated. Next a Comsol model is used to analyse effects in more detail. Comsol is a very powerful program, which uses finite element methods (FEM) to simulate many different physical processes. Finally the heat equation is solved analytically for heating by short laser pulses. This allows the temperature change at single points to be quickly calculated, e.g. in the centre of the irradiated area where temperature is highest.

4.3.1. Material parameters

For any heating simulation the properties of the material must be known. Especially important are the absorption length for the used laser wavelength, the thermal conductivity, heat capacity and density of the irradiated material.

The material that was used in our experiments was silver ion-exchanged B270. Some properties of B270 can be found in the literature and in data sheets. The ion exchanged glass is expected to have slightly different properties, and these will also change when particle formation and the metallisation happen. In the simulations the values of unchanged B270 are used since no better values are known. Also it turned out in the end that the uncertainty regarding the absorption length is limiting the accuracy of the simulation. Though it still allows to draw some general conclusions.

Heating can induce phase changes, specifically melting and evaporation. Unlike other materials glasses do not melt at a single melting point temperature, instead they show the so-called glass transition. Their properties are changing gradually, without an actual phase change. Around the transition temperature the heat capacity is rising considerably,

a plot as a function of temperature shows a smooth step. But there is no enthalpy of fusion.

Important thermal characteristics of B270 glass are the glass transition temperature of 533°C and softening temperature of 708°C. A vaporisation temperature for B270 could not be found in the literature. For fused silica Schick [116] reports a vaporisation temperature of 2430°C, which is a reasonable first-order approximation. He also reports an evaporation heat of 335 kJ mol^{-1} and the decomposition of fused silica at 3000K. Decomposition can be linked to bubble formation due to the release of oxygen.

For a homogeneous material the absorption length can be derived from transmission measurements. From the transmission T the extinction a can be obtained. This is related to the extinction coefficient α by the Beer Lambert law, which was already given in equation 1.1. It can be written in the form:

$$a = -\ln T = \alpha l \tag{4.12}$$

where l is the layer thickness. If other processes than absorption can be neglected α becomes the absorption coefficient. The absorption length is given by α^{-1}.

Absorption in the ion-exchanged layer is induced by silver ions. They show an absorption band in glass centred at 240nm, which is caused by electrons being excited from 4f to 5s level. That band follows a Lorentz distribution. The area under the curve is proportional to the amount of silver ions in the glass. The centre of the absorption band lies within the glass absorption band, which is caused by oxygen ions. The glass absorption of B270 at 355nm is only small, inducing an extinction of 0.13 for a slice of one mm thickness. This extinction also includes reflection losses at the surface.

After ion exchange extinction at 355nm increases to 1.07 due to a homogeneous layer of silver ions. The layer thickness is approximately 40µm, and the extinction change due to absorption in this layer is 0.93, neglecting other possible effects such as increased straylight and reflection at the interface between ion exchanged layer and unaffected glass. From these values the absorption length of 43µm is obtained.

The absorption length is decreasing during the process. There are silver nanoparticles forming in the glass, which induce absorption due to the plasmon band. Due to this for irradiation with 3µJ ps pulses the extinction at 355nm increases to 4 after the process, which is equivalent to an absorption length of 10µm. Irradiation with 5µJ pulses results in an extinction of 7 at 355nm, or an absorption length of 5.7µm. To illustrate this effect the absorption length in different irradiated areas is shown around the laser wavelength in fig. 4.21. Also the temperature increase can have a broadening effect on the absorption band of the silver ions [117], the glass absorption [118] and the plasmon resonance band. For short laser pulses two photon absorption is an important process. It can already be an important process for pulses with a length in the ns range [119]. All these effects are further decreasing the absorption length.

The appearance of the resulting surface is metallic for sufficiently high pulse

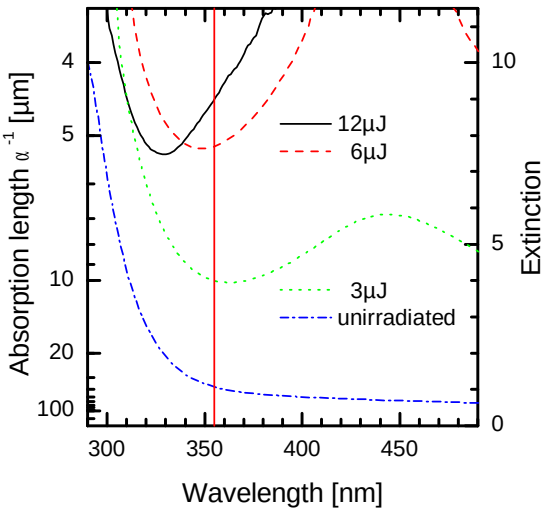

Fig. 4.21: Extinction spectra of unirradiated ion exchanged glass and irradiated areas around the laser wavelength. The absorption length has been derived from this and is shown on the left axis. The vertical red line marks the laser wavelength of 355nm.

energies. Metallic silver has an extremely short absorption length in the nm range. Therefore it must be assumed that the film of particles at the surface generated in the process also has an absorption length in the nm range. Though the transmission measurements on the final samples show that it does not absorb all light due to its low thickness. The reflectivity measured on modified areas was increased to 20%, though metals show a much lower reflectivity at high temperatures than at room temperature.

When squares are written lines are written with an overlap to produce a homogeneous area with surface particles. Nanoparticles were generated inside the glass at the border of the line written before, in an area with a width considerably larger than the line distance. These nanoparticles inside the glass decrease the absorption length from the beginning of the writing of the next line when squares are written. This effect does not occur in the single line experiments, therefore the effects when writing squares can be equal to the effects when writing lines with a slightly higher pulse energy. Such effects were observed for the limit of bubble formation by ps irradiation, and also the surface particle size of the square written first with 12µJ ns pulses are larger than for the single line written with the same parameters.

It can be concluded that the absorption length is 43µm for the unirradiated sample, but there are effects that can decrease it strongly during the irradiation process.

The other properties of B270 have to be taken from datasheets. Its density is 2.55 g/cm³. The thermal conductivity is given for different temperatures, in W/(m·K): 0.92 at 24.5°C, 1.01 at 89°C and 1.08 at 127°C. It is clearly temperature-dependent, though values for higher temperatures could not be found for B270. A publication by Helebrant [120] contains good approximations for a soda-lime glass for a wide temperature range.

In this work the laser heating of the glass by a CO_2 laser is simulated. This glass could be slightly different than B270, but the values given at lower temperatures are close to the B270 values. Also the transition temperature of 533°C that is used in this work is the same as that of B270.

The temperature dependence given for the heat conductivity is nearly linear. With the additional value of 2.1 W/(m·K) at 700°C taken from this work the following linear fit has been obtained:

$$k\left[\frac{\mathrm{W}}{\mathrm{m\,K}}\right] = 0.470 + 1.42 \cdot 10^{-3}\, T[\mathrm{K}] \tag{4.13}$$

Helebrant [120] also gives a formula for the estimation of the specific heat. There is a jump of the specific heat at the transition temperature by 122.2 J/(kg·K). The formula given in that publication can be simplified to:

$$c_p\left[\frac{\mathrm{J}}{\mathrm{kg \cdot K}}\right] = 1474 - \frac{3.46 \cdot 10^8}{(412 + T[\mathrm{K}])^2} + \begin{cases} 0 & for\ T \le 806\mathrm{K} \\ 122.2 & for\ T > 806\mathrm{K} \end{cases} \tag{4.14}$$

In the datasheet a heat capacity of 860 J kg^{-1} K^{-1} is given for heating B270 from 20°C to 100°C. Values given by Helebrant's formula are 778 J kg^{-1} K^{-1} at 20°C and 912 J kg^{-1} K^{-1} at 100°C. These values are in reasonable agreement. Therefore this formula is used to simulate the temperature dependence of the specific heat.

Heat conductivity k and specific heat c_p are often combined to the diffusivity D:

$$D = \frac{k}{\rho\, c_p} \tag{4.15}$$

where ρ is the density. With equations 4.13 and 4.14 the temperature-dependent diffusivity can be calculated. Temperature dependence of diffusivity and specific heat are shown in fig. 4.22.

4.3.2. Heat diffusion length considerations

A simple way to characterise the effect of heating of a glass is by the heat diffusion length *l(t)*. It is a measure for the volume which is affected by heat diffusion within a given time. The absorption length l_a determines the size of the volume that is heated directly by laser irradiation. If $l(t)<l_a$ then heat diffusion has only a small effect on the final temperature distribution, and it can be neglected.

The heat diffusion length is given by[121]:

$$l(t)=\sqrt{\frac{k\,t}{\rho\,c_p}}=\sqrt{D\,t} \tag{4.16}$$

The temperature dependence of D can not be included in this calculation. D is approximated with $D = 5\cdot10^{-7}$ m^2s^{-1}, which is close to the actual value for up to 1000°C.

With these values the thermal diffusion length can be calculated. It becomes equal to l_a of non-irradiated material after 3 ms. This is 240 times the time between two laser pulses, so the pulsed nature of the laser can be neglected under these conditions. It is shorter than the time of total irradiation of each spot for 340 pulses/spot used in the experiments, so heat conduction has a considerable influence on final temperatures. Also thermal diffusion length on the timescale of irradiation is considerably larger than the beam radius of 30µm. So it would not be sufficient to calculate heat diffusion in only one

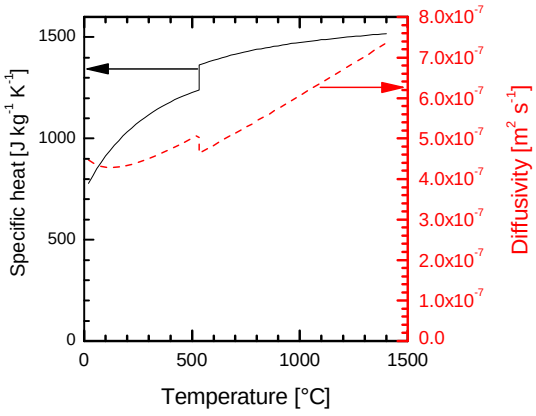

Fig. 4.22: Temperature dependence of specific heat (black, solid), left axis, and diffusivity shown in red, dashed, right y axis.

dimension.

The thermal diffusion length for the 10 ns laser pulse length is 72nm, while for 10ps it is only 2.3nm. This is a lot smaller than the absorption length of non-irradiated and particle-containing glass, which explains why experimental results for the two different pulse lengths are macroscopically nearly identical. However SEM images show smaller particle sizes for ns-pulsed irradiation than for ps-pulsed irradiation with the same fluence. This indicates a different behaviour for both pulse lengths when the surface particle film is formed. This could be caused by either nonlinear absorption effects in the metallic surface layer, or by the reduction of the absorption length below the thermal diffusion length for 10ns. This diffusion length might be considerably larger than that of glass due to the change to a more metallic composition.

4.3.3. Comsol simulation of laser heating of glass

Comsol is a simulation package utilising finite element methods (FEM). It started as a Matlab package but is a stand-alone program with its own interface nowadays. It combines modelling software from different areas of physics.

A Comsol model can be set up in a few steps. First the modelling dimensions and simulated physics are chosen. Dimensions can be 1d, 2d and 3d. The lower dimensional simulations can represent higher dimensional objects by translational and rotational symmetries. Next the geometry of the object has to be created, including additional symmetries to speed up the simulation. Materials can be chosen from a library, which contains properties of many different materials, but also allows making own entries. Energy sources and boundary conditions must be set. Then the mesh is created, which

defines how the object is divided into elements for the FEM simulation.

The simulation of laser heating of glass has been set up based on a provided example, which simulates the laser heating of a wafer. The glass is modelled in three dimensions. Only the heat transfer in solids module is used for this model. It simulates the heat conduction inside the glass, and the heat loss due to radiation to the ambient.

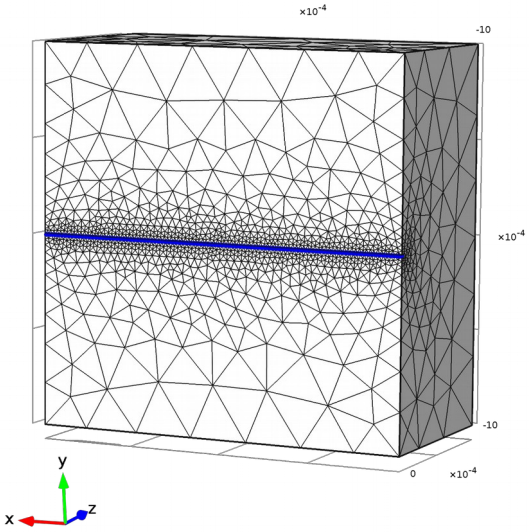

Fig. 4.23: Generated mesh. The block added to create a finer mesh around the laser line is shown in blue.

The laser heating itself is simulated by adding a heat source to the model. The heating is assumed to be homogeneous in the depth of the glass (z direction). The thickness of the heated layer is set to 22µm. This is lower than the actual absorption length at room temperature to partly compensate for the decrease of absorption length during the process. The width and height of the heated region are set to 60µm, similar to the beam diameter. The heated area is moving with the laser scanning speed of 14mm/s.

The other material parameters of B270 have been added to the library as temperature-dependent functions as presented in section 4.3.1.

The size of the simulated glass piece has been set to a thickness of 1mm, and 2mm height and width. Normally Comsol creates a homogeneous mesh for the whole simulated object. This means that the mesh would either be coarse over or fine the whole block of glass. But a coarse mesh can not simulate the heat generated by a narrow

laser beam correctly, and a fine mesh will take a very long time to be solved. Therefore another block of 3 µm width and depth was added in the centre of the laser-written line. Comsol generates 3µm-sized elements within this block. The maximum element growth rate was set to 1.3. This means that adjacent elements are no more than 1.3 times as large. So a very fine mesh is generated in the centre of the laser line, which becomes more coarse to the borders of the glass. It is shown in fig. 4.23.

4.3.3.1. Parameter testing

A first simulation was run for a continuous heating with 0.48W, which is equivalent to a pulse energy of 6µJ at 80kHz repetition rate. The surface emissivity of the glass was set to 0.5. In this first run the effect of different mesh sizes was tested by setting the size of the block added to the centre of the line to 3µm and 10µm. The temperature distribution of the resulting simulation is shown in fig. 4.24. The 10µm block result is shown on the

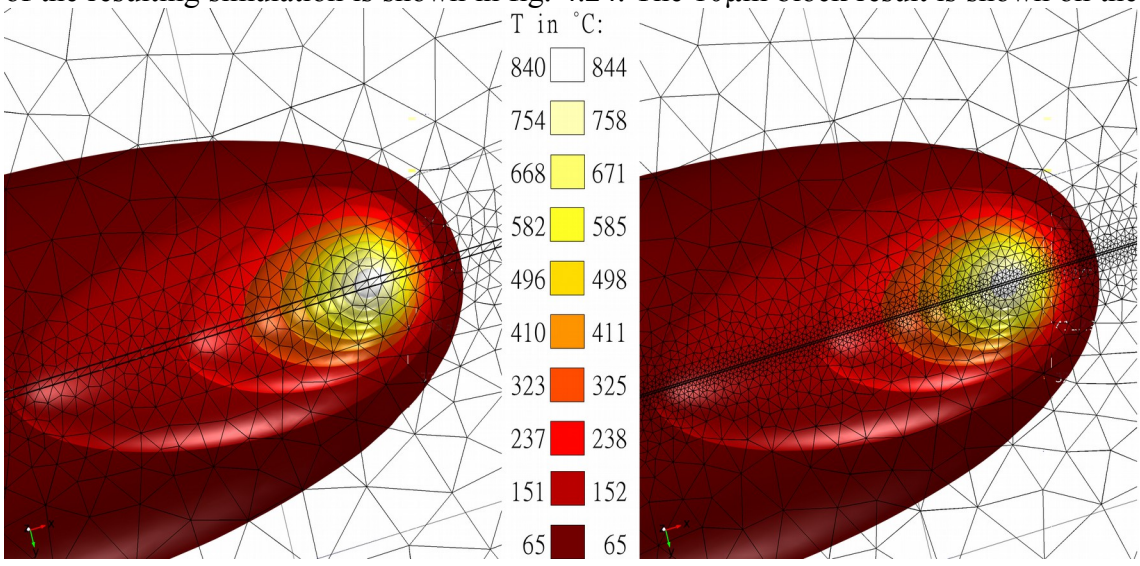

Fig. 4.24: Temperature profiles for two tests with different mesh sizes: The added block in laser focus is 10µm on the left side and 3µm on the right. The resulting mesh is shown as black lines. It is much finer mesh for the simulation result shown on the right. The resulting isothermal contours are shown in different colours from red for low temperatures to bright yellow for high temperatures. They are very similar, the maximum temperature is 4K larger for the finer mesh, which is negligible.

left, the 3µm on the right. Temperatures are represented by contours in different colours, the colour legend is in the right of each image. The meshes are also shown in grey.

These two simulations produce nearly identical results. The peak temperature for the 10µm grid is 840°C, while it is 844°C for the 3µm grid. Although the 10µm grid would be sufficient for further simulations the 3µm setting has been used since the calculation time was still acceptable.

Next the relevance of head radiation to the surrounding was tested by changing the emissivity parameter. The emissivity is a dimensionless number that characterises how much heat a material radiates to the ambient. It is defined as the ratio to the heat radiation of an ideal black body, which has an emissivity of one. An emissivity of zero means that no heat is emitted.

The emission of thermal radiation occurs over a broad wavelength range, which is centred at approximately 10µm at room temperature. At higher temperatures it is shifting to shorter wavelengths. The emissivity depends on the absorptivity at the wavelengths of thermal emission An ideal black body has the highest possible emissivity, while an ideally white or reflecting body has an emissivity close to zero. For glass the emissivity is 0.92 at room temperature, which is close to a black body. Silver on the contrary has an emissivity of 0.02. Though since the reflectivity of silver reduces strongly with increasing temperature the emissivity will increase when the temperature rises. So the emissivity should stay closer to the value of glass during the experiment.

Simulations were run for the whole range of emissivities from zero to one. The resulting peak temperatures are plotted in fig. 4.25. This shows that an emissivity of 1 decreases the peak temperature by less than 2K. Therefore emissivity does not need to be included

in modelling.

A very important heat loss mechanism is the boiling of material, which leads to ablation. This is not included in the presented simulations since it requires a quite high spatial and temporal resolution. Normally such simulations are done in 1d, only recently also in 2d [122]. The shown experiment would require a 3d simulation though. Therefore the heat loss due to ablation is not modelled, though it can still be determined if the ablation threshold is reached.

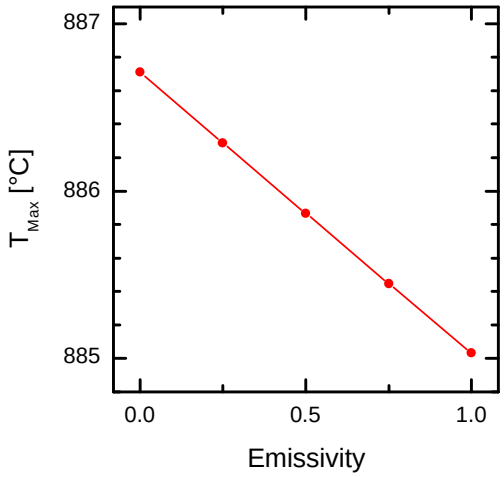

Fig. 4.25: The effect of the emissivity parameter on the maximum temperature

4.3.3.2. Simulation results

Simulations were run for different pulse energies from zero to 14 µJ every 0.25µJ. For each energy the peak temperature and the width of the area that exceeds a temperature of 550°C was determined. The obtained values are plotted in fig. 4.26.

At 3µJ a temperature around 500°C are reached, which can explain the formation of nanoparticles inside the glass. At 6µJ the maximum temperature is only 885°C. This temperature does not induce the formation of gas bubbles if the glass is heated in the furnace. This shows that higher temperatures are reached, since the absorption length is reducing further than the 22µm used for the simulation, and since the pulsed nature of irradiation is not modelled.

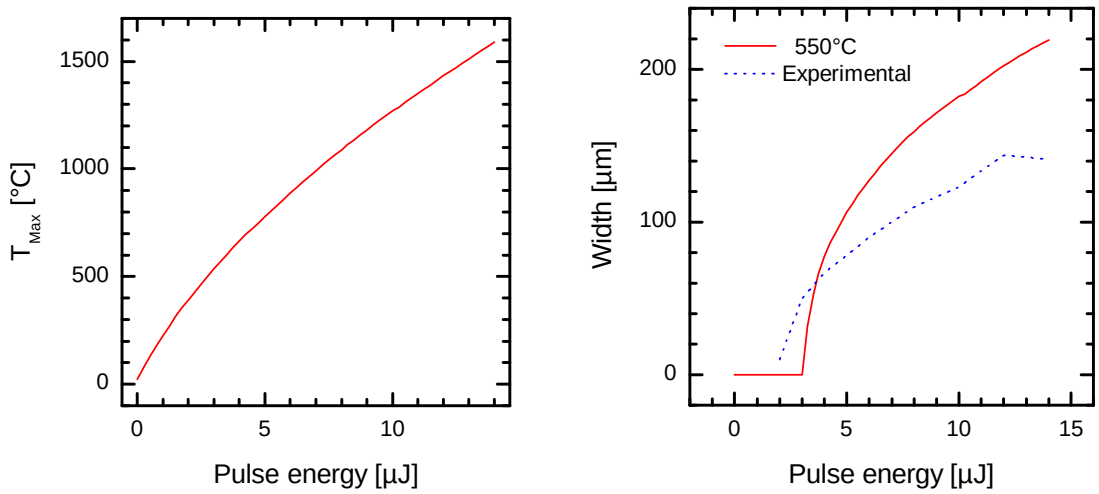

Fig. 4.26: Effect of different laser power (pulse energy). Left: Maximum temperature. Right: Width that exceeds a temperature of 550°C, and experimentally determined line width containing nanoparticles for comparison (ps pulses).

The width exceeding a temperature of 550°C should be comparable to the line width that contains silver nanoparticles in the glass volume. The graph shows this experimental line width measured in transmission mode on lines written with ps pulses. For low pulse energies the widths are in considerably good agreement. For high pulse energies the simulation shows a much broader area with 550°C or more than the experimentally determined area width containing nanoparticles. This difference between model and experiment can be explained by ablation, which is not simulated in the model. It is taking heat away from the piece of glass at high enough pulse energies, which then can not contribute to the heating of a wider area of the glass.

4.3.4. Analytical solution

Simulating pulsed laser irradiation in three dimensions over many pulses with Comsol would drastically increase the computation time. This can better be done in an analytical

solution, which is presented here. This also allows to do simulations for a wide range of absorption lengths down to the nanometre range without the hassle of the high spatial resolution that would be needed in a Comsol model.

4.3.4.1. The model

The heat equation (eq. 4.11) can be solved analytically by the Green's function method. The solution is given by [123]:

$$T(\vec{x},t)=\int_{-\infty}^{+\infty} G(\vec{x},\vec{x}',t)\,T(\vec{x}',0)\,d\vec{x}' \tag{4.17}$$

where $T(\vec{x}',0)$ is the initial condition at t=0, and $G(\vec{x},\vec{x}',t)$ is the Green's function. For the heat equation with no boundary condition the Green's function is [124]:

$$G(\vec{x},\vec{x}',t)=\frac{\exp-\frac{|\vec{x}-\vec{x}'|^2}{4Dt}}{(4\pi Dt)^{d/2}} \tag{4.18}$$

d is the number of dimensions in $\vec{x}$, which is 3 here.

It is assumed that the glass is filling the $z > 0$ half space. The laser irradiates the glass coming from the -z direction. It scans over the sample surface in x direction at $y = 0$, with a scanning speed of v = 14mm s^{-1}, starting at $x = 0$. The repetition rate of the laser f is 80000 s^{-1}. To obtain a problem with no boundary condition the whole simulation is mirrored at the $z = 0$ plane. The temperature distribution in both half spaces is identical, therefore no heat transfer occurs at $z = 0$. This is identical to the simulation of a glass limited to one half space with a no heat transfer boundary condition at the surface.

Since the heat equation is a linear differential equation the temperature distribution after Nth laser pulse can be written as a sum of the temperature changes caused by the

individual pulses before [125]:

$$T(t',x',y,z)=\sum_{n=0}^{N-1}\Delta T_1\left(t'-\frac{n}{f},x'-v\frac{n}{f},y,z\right)+T_0 \tag{4.19}$$

where ΔT_1 is the temperature change induced by a single pulse, T_0 is the initial temperature.

To calculate ΔT_1 the temperature change induced by a single pulse is taken as initial condition for the Green's function method:

$$\Delta T_1(0,x,y,z)=\frac{Q(x,y,z)}{V\rho c_p} \tag{4.20}$$

The heat generated per volume is equal to the absorbed laser energy:

$$\frac{Q(x,y,z)}{V}=\frac{\alpha E_P}{\pi w_0^2}\exp\left(-\frac{x^2+y^2}{w_0^2}+\alpha|z|\right) \tag{4.21}$$

By taking the absolute value of z the simulated laser heating is mirrored at $z = 0$.

Inserting ΔT_1 into equation 4.17 as $T(\vec{x}',0)$ and integrating results in:

$$\begin{aligned}\Delta T_1(t,x,y,z)&=\frac{\alpha E_P}{2\pi\rho c_p(4Dt+w_0^2)}\cdot\ldots\\ \ldots\cdot\exp\left(-\frac{x^2+y^2}{4Dt+w_0^2}+\alpha^2 Dt\right)&[f_z(z,t)+f_z(-z,t)]\end{aligned} \tag{4.22}$$

with

$$f_z(z,t)=\exp(\alpha z)\operatorname{erfc}\frac{z+2\alpha Dt}{2\sqrt{Dt}} \tag{4.23}$$

Solving a differential equation analytically becomes very difficult if the equation is not linear. Therefore the temperature dependence of the diffusivity is not included in the model, instead it is set constant to $5\cdot10^{-7}$ m^2s^{-1}. With that the achieved maximum temperature becomes a linear function of the pulse energy. This relation was plotted for

the Comsol simulation results in the left graph in fig. 4.26, which shows that the results do not differ much from the linear relation obtained with this approximation,

4.3.4.2. Simulation results

With temperature-independent material parameters and without heat loss to the environment the resulting temperatures become proportional to the laser pulse energy. Ep only occurs as a factor in ΔT_1 in the formula. Therefore simulations are run only for 6µJ, results for all other energies can easily be calculated from this. This is the pulse energy range where bubble formation starts, and two to three times the pulse energy of the onset of particle formation in the volume.

Simulations were run for different absorption lengths since absorption lengths are

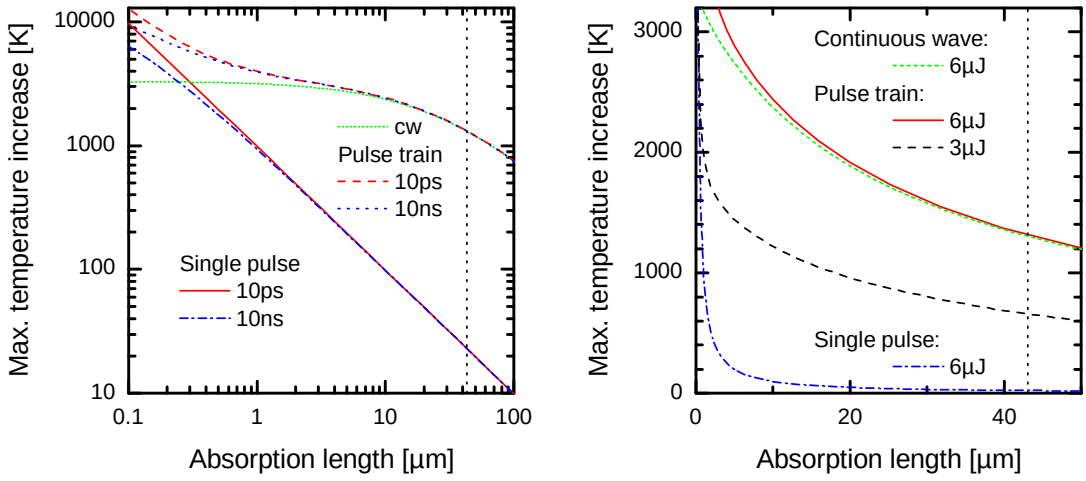

Fig. 4.27: Simulated heating of ion exchanged glass for 6µJ pulse energy. Graphs show peak temperatures after single pulse heating and after scanning irradiation as a function of absorption length. The vertical dotted black line marks the absorption length of non-irradiated glass of 43µm. The left graph is plotted on logarithmic scale to show the differences between ps and ns pulsed irradiation at small absorption lengths. The right graph is on linear scales, and the maximum temperature for 3µJ irradiation is added.

changing during the experiment and not exactly known. 10000 laser pulses were simulated, and the maximum temperature increase in the glass was obtained for each simulation. Also the maximum temperature increase by a single laser pulse for different absorption lengths was calculated to compare the absorption length dependence. The results of this simulation are shown in fig. 4.27 on a double-logarithmic scale. It also includes the results of a continuous wave simulation for comparison. This simulation was done according to a publication by Sanders [126].

The left graph shows that ns and ps pulsed irradiation only result in different temperatures for absorption lengths below 300 nm. Both irradiations have different effects such as different particle sizes and different surface profiles. Therefore the absorption length in the surface layer must be reduced below about 300 nm during irradiation. The increase in heat conductivity, which is not included in the modelling, can increase this limit. From diffusion length considerations a limit of 72 nm was deduced, which is equivalent to a more clear difference in peak temperature. Continuous wave and pulsed irradiation result in different temperatures for absorption lengths below about 3µm. The thermal diffusion length for the time between two pulses is 2.5µm. So the thermal diffusion length considerations are confirmed by this simulation.

The dashed black curve in the right graph shows the maximum temperature increase for irradiation with 3µJ pulses. At the initial absorption length the maximum temperature increase is 700K, which is above the transition temperature of the glass and sufficient to explain the observed generation of nanoparticles inside the glass.

For 6 µJ bubble formation is observed. It has to be taken into account that absorption lengths are reducing considerably during the process. Bubble formation can result from

boiling and decomposition of the glass, which occurs at about 2500°C. Such temperatures would be achieved with a constant absorption length of 10µm. In the actual experiment larger and smaller absorption lengths occur.

When higher temperatures are occurring in the simulation evaporation will happen, which will result in ablation.

4.3.5. Modelling conclusions

Accurate heating simulations of the experiments are hampered by a strongly changing absorption length during the experiment, and uncertainty about its actual value at elevated temperatures. However conclusions can still be drawn from simulations done over a range of parameters.

A simple heat diffusion length analysis with comparison to the absorption length shows where heat conduction is relevant. The original ion-exchanged glass has a large absorption length of 43µm at the laser wavelength. In this state not only the pulse length is irrelevant, but also the pulsed nature of the laser irradiation. This explains strong similarities of the results of ps and ns pulsed irradiation. The analysis also shows that a heat simulation must be done in 3d because the spreading of heat to the sides is influencing the achieved temperatures.

The diffusion length analysis already shows that the absorption length must be reduced to roughly 100nm to explain differences between ns and ps pulsed irradiations. Analytical modelling confirms this limit.

Both models allow to conclude that at 3µJ temperatures needed for particle formation in the glass are achieved, which explains nanoparticle formation in the glass. Also bubble

formation can be explained by the glass reaching the boiling point and decomposition temperature, but only if the reduction of absorption length is taken into account.

The Comsol simulation showed that radiative heat loss can be neglected. Though simulated widths of glass exceeding 550°C are much wider than generated line widths. This shows that there is considerable heat loss due to evaporation, which results in ablation.

The modelling could be improved by a more sophisticated simulation of the laser irradiation, including a temperature-dependent absorption coefficient. This is difficult to do in an analytical solution. Therefore it should be done in a numerical model such as the Comsol modelling. It would also be interesting to include ablation in the simulation [122], though this requires a very fine mesh, which requires to switch to a 2d simulation. Both improvements are far from trivial, and the benefit of such simulations would be only small since the temperature dependence of the material properties, especially the absorption length are not known for certain. If such simulations are needed the experiment should be changed to simplify modelling, e.g. by non-scanning irradiation, which makes the problem cylindrically symmetrical. This would allow to do the simulation in 2d. The analytical solution would be reduced to the calculation for a single point in that case. Though the experimental analysis of the induced changes becomes more difficult in that case. It has to be done either on single spots or on an array of spots. Though such an array would show much more of the effects at the edge of the modified area. Larger beam diameters would help with these problems.

Also a different laser wavelength with a lower temperature dependence of the absorption length would make simulations easier, for example a wavelength of 300nm

or less, or possibly a CO_2 laser.

4.4. Discussion of mechanisms creating the surface structure

The GSC has exciting and unexpected properties. Most fascinating is the formation of a near regular pattern of silver particles at the glass surface.

4.4.1. Comparable structures in literature

A comparable metallic shine has already been created in lustre decoration of ceramics [127]. Lustre glazing of ceramics is a technique that was developed in medieval Mesopotamia, where it first came up in the 9th century. Very different shiny colours were achieved, like golden-yellow, blue, green, pink. The optical effects are caused by a layer with highly-concentrated silver nanoparticles [128]. This was created by applying a paint containing silver or copper salts and annealing in a reducing atmosphere. The microscopic structure of these nanoparticles is different from the GSC nonetheless. The nanoparticles are randomly distributed within a layer under the surface of the ceramic, similar to conventional glasses with silver nanoparticles, yet with a much higher particle concentration.

Laser irradiation of metallic films can result in randomly distributed metal structures [129]. Irradiation of gold films on glass can produce quite regular nanoparticle structures [130, 131]. These have comparable appearance to the surface structure of the GSC.

4.4.2. Formation mechanisms

The required electrons for the start of aggregation can be provided by the 2p orbital of

non-bridging oxygen in the SiO_4 polyhedron via the multi-photon absorption of the incident photon [132-135] by ionisation [132] multi-photon absorption from fs laser [135]. Here, absorption of the laser beam and intense irradiation ensured for a vast number of silver ions to be able to acquire sufficient energy to reduce to silver atoms with the resultant aggregation. The electron gas of the aggregated particles then further absorbs the light pulses leading to the fabrication of metallic silver. It was recently shown that in the earliest moment of irradiation, there could exist a large discrepancy between electron and lattice temperatures and before thermal equilibrium can be achieved [136]. This process can lead to a phase change mechanism resulting in formation of metallic silver and fabrication of GSC.

It is known that a glass melt can contain only limited amount of silver, much lower than the concentrations achieved by ion exchange at lower temperatures. If silver salts are added to a glass melt when the glass is manufactured it can only be dissolved in amounts of 0.003-0.1 wt-% -% [50]. Larger amounts of silver separate from the melt in metallic form. Over the long duration of glass melting this can result in a single agglomeration of silver, but over the duration of laser irradiation only shorter diffusion lengths can be expected. This process might also result in the precipitation of silver at the glass surface. However our analysis showed that surface particle formation occurs when the temperature reaches the boiling point of the glass.

Our thermal modelling shows that the glass is heated above the softening point during laser irradiation. This causes the separation of silver from the glass as a metallic film on the surface. This film consists of molten silver since the temperature exceeds the melting temperature of silver, which is 861.78°C. As the SEM images showed the silver

is forming a regular pattern of even-sized nanoparticles. The separation into nanoparticles is indicates that the silver is not wetting the glass. It is separated into nanoparticles by its surface tension.

Interesting is the regularity of the nanoparticle layer. There must be a mechanism that causes an even distribution of the silver, an exchange between the individual nanoparticles. At higher temperatures the surface tension of silver decreases [137], so the silver could form a cohesive uniform film. Only after cooling down, before freezing, it is separating into nanoparticles, which have similar size because of the homogeneous thickness of the film.

On the sides of the laser-written lines the silver shows a different, much more irregular structure. The maximum temperature has been lower in this region, therefore this silver was not molten like that in the centre of the line.

4.5. Summary and conclusions

Laser irradiation of the ion exchanged B270 glass had a very interesting effect, giving the glass surface a metallic shine. This turned out to be a new kind of material, which was discovered in the course of this work and not found in any publications. The discovery of the material[108] and an analysis of the process and its properties [109] were published. A patent was filed on the manufacturing process [110].

We called the material Glass-silver composite (GSC). The ion exchanged B270 glass presented in chapter 2 was irradiated with pulsed lasers with 10ns and with 10ps pulse length and a wavelength of 355nm. Macroscopically the material shows a metallic reflection similar to a rough silver surface. Imaging with a scanning electron

microscope revealed a dense monolayer of large silver nanoparticles at the glass surface. These particles have a quite narrow size distribution, and the particle sizes can be controlled by the laser pulse energy.

Main focus when analysing this material was to understand the formation mechanism. Surface profiling showed the occurrence of ablation for high pulse energies. The laser irradiation also generates nanoparticles within the glass volume. At pulse energies between 2 and 5μJ this is the only process. It has been shown that the formation process starts at pulse energies which are sufficient to heat the glass to the boiling point. The particle formation in the glass volume is linked to temperatures similar to these used to generate nanoparticles in the glass by annealing.

In the future we will be looking for applications for the newly found glass silver composite. It is a very promising candidate for surface enhanced Raman scattering (SERS). A characterisation of this material's SERS properties is being prepared with Dr Svetlana Zolotkovskaya. Other possible applications are as a chemical catalyst, for plasmonic nanotechnology and sensors and possibly in the field of terahertz generation.

5. Summary of the work and outlook

In this work two different types of silver-glass nanocomposites were analysed. The first material is glass with silver nanoparticles, which contains nanoparticles inside the glass. The second material is called glass-silver composite. Both materials are based on silver ion exchanged glass, which was also characterised. Materials were produced with different parameters and characterised by optical methods and scanning electron microscopy (SEM). Understanding of the processes has been improved.

Silver ion exchanged B270 glass was fabricated by field-assisted ion exchange at 300°C with different applied voltages. The electrical current flow was measured and recorded, and the transferred electrical charge determined. SEM imaging allowed to measure the thickness of the ion exchanged layer. It was found that charge transfer and layer thickness are correlated by a linear relation, the resulting layer thickness is 16.2 ± 1.4 µm / (As cm^{-2}). There were damages occurring at the negative side of the glass, which are attributed to oxygen ion depletion, while colour changes in that area are explained by hydroxide ion exchange.

The ion exchanged B270 glass was annealed at 550°C, which induced the formation of silver nanoparticles inside the glass. Thin slices of the cross sections of this material were prepared and analysed with a microscope spectrometer. Simulation of the absorption of the composite material utilising the Maxwell Garnett theory allowed to find particle filling factors and particle sizes.

A series with different annealing times allowed to analyse the development of the particle-containing layer over time. Filling factor profiles were obtained from

simulations of the measured spectra. These were compared to a diffusion simulation, which simulates the formation of the particle layer from freely diffusing silver. In principle this simulation agreed with the experimental results, but it also showed interesting differences. The experimental results show a steeper profile, with the steepness changing only minimally with diffusion times. Diffusion simulation shows a concentration profile that becomes considerably more flat over time. Also diffusion depths for longer annealing are smaller compared to the simulation. This shows that there is a slowing-down effect at the edge of the silver-containing layer, compared to the diffusion within the layer. This is explained by the formation of percolated pathways.

A second series of experiments was performed with varying exchange voltages. This allows to greatly vary the thickness of particle containing layers. Interestingly there was no indication of a variation of nanoparticle concentrations within the layers for different voltages. This effect narrows down the potential reduction mechanisms. In B270 reduction must be related to non-bridging oxygen, because it is a high purity glass free of other reducing agents. Reduction must be limited to certain sites in the glass, possibly anion dimer sites which are occupied by two silver ions.

The second analysed material, which was first presented in the course of this work, is called glass-silver composite. It is manufactured by pulsed laser irradiation of the silver ion exchanged glass. Macroscopically it exhibits a metal-like reflection. SEM imaging shows the reflection is caused by a dense monolayer of large silver nanoparticles at the glass surface. These particles have a quite narrow size distribution, and the particle sizes can be controlled by the laser pulse energy.

Main focus when analysing this material was to understand the formation mechanism.

Surface profiling showed the occurrence of ablation for high pulse energies. The laser irradiation also generates nanoparticles within the glass volume. At pulse energies between 2 and 5µJ this is the only process. It has been shown that the formation process starts at pulse energies which are sufficient to heat the glass to the boiling point. The particle formation in the glass volume is linked to temperatures similar to these used to generate nanoparticles in the glass by annealing.

In the future we will be looking for applications for the newly found glass silver composite. It is a very promising candidate for surface enhanced Raman scattering (SERS). A characterisation of this material's SERS properties is being prepared with Dr Svetlana Zolotkovskaya. Other possible applications are as a chemical catalyst, for plasmonic nanotechnology and sensors and possibly in the field of terahertz generation.

References

1. Kreibig, U. and M. Vollmer, *Optical Properties of Metal Clusters*. 1995: Springer.

2. Brongersma, M.L. and P.G. Kik, *Surface Plasmon Nanophotonics*. 2007: Springer.

3. Daniel, M.-C. and D. Astruc, *Gold nanoparticles: assembly, supramolecular chemistry, quantum-size-related properties, and applications toward biology, catalysis, and nanotechnology.* Chemical Reviews, 2004. **104**(1): p. 293-346.

4. Otto, A., *Excitation of non-radiative surface plasma waves in silver by the method of frustrated total reflection.* Zeitschrift für Physik, 1968. **216**(4): p. 398-410.

5. Wagner, F.E., S. Haslbeck, L. Stievano, S. Calogero, Q. Pankhurst, and K.-P. Martinek, *Before striking gold in gold-ruby glass.* Nature, 2000. **407**(6805): p. 691-692.

6. Mie, G., *Beiträge zur Optik trüber Medien, speziell kolloidaler Metallösungen.* Annalen der Physik, 1908. **330**(3): p. 377-445.

7. Kreibig, U. and P. Zacharias, *Surface plasma resonances in small spherical silver and gold particles.* Zeitschrift für Physik, 1970. **231**(2): p. 128-143.

8. Kelly, K.L., E. Coronado, L.L. Zhao, and G.C. Schatz, *The Optical Properties of Metal Nanoparticles: The Influence of Size, Shape, and Dielectric Environment.* J. Phys. Chem. B, 2003. **107**: p. 668-677.

9. Fleischmann, M., P. Hendra, and A. McQuillan, *Raman spectra of pyridine adsorbed at a silver electrode.* Chemical Physics Letters, 1974. **26**(2): p. 163-166.

10. Leopold, N. and B. Lendl, *On-column silver substrate synthesis and surface-enhanced Raman detection in capillary electrophoresis.* Analytical and Bioanalytical Chemistry, 2010. **396**(6): p. 2341-2348.

11. Volkan, M., D.L. Stokes, and T. Vo-Dinh, *A new surface-enhanced Raman scattering substrate based on silver nanoparticles in sol–gel.* Journal of Raman Spectroscopy, 1999. **30**(12): p. 1057-1065.

12. Kneipp, K., Y. Wang, H. Kneipp, L.T. Perelman, I. Itzkan, R.R. Dasari, and M.S. Feld, *Single molecule detection using surface-enhanced Raman scattering (SERS).* Physical Review Letters, 1997. **78**(9): p. 1667.

13. Le Ru, E.C. and P.G. Etchegoin, *Single-molecule surface-enhanced Raman spectroscopy.* Annual Review of Physical Chemistry, 2012. **63**: p. 65-87.

14. Hallermann, F., C. Rockstuhl, S. Fahr, G. Seifert, S. Wackerow, H. Graener, G.v. Plessen, and F. Lederer, *On the use of localized plasmon polaritons in solar cells.* physica status solidi (a), 2008. **205**(12): p. 2844-2861.

15. Trupke, T., M. Green, and P. Wurfel, *Improving solar cell efficiencies by up-conversion of sub-band-gap light.* Journal of Applied Physics, 2002. **92**(7): p. 4117-4122.

16. Aisaka, T., M. Fujii, and S. Hayashi, *Enhancement of upconversion luminescence of Er doped AlO films by Ag island films.* Applied Physics Letters, 2008. **92**: p. 132105.

17. Mertens, H. and A. Polman, *Plasmon-enhanced erbium luminescence.* Applied Physics Letters, 2006. **89**(21): p. 211107-3.

18. Trupke, T., M. Green, and P. Wurfel, *Improving solar cell efficiencies by down-conversion of high-energy photons.* Journal of Applied Physics, 2002. **92**(3): p. 1668-1674.

19. Borek, R., K.-J. BERA, and G. Berg, *Low-temperature tensile deformation of flat glass containing metal particles to generate dichroism.* Glass Science and Technology, 1998. **71**(12): p. 352-359.

20. Kaempfe, M., T. Rainer, K.J. Berg, G. Seifert, and H. Graener, *Ultrashort laser pulse induced deformation of silver nanoparticles in glass.* Applied Physics Letters, 1999. **74**(9): p. 1200-1202.

21. Unal, A.A., A. Stalmashonak, H. Graener, and G. Seifert, *Tuning the shape anisotropy of silver nanoparticles using time-delayed laser pulse pair irradiations.* Applied Physics B, 2010. **101**(4): p. 841-847.

22. Kaempfe, M., *Laserinduzierte Deformation metallischer Nanopartikel in Gläsern*. 2000, Martin-Luther-Universität Halle-Wittenberg.

23. Stalmashonak, A., G. Seifert, A.A. Unal, U. Skrzypczak, A. Podlipensky, A. Abdolvand, and H. Graener, *Toward the production of micropolarizers by irradiation of composite glasses with silver nanoparticles.* Applied Optics, 2009. **48**(25): p. F37-F43.

24. Stalmashonak, A., A. Abdolvand, and G. Seifert, *Metal-glass nanocomposite for optical storage of information.* Applied Physics Letters, 2011. **99**(20): p. 201904-3.

25. Stalmashonak, A., A.A. Unal, H. Graener, and G. Seifert, *Effects of Temperature on Laser-Induced Shape Modification of Silver Nanoparticles Embedded in Glass.* Journal of Physical Chemistry C, 2009. **113**(28): p. 12028-12032.

26. Deparis, O., P.G. Kazansky, A. Abdolvand, A. Podlipensky, G. Seifert, and H. Graener, *Poling-assisted bleaching of metal-doped nanocomposite glass.* Applied Physics Letters, 2004. **85**(6): p. 872.

27. Abdolvand, A., A. Podlipensky, S. Matthias, F. Syrowatka, U. Gösele, G. Seifert, and H. Graener, *Metallodielectric Two-Dimensional Photonic Structures Made by Electric-Field Microstructuring of Nanocomposite Glasses.* Advanced Materials, 2005. **17**(24): p. 2983-2987.

28. Fleming, L.A., S. Wackerow, A.C. Hourd, W.A. Gillespie, G. Seifert, and A. Abdolvand, *Diffractive optical element embedded in silver-doped nanocomposite glass.* Optics Express, 2012. **20**(20): p. 22579-22584.

29. Liedberg, B., C. Nylander, and I. Lunström, *Surface plasmon resonance for gas detection and biosensing.* Sensors and actuators, 1983. **4**: p. 299-304.

30. Stewart, M.E., C.R. Anderton, L.B. Thompson, J. Maria, S.K. Gray, J.A. Rogers, and R.G. Nuzzo, *Nanostructured plasmonic sensors.* Chemical Reviews, 2008. **108**(2): p. 494-521.

31. Lobet, M.l. and O. Deparis, *Plasmonic device using backscattering of light for enhanced gas and vapour sensing.* 2012: p. 842509-842509.

32. Quinten, M., A. Leitner, J. Krenn, and F. Aussenegg, *Electromagnetic energy transport via linear chains of silver nanoparticles.* Optics Letters, 1998. **23**(17): p. 1331-1333.

33. Maier, S.A., P.G. Kik, and H.A. Atwater, *Observation of coupled plasmon-polariton modes in Au nanoparticle chain waveguides of different lengths: Estimation of waveguide loss.* Applied Physics Letters, 2002. **81**(9): p. 1714-1716.

34. Kilty, P.A. and W.M.H. Sachtler, *The mechanism of the selective oxidation of ethylene to ethylene oxide.* Catalysis Reviews, 1974. **10**(1): p. 1-16.

35. Jiang, Z.-J., C.-Y. Liu, and L.-W. Sun, *Catalytic properties of silver nanoparticles supported on silica spheres.* The Journal of Physical Chemistry B, 2005. **109**(5): p. 1730-1735.

36. Kamat, P.V., *Photophysical, photochemical and photocatalytic aspects of metal nanoparticles.* Journal of Physical Chemistry B, 2002. **106**(32): p. 7729-7744.

37. Moroz, A., *Three-dimensional complete photonic-band-gap structures in the visible.* Physical Review Letters, 1999. **83**(25): p. 5274.

38. Stepanov, A., *Nonlinear optical properties of implanted metal nanoparticles in various transparent matrixes: a review.* Rev. Adv. Mater. Sci, 2011. **27**: p. 115-145.

39. Mohan, S., J. Lange, H. Graener, and G. Seifert, *Surface plasmon assisted optical nonlinearities of uniformly oriented metal nano-ellipsoids in glass.* Opt. Express, 2012. **20**(27): p. 28655-28663.

40. Lamprecht, B., A. Leitner, and F.R. Aussenegg, *Femtosecond decay-time measurement of electron-plasma oscillation in nanolithographically designed silver particles*. Applied Physics B-Lasers and Optics, 1997. **64**(2): p. 269-272.

41. Chakraborty, P., *Metal nanoclusters in glasses as non-linear photonic materials.* Journal of Materials Science, 1998. **33**(9): p. 2235-2249.

42. Griscom, D.L., *Optical properties and structure of defects in silica glass.* Nippon Seramikkusu Kyokai Gakujutsu Ronbunshi/Journal of the Ceramic Society of Japan, 1991. **99**(1154): p. 923-942.

43. Frischat, G.H., *Tin ions in float glass cause anomalies.* Comptes Rendus Chimie, 2002. **5**(11): p. 759-763.

44. Colombin, L., A. Jelli, J. Riga, J.J. Pireaux, and J. Verbist, *Penetration depth of tin in float glass.* Journal of Non-Crystalline Solids, 1977. **24**(2): p. 253-258.

45. Shelby, J.E. and J. Vitko Jr, *Colloidal silver formation at the surface of float glass.* Journal of Non-Crystalline Solids, 1982. **50**(1): p. 107-117.

46. Rainer, T., *Laserstrahlinduzierte Bildung von Silbernanopartikeln in Glas - Modell der Partikelbildung* -. 2002, Martin-Luther-Universität Halle-Wittenberg.

47. Sperber, H., *Herstellung von Formaldehyd aus Methanol in der BASF.* Chemie Ingenieur Technik, 1969. **41**(17): p. 962-966.

48. Compton, W. and J. Schulman, *Colour centres in solids*. 1962, Pergamon Press, London.

49. Kreibig, U., *Small silver particles in photosensitive glass: their nucleation and growth.* Applied physics, 1976. **10**(3): p. 255-264.

50. Vogel, W., *Glaschemie*. 1992: Springer Berlin etc.

51. Berger, A., *Concentration and size depth profile of colloidal silver particles in glass surfaces produced by sodium-silver ion-exchange.* Journal of Non-Crystalline Solids, 1992. **151**: p. 88-94.

52. Pinchuk, A., G.v. Plessen, and U. Kreibig, *Influence of interband electronic transitions on the optical absorption in metallic nanoparticles.* Journal of Physics D: Applied Physics, 2004. **37**(22): p. 3133.

53. Bruggeman, D.A.G., *Berechnung verschiedener physikalischer Konstanten von heterogenen Substanzen. I. Dielektrizitätskonstanten und Leitfähigkeiten der Mischkörper aus isotropen Substanzen.* Annalen der Physik, 1935. **416**(7): p. 636-664.

54. Hinsen, K. and B. Felderhof, *Dielectric constant of a suspension of uniform spheres.* Physical Review B, 1992. **46**(20): p. 12955-12963.

55. Drude, P., *Zur Elektronentheorie der Metalle.* Annalen der Physik, 1900. **306**(3): p. 566-613.

56. Drude, P., *Zur Elektronentheorie der Metalle; II. Teil. galvanomagnetische und thermomagnetische Effecte.* Annalen der Physik, 1900. **308**(11): p. 369-402.

57. Ma, Y., J. Lin, J. Chen, Z. Feng, H. Wei, and J. Mao, *Plasmon-enhanced luminescence of YAG: Yb, Er nanopowders by Ag nanoparticles embedded in silicate glass.* Materials Letters, 2011. **65**(2): p. 282-284.

58. Hilger, A., M. Tenfelde, and U. Kreibig, *Silver nanoparticles deposited on dielectric surfaces.* Applied Physics B: Lasers and Optics, 2001. **73**(4): p. 361-372.

59. Xu, G., M. Tazawa, P. Jin, and S. Nakao, *Surface plasmon resonance of sputtered Ag films: substrate and mass thickness dependence.* Applied Physics A: Materials Science & Processing, 2005. **80**(7): p. 1535-1540.

60. Manikandan, D., S. Mohan, P. Magudapathy, and K.G.M. Nair, *Blue shift of plasmon resonance in Cu and Ag ion-exchanged and annealed soda-lime glass: an optical absorption study.* Physica B: Condensed Matter, 2003. **325**(0): p. 86-91.

61. Thomas, S., S.K. Nair, E.M.A. Jamal, S.H. Al-Harthi, M.R. Varma, and M.R. Anantharaman, *Size-dependent surface plasmon resonance in silver silica nanocomposites.* Nanotechnology, 2008. **19**(7): p. 075710.

62. Link, S. and M.A. El-Sayed, *Size and Temperature Dependence of the Plasmon Absorption of Colloidal Gold Nanoparticles.* The Journal of Physical Chemistry B, 1999. **103**(21): p. 4212-4217.

63. Johnson, P.B. and R.W. Christy, *Optical Constants of the Noble Metals.* Physical Review B, 1972. **6**(12): p. 4370-4379.

64. Hahn, D.W., *Light scattering theory.* Department of Mechanical and Aerospace Engineering, Florida, 2006.

65. Baffou, G. and R. Quidant, *Thermo-plasmonics: using metallic nanostructures as nano-sources of heat.* Laser & Photonics Reviews, 2013. **7**(2): p. 171-187.

66. Marton, J. and J. Lemon, *Optical Properties of Aggregated Metal Systems. I. Theory.* Physical Review B, 1971. **4**(2): p. 271-280.

67. Shalaev, V.M., *Optical Properties of Nanostructured Random Media*. 2001: Springer.

68. Sancho-Parramon, J., S. Bosch, A. Abdolvand, A. Podlipensky, G. Seifert, and H. Graener, *Effective medium models for metal-dielectric composites: an analysis based on the spectral density theory*, in *Symposium*. 2006: Jena.

69. Bergman, D.J., *The dielectric constant of a composite material—A problem in classical physics.* Physics Reports, 1978. **43**(9): p. 377-407.

70. Ma, Y., J. Lin, S. Qin, N. Zhou, Q. Bian, H. Wei, and Z. Feng, *Preparation of Ag nanocrystals embedded silicate glass by field-assisted diffusion and its properties of optical absorption.* Solid State Sciences, 2010. **12**(8): p. 1413-1418.

71. Sancho-Parramon, J., V. Janicki, P. Dubček, M. Karlušić, D. Gracin, M. Jakšić, S. Bernstorff, D. Meljanac, and K. Juraić, *Optical and structural properties of silver nanoparticles in glass matrix formed by thermal annealing of field assisted film dissolution.* Optical Materials, 2010. **32**(4): p. 510-514.

72. Najafi, S.I., *Introduction to glass integrated optics*. 1992, Boston, London: Artech House.

73. Tervonen, A., B.R. West, and S. Honkanen, *Ion-exchanged glass waveguide technology: a review.* Optical Engineering, 2011. **50**(7): p. 071107.

74. Baranovskii, S. and H. Cordes, *On the conduction mechanism in ionic glasses.* The Journal of chemical physics, 1999. **111**(16): p. 7546-7557.

75. Ramaswamy, R.V. and R. Srivastava, *Ion-Exchanged Glass Waveguides: A Review.* Journal of lightwave technology, 1988. **6**(6): p. 984-1002.

76. Zhang, A., T. Suetsugu, and K. Kadono, *Incorporation of silver into soda-lime silicate glass by a classical staining process.* Journal of Non-Crystalline Solids, 2007. **353**(1): p. 44-50.

77. *Schott B270 Sheet Glass, Knight Optical Datasheet*. Available from: http://www.knightoptical.com/_public/documents/1372681801_sheetglassb270tsgb270.pdf.

78. Honkanen, S. and A. Tervonen, *Experimental analysis of Ag+ -Na+ exchange in glass with Ag film ion sources for planar optical waveguide fabrication.* Journal of Applied Physics, 1988. **63**(3): p. 634-639.

79. Doremus, R.H., *Exchange and Diffusion of Ions in Glass.* The Journal of Physical Chemistry, 1964. **68**(8): p. 2212-2218.

80. Belkhir, A., *Detailed study of silver metallic film diffusion in a soda-lime glass substrate for optical waveguide fabrication.* Applied Optics, 2002. **41**(15): p. 2888-2893.

81. Berg, K.-J., A. Berger, and H. Hofmeister, *Small silver particles in glass surface layers produced by sodium-silver ion exchange-their concentration and size depth profile.* Z. Phys. D - Atoms, Molecules and Clusters, 1991. **20**: p. 309-311.

82. Najafi, S., P. Suchoski, and R. Ramaswamy, *Silver film-diffused glass waveguides: diffusion process and optical properties.* Quantum Electronics, IEEE Journal of, 1986. **22**(12): p. 2213-2218.

83. Findakly, T. and E. Garmire, *Reduction and control of optical waveguide losses in glass.* Applied Physics Letters, 1980. **37**(10): p. 855.

84. Fantone, S.D., *Refractive index and spectral models for gradient-index materials.* Applied Optics, 1983. **22**(3): p. 432-440.

85. Albert, J. and G. Yip, *Stress-induced index change for K+-Na+ ion exchange in glass.* Electronics Letters, 1987. **23**(14): p. 737-738.

86. Hale, D., *Strengthening of silicate glasses by ion exchange.* Nature, 1968. **217**: p. 1115-1118.

87. Chartier, G., P. Jaussaud, A. De Oliveira, and O. Parriaux, *Optical waveguides fabricated by electric-field controlled ion exchange in glass.* Electronics Letters, 1978. **14**(5): p. 132-134.

88. Quaranta, A., E. Cattaruzza, and F. Gonella, *Modelling the ion exchange process in glass: Phenomenological approaches and perspectives.* Materials Science and Engineering: B, 2008. **149**(2): p. 133-139.

89. Dubiel, M., S. Brunsch, U. Kolb, D. Gutwerk, and H. Bertagnolli, *Experimental studies investigating the structure of soda-lime glasses after silver-sodium ion exchange.* Journal of Non-Crystalline Solids, 1997. **220**(1): p. 30-44.

90. Krieger, U.K. and W.A. Lanford, *Field Assisted Transport of Na+-, Ca2+- Ions and Electrons in commercial Soda Lime Glasses.* J. Non-Crystalline Solids, 1988. **102**: p. 50-61.

91. Mariappan, C.R. and B. Roling, *Mechanism and kinetics of Na+ ion depletion under the anode during electro-thermal poling of a bioactive glass.* Journal of Non-Crystalline Solids, 2010. **356**(11-17): p. 720-724.

92. Carlson, D.E., *Ion Depletion of Glass at a Blocking Anode: I, Theory and Experimental Results for Alkali Silicate Glasses.* Journal of the American Ceramic Society, 1974. **57**(7): p. 291-294.

93. Myers, R.A., N. Mukherjee, and S.R.J. Brueck, *Large second-order nonlinearity in poled fused silica.* Optics Letters, 1991. **16**(22): p. 1732-1734.

94. Kazansky, P.G. and P.S.J. Russel, *Thermally poled glass: frozen-in electric field or oriented dipoles?* Optics Communications, 1994. **110**(5–6): p. 611-614.

95. Beresna, M., P.G. Kazansky, O. Deparis, I.C.S. Carvalho, S. Takahashi, and A.V. Zayats, *Poling-Assisted Fabrication of Plasmonic Nanocomposite Devices in Glass.* Advanced Materials, 2010. **22**(39): p. 4368-4372.

96. Podlipensky, A., A. Abdolvand, G. Seifert, H. Graener, O. Deparis, and P.G. Kazansky, *Dissolution of silver nanoparticles in glass through an intense dc electric field.* Journal of Physical Chemistry B, 2004. **108**(46): p. 17699-17702.

97. Kapila, D. and J.L. Plawsky, *Diffusion processes for integrated waveguide fabrication in glasses: A solid-state electrochemical approach.* Chemical Engineering Science, 1995. **50**(16): p. 2589-2600.

98. Wackerow, S., G. Seifert, and A. Abdolvand, *Homogenous silver-doped nanocomposite glass.* Opt. Mater. Express, 2011. **1**(7): p. 1224-1231.

99. Wackerow, S. and A. Abdolvand, *Optical analyses of the formation of a silver nanoparticle-containing layer in glass.* Optics Express, 2012. **20**(21): p. 23227-23234.

100. Pan, A., Z. Yang, H. Zheng, F. Liu, Y. Zhu, X. Su, and Z. Ding, *Changeable position of SPR peak of Ag nanoparticles embedded in mesoporous SiO2 glass by annealing treatment.* Applied Surface Science, 2003. **205**(1–4): p. 323-328.

101. Yata, K. and T. Yamaguchi, *Ostwald ripening of silver in glass.* Journal of Materials Science, 1992. **27**(1): p. 101-106.

102. Dubiel, M., J. Haug, H. Kruth, H. Hofmeister, and K.-D. Schicke, *Ag/Na ion exchange in soda-lime glasses and the formation of small Ag nanoparticles.* Materials Science and Engineering: B, 2008. **149**(2): p. 146-151.

103. Araujo, R., *Colorless glasses containing ion-exchanged silver.* Applied Optics, 1992. **31**(25): p. 5221-5224.

104. Borsella, E., E. Cattaruzza, G.D. Marchi, F. Gonella, G. Mattei, P. Mazzoldi, A. Quaranta, G. Battaglin, and R. Polloni, *Synthesis of silver clusters in silica-based glasses for optoelectronics applications.* Journal of Non-Crystalline Solids, 1999. **245**: p. 122-128.

105. Varma, R.S., D.C. Kothari, and R. Tewari, *Nano-composite soda lime silicate glass prepared using silver ion exchange.* Journal of Non-Crystalline Solids, 2009. **355**(22-23): p. 1246-1251.

106. Podlipensky, A.V., *Laser assisted modification of optical and structural properties of composite glass with silver nanoparticles*. 2005, Martin-Luther Universität Halle-Wittenberg.

107. Borsella, E., G. Battaglin, M. Garcia, F. Gonella, P. Mazzoldi, R. Polloni, and A. Quaranta, *Structural incorporation of silver in soda-lime glass by the ion-exchange process: a photoluminescence spectroscopy study.* Applied Physics A: Materials Science & Processing, 2000. **71**(2): p. 125-132.

108. Wackerow, S. and A. Abdolvand, *Laser-assisted one-step fabrication of homogeneous glass–silver composite.* Applied Physics A, 2012. **109**(1): p. 45-49.

109. Wackerow, S. and A. Abdolvand, *Generation of silver nanoparticles with controlled size and spatial distribution by pulsed laser irradiation of silver ion-doped glass.* Optics Express, 2014. **22**(5): p. 5076-5085.

110. Wackerow, S. and A. Abdolvand, *An ion exchange substrate and metalized product and apparatus and method for production thereof*. 2013.

111. Krüger, J. and W. Kautek, *Ultrashort pulse laser interaction with dielectrics and polymers*, in *Polymers and Light*. 2004, Springer. p. 247-290.

112. Liu, J., *Simple technique for measurements of pulsed Gaussian-beam spot sizes.* Optics Letters, 1982. **7**(5): p. 196-198.

113. Tang, G. and A. Abdolvand, *Structuring of titanium using a nanosecond-pulsed Nd: YVO4 laser at 1064 nm.* The International Journal of Advanced Manufacturing Technology, 2013: p. 1-7.

114. Peng, P., A. Hu, and Y. Zhou, *Laser sintering of silver nanoparticle thin films: microstructure and optical properties.* Applied Physics A, 2012. **108**(3): p. 685-691.

115. Schneider, C.A., W.S. Rasband, and K.W. Eliceiri, *NIH Image to ImageJ: 25 years of image analysis.* Nat Meth, 2012. **9**(7): p. 671-675.

116. Schick, H.L., *A Thermodynamic Analysis of the High-temperature Vaporization Properties of Silica.* Chemical Reviews, 1960. **60**(4): p. 331-362.

117. Gödeke, D., M. Müller, and C. Rüssel, *High-temperature UV-VIS-NIR absorption and emission spectroscopy of soda-lime-silica glasses doped with Nd2O3.* Glass Science and Technology, 2003. **76**(1): p. 28-32.

118. Saito, K. and A.J. Ikushima, *Absorption edge in silica glass.* Physical Review B, 2000. **62**(13): p. 8584-8587.

119. Jensen, L., M. Mende, S. Schrameyer, M. Jupé, and D. Ristau, *Role of two-photon absorption in Ta2O5 thin films in nanosecond laser-induced damage.* Opt. Lett., 2012. **37**(20): p. 4329-4331.

120. Helebrant, A., C. Buerhop, and R. Weissmann, *Mathematical modelling of temperature distribution during CO 2 laser irradiation of glass.* Glass Technology, 1993. **34**(4): p. 154-158.

121. Stepanov, A.L., D.E. Hole, and P.D. Townsend, *Modification of size distribution of ion implanted silver nanoparticles in sodium silicate glass using laser and thermal annealing.* Nuclear Instruments and Methods in Physics Research Section B: Beam Interactions with Materials and Atoms, 1999. **149**(1–2): p. 89-98.

122. Lim, H. and J. Yoo, *FEM based simulation of the pulsed laser ablation process in nanosecond fields.* Journal of Mechanical Science and Technology, 2011. **25**(7): p. 1811-1816.

123. Özıñsık, M.N., *Heat Conduction*. Vol. 2. 1993: Wiley (New York).

124. Ursell, T.S., *The Diffusion Equation - A Multi-dimensional Tutorial*, http://www.rpgroup.caltech.edu/~natsirt/aph162/diffusion_old.pdf, Editor. 2007.

125. Shimizu, M., M. Sakakura, M. Ohnishi, Y. Shimotsuma, T. Nakaya, K. Miura, and K. Hirao, *Mechanism of heat-modification inside a glass after irradiation with high-repetition rate femtosecond laser pulses.* Journal of Applied Physics, 2010. **108**(7): p. 073533.

126. Sanders, D.J., *Temperature distributions produced by scanning Gaussian laser beams.* Appl. Opt., 1984. **23**(1): p. 30-35.

127. Climent-Font, A., *Commentary: Luster ceramics: a 9th century AD nanotechnology.* Journal of Nanophotonics, 2012. **6**(1): p. 060303-060303.

128. Sciau, P., *Nanoparticles in ancient materials: the metallic lustre decoration of medieval ceramics*, Chapter.

129. Lorenz, P., F. Frost, M. Ehrhardt, and K. Zimmer, *Laser-induced fabrication of randomly distributed nanostructures in fused silica surfaces.* Applied Physics A, 2013. **111**(4): p. 1025-1030.

130. Ruffino, F., A. Pugliara, E. Carria, L. Romano, C. Bongiorno, G. Fisicaro, A. La Magna, C. Spinella, and M.G. Grimaldi, *Towards a laser fluence dependent nanostructuring of thin Au films on Si by nanosecond laser irradiation.* Applied Surface Science, 2012. **258**(23): p. 9128-9137.

131. Grochowska, K., G. Śliwiński, A. Iwulska, M. Sawczak, N. Nedyalkov, P. Atanasov, G. Obara, and M. Obara, *Engineering Au Nanoparticle Arrays on SiO2 Glass by Pulsed UV Laser Irradiation.* Plasmonics, 2013. **8**(1): p. 105-113.

132. Zhang, J., W. Dong, J. Sheng, J. Zheng, J. Li, L. Qiao, and L. Jiang, *Silver nanoclusters formation in ion-exchanged glasses by thermal annealing, UV-laser and X-ray irradiation.* Journal of Crystal Growth, 2008. **310**(1): p. 234-239.

133. Sheng, J., J. Zheng, J. Zhang, C. Zhou, and L. Jiang, *UV-laser-induced nanoclusters in silver ion-exchanged soda-lime silicate glass.* Physica B: Condensed Matter, 2007. **387**(1): p. 32-35.

134. Zhang, J., W. Dong, L. Qiao, J. Li, J. Zheng, and J. Sheng, *Silver nanocluster formation in soda-lime silicate glass by X-ray irradiation and annealing.* Journal of Crystal Growth, 2007. **305**(1): p. 278-284.

135. Qiu, J., M. Shirai, T. Nakaya, J. Si, X. Jiang, C. Zhu, and K. Hirao, *Space-selective precipitation of metal nanoparticles inside glasses.* Applied Physics Letters, 2002. **81**(16): p. 3040.

136. Rashidi-Huyeh, M. and B. Palpant, *Thermal response of nanocomposite materials under pulsed laser excitation.* Journal of Applied Physics, 2004. **96**(8): p. 4475.

137. Nogi, K., K. Ogino, A. McLean, and W.A. Miller, *The temperature coefficient of the surface tension of pure liquid metals.* Metallurgical Transactions B, 1986. **17**(1): p. 163-170.